GRADUATE COLLEGE

TRANSPORT OF NANOPARTICLES IN POROUS MEDIA BY NUMERICAL SIMULATIONS

A DISSERTATION

SUBMITTED TO THE GRADUATE FACULTY

in partial fulfillment of the requirements for the

Degree of

DOCTOR OF PHILOSOPHY

By

THI KIM VI NGUYEN
Norman, Oklahoma
2023

Downloaded from SHAREOK. Persistent Handle URL: https://hdl.handle.net/11244/337629

TRANSPORT OF NANOPARTICLES IN POROUS MEDIA

BY NUMERICAL SIMULATIONS

A DISSERTATION APPROVED FOR THE

SCHOOL OF CHEMICAL, BIOLOGICAL AND MATERIALS ENGINEERING

BY THE COMMITTEE CONSISTING OF

Dr. Dimitrios V. Papavassiliou, Chair

Dr. Prakash Vedula

Dr. Liangliang Huang

Dr. Sepideh Razavi

Dr. Vassilios I. Sikavitsas

© Copyright by THI KIM VI NGUYEN 2023

All Rights Reserved.

To my beloved family - my parents, husband, and children - who have stood by me through every step of this journey, I dedicate this dissertation with heartfelt gratitude and appreciation.

Acknowledgments

I would like to express my sincere appreciation to Dr. Dimitrios V. Papavassiliou, my advisor, for his invaluable support and exceptional mentorship, without which this work would not have been possible. Additionally, I am grateful to the members of the committee, Dr. Prakash Vedula, Dr. Liangliang Huang, Dr. Sepideh Razavi, and Dr. Vassilios I. Sikavitsas, for their insightful advice and recommendations. The financial assistance provided by The American Chemical Society Petroleum Research Fund through grant PRF # 58518-ND9 is also greatly appreciated, as is funding from the Office of the Vice President for Research and Partnerships at the University of Oklahoma through the Big Idea Challenge project on Carbon-Free Hydrogen Productions and Storage. Furthermore, I extend my gratitude to the OU Supercomputing Center for Education & Research (OSCER) and the Texas Advanced Computing Center, which supported this work through XSEDE allocation CTS-090025. Finally, I am thankful to my colleagues and friends for their valuable discussions and the enjoyable time we spent together.

TABLE OF CONTENTS

LIST OF TABLES ..... **viii**
LIST OF FIGURES ..... **ix**
ABSTRACT ..... **xiii**
I. INTRODUCTION **1**
I.1. Velocity magnitude distribution for flow in porous media 1
I.2. Hydrodynamic dispersivity based on Lagrangian Peclet number 4
I.3. Aggregation of nanoparticles 8
II. NUMERICAL METHODOLOGY **14**
II.1. Velocity magnitude distribution for flow in porous media 14
II.1.1. Simulation setup 14
II.1.1.a. Velocity magnitude distribution for flow in sphere packings and scaffolds 14
II.1.1.b. Relationship between pore fluid velocity distribution and pore size distribution 19
II.1.2. Lattice Boltzmann method 22
II.1.2.a. Algorithm 22
II.1.2.b. Code validation and verification 24
II.1.3. Probability density function for velocity magnitude 27
II.1.4. Pore-size calculation - Watershed segmentation 27
II.1.5. Pore-size calculation– Maximal ball (MB) algorithm 29
II.2. Hydrodynamic dispersivity based on Lagrangian Peclet number 30
II.2.1. Simulation setup 30
II.2.2. Lagrangian Particle Tracking 31
II.2.3. Lagrangian time scale and Velocity Autocorrelation Function 33
II.2.4. Hydrodynamic dispersion coefficient 34
II.3. Aggregation of nanoparticles 34
II.3.1. Simulation set up 34
II.3.1.a. Aggregation of nanoparticles in bulk 34
II.3.1.b. Aggregation of nanoparticles in porous media 35
II.3.2. Lagrangian particle tracking based on force balance approach (LPT/FB) 37
II.3.3. Fractal dimension 42
II.3.4. Hydrodynamic radius and asphericity of an aggregate 44

III. RESULTS 46
III.1. Velocity Magnitude Distribution for Flow in Porous Media 46
III.1.1. Velocity magnitude distribution for flow in sphere packings and scaffolds 46
III.1.2. Relationship between pore fluid velocity distribution and pore size distribution .. 56
III.2. Hydrodynamic dispersivity based on Lagrangian Peclet number 61
III.2.1. Lagrangian time scale and Velocity Autocorrelation Function 61
III.2.2. Hydrodynamic dispersivity 65
III.3. Aggregation of nanoparticles 70
III.3.1. Validation results against aggregation of NPs in bulk 70
III.3.2. Aggregation in porous media 72
III.3.2.a. Effects of the ionic strength 72
III.3.2.b. Effects of the pore velocity on diffusion-limited aggregation 77
III.3.2.c. Effects of the pore velocity on reaction-limited aggregation 80
III.3.2.d. Effects of the particle size on diffusion-limited aggregation 81
III.3.2.e. Effects of the particle size on the reaction-limited aggregation 83
III.3.2.f. Formation and behavior of large clusters 85
III.3.2.g. Positions of clusters relative to the walls and their velocities 87
IV. CONCLUSIONS AND FUTURE PLANS 92
IV.1. Conclusions 92
IV.2. Future Plans 95
REFERENCE 97
APPENDIX 115
Appendix A: Hydrodynamic dispersivity based on Lagrangian Peclet number 115
Appendix B: Aggregation of nanoparticles 123

LIST OF TABLES

Table I.1. Summary of studies on hydrodynamic dispersion through packed beds in the randomly packed spheres (RPS) configuration..... 7

Table II.1. Summary of the geometry characteristics of the porous media investigated in this study..... 17

Table II.2. Details of domains of all porous media examined in this work and results for two-sample KS tests for the pore volume and velocity magnitude distributions. The pore volumes and local velocity magnitudes in a porous type will be distributed by the same distribution if the two-sample KS test statistic is lower than 0.152, which is the critical value at the significance level of 0.2..... 20

Table II.3. Comparison of the results for dimensionless permeability with prior results. The reported error is the relative absolute error compared to references. 25

Table II.4. The lattice Boltzmann method (LBM) code verification by Blake–Kozeny equation. The reported error is the relative absolute error for the calculated superficial velocity. 26

Table II.5. Details of simulations performed by the multiscale model for aggregation and movement of CeO_2 nanoparticles in randomly packed spheres with the presence of ionic strength. 36

Table III.1. The p-values from the Kolmogorov-Smirnov goodness-of-fit tests conducted for velocity distributions in different types of sphere packings and scaffolds including data from ref.[1] against the six best distribution forms are listed. The table also displays the shape and scale factors represented by α and β for the Weibull distribution that best fits each porous medium. The p-values of the Kolmogorov-Smirnov test conducted for the null hypothesis testing whether the Weibull universal form ($\alpha = 1.212$, $\beta = 1.062$) was a good fit are illustrated in the last column. The attained significance level was 0.2 in all cases except for those with p-value marked with a, b, or c where that level was 0.1, 0.01, or 0.00, respectively..... 51

Table III.2. Three correlation schemes for hydrodynamic dispersion of particle transport in an FCC-packed bed..... 68

Table III.3. Three correlation schemes for hydrodynamic dispersion of particles transport in RPS-packed bed..... 68

LIST OF FIGURES

Figure II.1. Geometries of ideally packed spheres including (a) SC - 1 sphere, (b) BCC - 2 spheres, (c) FCC - 4 spheres, (d) SC - 125 spheres, (e) BCC - 250 spheres, and (f) FCC - 256 spheres... 16

Figure II.2. Geometries of randomly packed spheres containing (a) monodisperse spheres, (b) bidisperse spheres, and (c) tridisperse spheres. 16

Figure II.3. Geometries of (a) fiber scaffold, (b) monodisperse foam scaffold, and (c) bidisperse foam scaffold. 18

Figure II.4. Pore velocity calculated by averaging over an increasing part of the domain volume. The average pore velocity changed with the domain size when water at room temperature flows through the monodisperse sphere packing, consisting of 432 spheres, in x direction. 19

Figure II.5. Geometries of (a) a sandstone - S1, (b) synthetic silica - A1, and (c) carbonate - C1. The red color represents the solid phase, while the blue one indicates the pore space of porous media. 20

Figure II.6. (a) Details of the velocity magnitude distributions of the flow through packed bed containing monodisperse spheres (sphere diameter = 0.2 cm, porosity = 37%, average pore velocity magnitude U= 1.27 x 10^{-2} cm/s) in random configuration that was measured by experiment (Souzy et al.[1]) and the present LBM simulation (green data points), (b) streamwise velocity, and (c) spanwise velocity. It is seen that the LBM computation results agree with the experiments not only in the mean, but also in the whole range of the velocity distribution and in both the streamwise and spanwise directions. 27

Figure II.7. Examples of 2D pore extraction by using the watershed method for (a) FCC, (b) packing of monodisperse spheres, and (c) monodisperse foam scaffold. The black color indicates the solid matrix and the white color indicates the void pore space. The thin black straight lines appearing in the panels to the right indicate pore boundaries found using the watershed algorithm. 29

Figure II.8. Calculations are performed for every simulation step in LPT/FB aggregation model. h is the distance between two particles; dx is the mesh resolution in the x direction; and Δs is the distance that a particle travel at the current step. 41

Figure II.9. Fractal dimension of aggregates is defined from the relationship between R_g/R and n as seen in Eqn. II.24. The slope of the line is the fractal dimension, which is equal to 1.7, in this case of aggregation of CeO_2 particles of D = 190nm in a solution of 0.2M KCl and at bulk conditions. 43

Figure II.10. (a) Particles are distributed in a spherical cluster with Df= 3 and As= 0, (b) Particles are arranged in an orderly 3D structure with Df= 1.2 and As = 0, (c) a 2D cluster has a hexagonal

shape with Df= 2 and As = 0.25, (d) a 2D cluster that is inscribed in the same circle as the hexagonal cluster in 3(c); and it has Df= 1.1 and As = 0.25..... 45

Figure III.1. (a) The distributions of normalized pore velocity magnitude for water flow in monodisperse sphere packing at different pore velocities in the x direction, and (b) the velocity distribution of different fluids with pore velocity in x direction of 0.1 cm/s..... 46

Figure III.2. Details of normalized pore velocity magnitudes in 2D planes perpendicular to the streamwise axis and parallel to the flow direction in (a) SC, (b) FCC, (c) the monodisperse sphere packing, (d) the monodisperse foam scaffold, (e) the bidisperse foam scaffold, and (f) the fiber scaffold. The areas seen in yellow color designate the solid phase, where the velocity magnitude is zero. 48

Figure III.3. Graphs of the distributions of the 3D normalized velocity magnitude together with the distribution tested with the null hypothesis – the Weibull distribution for (a) random sphere packings, (b) scaffolds, (c) SC, BCC, and (d) FCC. 49

Figure III.4. Distributions of normalized velocity magnitude and normalized pore area in all types of porous materials including (a) SC, (b), BCC, (c) FCC, (d) monodisperse sphere packing, (e) bidisperse sphere packing, (f) tridisperse sphere packing, (g) monodisperse foam scaffold, (h) bidisperse foam scaffold, (i) fiber scaffold with flow in x direction and (j) fiber scaffold with the flow in the y direction. 55

Figure III.5. The probability density function (PDF) and the cumulative distribution function (CDF) for normalized velocity magnitude and normalized pore volume in various porous media: (a) Berea sandstone, (b) carbonate C1, (c) synthetic silica A1, (d) tridisperse sphere packing, (e) fiber-x. 60

Figure III.6. The velocity correlation coefficient for the packed bed with an FCC geometry with time for (**a**) Schmidt number (Sc) = 100, (**b**) Sc = 1000, (**c**) Sc = 7080, and (**d**) Sc = 10,000. Each graph contains a velocity autocorrelation coefficient for different average pore velocities. 63

Figure III.7. The velocity correlation coefficients for the packed bed with an RPS geometry with time for (**a**) Sc = 100, (**b**) Sc = 1000, (**c**) Sc = 7080, and (**d**) Sc = 10,000. Each graph contains velocity autocorrelation coefficients for different average pore velocities. 64

Figure III.8. The effect of the Schmidt number on the velocity correlation coefficient, as well as Lagrangian timescales for both cases including the FCC (a) and RPS (b) configurations at the same average pore velocity of 1000 μm/s. 65

Figure III.9. The ratio of the hydrodynamic dispersion coefficient over the effective molecular diffusion coefficient in an FCC as a function of (a) the effective Eulerian Peclet number based on sphere diameter and (**b**) the effective Peclet number determined from the Lagrangian length scale.[65] 66

Figure III.10. The ratio of the hydrodynamic dispersion coefficient over the effective molecular diffusion coefficient in an RPS as a function of (a) the effective Eulerian Peclet number based on sphere diameter and (**b**) the effective Peclet number determined from the Lagrangian length scale.[65] 67

Figure III.11. Interaction forces (a) and the net interaction energy (b) between two particles in aqueous suspension under different KCl concentrations. 71

Figure III.12. The hydrodynamic radius of aggregates measured by experiments[148] and simulations during the aggregation process of CeO_2 nanoparticles in different KCl concentrations. 71

Figure III.13. Fractal dimensions of aggregates in reaction-limited aggregation (0.02M KCl) and diffusion-limited aggregation (0.1M KCl, 0.15M KCl, and 0.2M KCl) were calculated by the simulation. 72

Figure III.14. Effects of potassium chloride concentration on (a) the aggregation kinetics, (b) the ratio between the number of single particles over the total number of clusters, (c) the fractal dimension, (d) the asphericity, and (e) the probability density function of cluster size at t = 500 PV. The investigated electrolyte concentrations included 0.001M, 0.02M, and 0.2M KCl. 74

Figure III.15. Illustration of computed clusters in (a) diffusion-controlled aggregation with Df = 1.55, As = 0.53, and (b) reaction-controlled aggregation with Df= 1.9, As = 0.3. The solid phase of the porous medium is not shown. Red dots represent agglomerates, while blue dots are monomer particles that did not yet agglomerate. 76

Figure III.16. Effects of the pore velocity on (a) the aggregation kinetics, (b) the ratio between the number of single particles over the total number of clusters, (c) the fractal dimension, (d) the asphericity, and (e) the probability density function of cluster size at t = 500 PV in the diffusion-limited regime. Particles, suspended in 0.2M KCl solution, traveled through randomly packed spheres with the pore velocity varying from 50 μm/s to 2000 μm/s. 79

Figure III.17. The attachment of a single particle in blue color to a large cluster in red color (a) reduces the fractal dimension and asphericity because the boundary is expanded from the red ellipse to the blue ellipse, (b) lowers the fractal dimension and improves the asphericity since the blue boundary differs from a sphere, (c) enhances the fractal dimension without changing the asphericity. 79

Figure III.18. Effects of the pore velocity on (a) the aggregation kinetics, (b) the ratio between the number of single particles over the total number of clusters, (c) the fractal dimension, (d) the asphericity, and (e) the probability density function of cluster size at t = 500 PV in the reaction-limited regime. Particles, suspended in 0.02M KCl solution, traveled through randomly packed spheres with the pore velocity varying from 50 μm/s to 2000 μm/s. 81

Figure III.19. Effects of the particle size on (a) the aggregation kinetics, (b) the ratio between the number of single particles over the total number of clusters, (c) the fractal dimension, (d) the asphericity, and (e) the probability density function of cluster size at t = 500 PV in diffusion-limited regime. Particles, suspended in 0.2M KCl solution, traveled through randomly packed spheres at the pore velocity 500 μm/s. 83

Figure III.20. Effects of the particle size on (a) the aggregation kinetics, (b) the ratio between the number of single particles over the total number of clusters, (c) the fractal dimension, (d) the asphericity, and (e) the probability density function of cluster size at t = 500 PV in the reaction-limited regime. Particles, suspended in 0.02M KCl solution, traveled through randomly packed spheres at the pore velocity of 500 μm/s. 84

Figure III.21. Images of (a), (b) two enormous ceria clusters obtained by our simulations (particles involved in the aggregation are shown in red; and the solid matrix of the porous medium is displayed in yellow), (c) a large silica cluster obtained by the lab microscope (reprinted from a publication[186] with permission from Elsevier), (d) a large titania aggregate obtained by the lab microscope (reprinted from a publication[67] with permission from American Chemical Society). 86

Figure III.22. Simulation results of CeO_2 particles in 0.2M KCl solution through a sphere packing, at 100 μm/s, from 0 PV to 1000 PV include (a) aggregation kinetics, (b) the ratio between the number of single particles and the total number of clusters, (c) the fractal dimension, (d) the asphericity, and (e) the cluster size probability density function at different times such as 100 PV, 200 PV, 400 PV, 800 PV and 1000 PV. 87

Figure III.23. (a) Distances from clusters to the nearest walls and (b) the velocities of clusters at different times such as 0 PV, 400 PV, 800 PV, and 1000 PV. The distance from a cluster to the wall is the minimum distance from the surface of any particle that is nearest to the wall. 89

Figure III.24. (a) Minimum distances from 125 single particles, which formed a large cluster at 1200 PV, to the nearest wall and (b) their velocity at different times 0 PV, 400 PV, 800 PV, and 1200 PV. 90

Figure III.25. (a) Minimum distances from 167 single particles, which formed a large cluster at 1200 PV, to the nearest wall and (b) their velocity at different times 0 PV, 400 PV, 800 PV, and 1200 PV. 91

ABSTRACT

This thesis focuses on three primary topics related to the movement of fluid and nanoparticles (NPs) in porous media. While prediction of local fluid velocities within porous media are significant, conducting experiments to measure them can be exceedingly difficult. Therefore, this work aimed to develop methods to predict velocity distributions in porous media. The lattice Boltzmann method was applied to solve for the fluid velocity fields through different media, such as sphere packings, scaffolds, sandstones, carbonates, and synthetic silica. The one-sample Kolmogorov-Smirnov (KS) goodness-of-fit statistical tests were utilized to examine whether the velocity distributions in different porous media followed any known distribution types, whereas the two-sample KS goodness-of-fit tests were used to determine if the velocity and pore-size distributions are statistically similar. Simulation results indicated that the velocity magnitude and pore volume in a porous medium follow the same distribution for all the examined porous media with continuous pore size distributions. In addition, velocity magnitude distributions in scaffolds and sphere packings with random configurations could be predicted by a single Weibull distribution model within statistical accuracy.

The hydrodynamic dispersivity of nanoparticles (NPs) is a significant parameter in determining their mobility, and our study sought to investigate this parameter using the Lagrangian approach, as opposed to the Eulerian approach that has been commonly employed in previous studies. The lattice Boltzmann method (LBM) was employed to simulate flow in porous media, and Lagrangian particle tracking (LPT) was used to track the movement of individual dispersing particles without considering the particle-particle interactions. In other words, the movement of particles was a consequence of both the molecular diffusion of the particles themselves and the convection of the surrounding fluid. It was found that the hydrodynamic dispersion coefficient

linearly depended on the effective Lagrangian Peclet number, based on a length scale that took the molecular diffusion effects as well as the convection effects into account; and this relationship held for different porous media. More importantly, this linear equation was simpler and more precise than the one formed by using the Eulerian Peclet number with a fixed length scale. This result confirmed that Lagrangian length and time scales were appropriate for modeling particle dispersion.

The mobility of NPs in porous media is significantly impacted by their tendency to aggregate since large aggregates may induce some problems such as pore clogging or blocking and reduce the mobility of NPs. Thus, a new model, Lagrangian Particle Tracking based on the force balance approach (LPT/FB), was built to simulate the aggregation process and to predict the morphology of aggregates when particles move in porous media. It relied on Newton's second law of motion and took interaction forces among particles into account. Aggregation kinetics and fractal dimension results from the computational model for Cerium oxide (CeO_2) particles, suspended in potassium chloride (KCl) solutions with different concentrations, were verified against experimental results. The model was then employed to investigate the effects of ionic strength, pore velocity, and particle size on the aggregation of CeO_2 particles together with their fractal dimension and asphericity when they moved in randomly packed spheres. The electrolyte concentration was found to be the most important factor impacting the aggregation process and the aggregate structure. It was followed by the pore velocity, which considerably influenced the aggregation kinetics and fractal dimensions, especially in the diffusion-limited regime. The primary particle size had a minor effect on the aggregation kinetics but created a noticeable change in the fractal dimension of reaction-limited aggregates.

I. INTRODUCTION

The study of fluid flow through porous media has many applications in various industrial and environmental fields such as the spread of contaminants in aquifers, the movement of chemicals in packed bed reactors, the delivery of nutrients or drugs in tissues, the sequestration of carbon dioxide in geological formations, the delivery of nutrient flow through scaffolds in bioreactors, and so on.[1–8] These processes are strongly characterized by not only the average fluid velocity but also the local fluid velocities within the pore space; hence, predicting the distribution of pore fluid velocities is of critical importance.[1,3]

Nanoparticles have been widely used in various fields including the petroleum industry, agriculture, medicine, biotechnology, and electronics.[9] However, the popular use of NPs and their harmful impacts on the environment makes the understanding of their mobility, especially in porous media essential. In the other words, studying the hydrodynamic dispersivity of NPs in porous media is highly advantageous. Furthermore, while NPs move in such complex media, aggregation of NPs due to particle-particle interactions is inevitable and could lead to some issues such as pore clogging, and pore blocking which alters the transport potentials of particles.[10–12] Thus, this work focuses on three main topics related to the transport of fluid and NPs through porous media, including velocity distribution of fluid, hydrodynamic dispersivity of nanoparticles (without aggregation), and aggregation of nanoparticles in porous media.

I.1. Velocity magnitude distribution for flow in porous media

The local velocity of the flow in porous media is critically important in many applications.[13–20] Extremely high or low values of flow velocities in catalyst-packed beds could lead to the creation of hot spots and catalyst deactivation.[15,19,20] Moreover, in flow perfusion bioreactors for tissue engineering cultures, the cells can be detached from the scaffold surface due

to the very high velocities of flow,[13,14,16,17] or they cannot survive in the very low-velocity regions due to low nutrient transfer.[21] However, obtaining the local velocities of the flow field in such complicated porous materials is far more arduous and time-consuming than calculating the average fluid velocity.

While the prediction of the average velocity of the fluid inside the pores can be obtained by dividing the superficial fluid velocity by the medium porosity, ϕ, predicting the details of the fluid velocity field in such complex porous materials is challenging. Recent advances in computations, mainly through direct simulation techniques that do not depend on Darcy models for the flow (e.g., lattice Boltzmann methods), and recent advances in microscopy, such as confocal microscopy that can help with visualization inside the porous medium, have helped to obtain detailed velocity data, advancing our understanding beyond models that are appropriate for average behavior (e.g., based on Blake-Kozeny or Ergun type of equations). A few prior studies have focused on the distribution of fluid velocity in the pore space. Datta et al.[22] used confocal microscopy to estimate the velocity field for flow through a random packing of glass beads. It was found that the velocity magnitude and the velocity components in both spanwise and streamwise directions were exponentially distributed through the pore space that was completely random and complex. Other researchers have shown that there is a relationship between the pore-network and the pore velocity distribution in porous media.[4,5,23–25] Maier[24] applied the lattice Boltzmann method to simulate flow through glass bead packings; and the results were compared to data obtained from Nuclear Magnetic Resonance (NMR) spectroscopy. It was discovered that the high-velocity tail of the longitudinal velocity distribution was strongly affected by the distribution of the large pores – the longer the tail of the pore distribution, the longer the tail of the velocity distribution.

De Anna and coworkers[5] studied the relationship between pore-network and velocity distribution by Stokesian flow through two-dimensional (2D) porous media generated by non-overlapping circular posts. It was argued that the distribution of small openings determined the distribution of small velocities. Both pore throat size distribution and velocity distribution followed a power law; however, the exponent in the velocity distribution model was half of that in the pore throat size distribution model.

Araújo et al.[23] studied the fluid flow through 2D porous media of overlapping disks with porosities between 0.6 and 0.9. The computational fluid dynamics software Fluent was used to solve the Navier-Stokes equation and to obtain the fluid velocity field. It was found that the distribution of velocity magnitude scaled with the square of porosity followed a Gaussian model, except for very small velocities, while the flux distribution fitted the stretched exponential model with an exponent of 0.5. Siena et al.[4] investigated the relationship between the distribution of longitudinal velocity and that of the pore size in isotropic porous media. The probability density function (PDF) of pore size decayed according to an exponential form, while the velocity PDF followed a stretched exponential model at high velocities. More interestingly, parameters in the model for pore size and velocity were found to be related to each other via a power-law form. Aramideh et al.[25] examined the velocity distribution through a packed bed consisting of spheres by applying a direct numerical simulation (DNS) method to solve the Navier-Stokes equations together with mass and momentum conservation equations. The distribution of velocity changed from a nearly Gaussian model to a Gaussian when the medium porosity increased. Moreover, the authors showed the effects of pore geometry on pore velocity by comparing the spatial correlation in velocity fluctuations and the two-point correlation pore space. It was found that they are strongly correlated to each other for both monodisperse sphere packings and Castlegate sandstone.

Given the above observations, one can hypothesize that the pore velocity distribution can be predicted and that it follows a specific type of a statistical probability density function. Prior investigations for the discovery of common statistical distributions that can be used to predict flow-induced stresses in porous media flows suggest that it is reasonable to make this hypothesis.[26] The distribution of flow-induced stresses in the pore space and on the solid-fluid interface has been found to follow common forms, at least for porous media with high porosity (over 50%). The flow-induced wall stress was found to follow a unique three-point gamma distribution model for porous scaffolds.[27] A common three-point log-normal distribution was also found to fit the distribution of stresses in the bulk of the pore space for all types of packing spheres and highly porous scaffolds.[6,28]

Our goal is to find methods to predict the velocity distributions in different porous media. In the first part, the velocity distributions in different types of sphere packings and scaffolds were examined to determine whether they follow a known form of a statistical PDF, and how these distributions may be affected by the pore structure. In the second part, this research continued studying the velocity and pore-size distributions in other porous media such as random sphere packings, fiber scaffolds, sandstones, carbonates, and synthetic silica.

I.2. Hydrodynamic dispersivity based on Lagrangian Peclet number

Predicting the hydrodynamic dispersion through porous media is of great importance in many engineering applications. For instance, in the field of petroleum engineering, chemicals such as surfactants are injected into hydrocarbon reservoirs to enhance oil recovery.[29] The theory of hydrodynamic dispersion can assist engineers to estimate how far the chemicals reach, thereby designing appropriate injection points to cover the targeted zone. In environmental applications,

dispersion in porous media has helped to predict how pollutants spread in the groundwater and contaminate aquifers.[6,30,31]

What is hydrodynamic dispersion? In general, substances or particles that disperse in a porous medium do so because of two effects: molecular diffusion and convective dispersion (or mechanical dispersion). The transport that combines both mechanisms of dispersion is known as hydrodynamic dispersion.[30,32,33] The effectiveness of solute transport is based on the hydrodynamic dispersion coefficient; and many researchers have worked to determine this coefficient for various porous geometries at different flow regions by using both experimental and numerical methods. All studies have agreed that the hydrodynamic dispersion coefficient is the sum of an effective molecular diffusivity coefficient and a mechanical dispersion coefficient. Furthermore, the coefficient for effective molecular diffusion in porous media, D'_m, is always smaller than that for molecular diffusion in a pure solvent D_m.[30–35]

There have been several suggestions for calculating the effective molecular diffusion coefficient in a porous medium. Several researchers have proposed to estimate this parameter based on the diffusive tortuosity (τ_d), which is defined by the squared ratio of the average length of the path (L_d) traveled by a substance as it diffuses through the porous medium over the straight-line length (L_s), $\tau_d = \left(\frac{L_d}{L_s}\right)^2$. [36] The diffusive tortuosity is often defined as the molecular diffusion coefficient of a species in a free fluid relative to that in a porous medium $\tau_d = \frac{D_m}{D'_m}$.[36–40] However, others have argued that the porosity ϕ should be present in the equation of tortuosity as $\tau_d = \phi \frac{D_m}{D'_m}$.[41–43] From another perspective, other researchers have found that there is a link between the diffusion in a porous medium and its electrical conductivity, proposing a correlation such as $\frac{1}{F\phi} = \frac{D_m}{D'_m}$, where F is the formation electrical resistivity factor.[33,44,45] At the end of the day, it appears that

the most accurate method is to experimentally measure the diffusive tortuosity of a porous medium by measuring the diffusion coefficient, both in the bulk fluid and in the porous medium.[46]

Regarding the hydrodynamic dispersion coefficient, several studies for different types of porous media have ended up with different equation forms for different flow regimes. Table I.1 is a summary of the results related to hydrodynamic dispersivity from different studies for NP movement in randomly packed spheres**.** Most researchers tried to characterize the longitudinal dispersion in sphere-packed beds based on the Eulerian Peclet number Pe_m^E, determined by the diameter of the spheres d_p and molecular diffusion D_m in the bulk fluid,[32,33] as follows:

$$Pe_m^E = Ud_p/D_m \tag{I.1}$$

where U is the pore velocity in the flow direction.

Koch and Brady[34] together with Delgado et al.[32] suggested equations for the longitudinal dispersion coefficient as a function of the effective Eulerian Peclet number defined with the use of the effective molecular diffusivity D'_m (the molecular diffusivity of particles in porous media),

$$Pe_m'^E = Ud_p/D'_m. \tag{I.2}$$

Table I.1. Summary of studies on hydrodynamic dispersion through packed beds in the randomly packed spheres (RPS) configuration.

Reference	Conditions	Equations of hydrodynamic dispersion coefficient
Fried-Combranous[47]	$Pe_m^E < 300$	$\frac{D_L}{D_m} = \frac{1}{\tau_d} + 0.5 {Pe_m^E}^{1.2}$
	$Pe_m^E < 10^5$	$\frac{D_L}{D_m} = \frac{1}{\tau_d} + (1.8 \pm 0.4) Pe_m^E$
Hiby[32,48]	$Re < 300$	$\frac{D_L}{D_m} = \frac{1}{\tau_d} + \frac{0.65 Pe_m^E}{1 + 7 {Pe_m^E}^{-0.5}}$
Harleman et al.[48]	$20 < Pe_m^E < 4000$	$\frac{D_L}{D_m} = 0.67 + 0.66 {Pe_m}^{1.2}$
Koch and Brady[34]	Impermeable packed bed $(1-\varepsilon)^2 < Pe_m'^E/2 < 1$	$\frac{D_L}{D_m'} = 1 + \frac{3}{4}\frac{Pe_m'^E}{2}$
	$Pe_m'^E/2 > 1$	$\frac{D_L}{D_m'} = 1 + \frac{3}{4}\frac{Pe_m'^E}{2} + \frac{\pi^2}{6}(1-\varepsilon)\frac{Pe_m'^E}{2}\ln\left(\frac{Pe_m'^E}{2}\right)$
Delgado et al.[32]	Diffusion regime $(Pe_m^E < 0.1)$	$\frac{D_L}{D_m'} = 1$
	Predominant diffusional regime $(0.1 < Pe_m^E < 4)$	$\frac{D_L}{D_m'} = \frac{Pe_m'^E}{0.8/Pe_m'^E + 0.4}$
	Predominant mechanical dispersion $(4 < Pe_m^E$ and $Re < 10)$	$\frac{D_L}{D_m'} = \frac{Pe_m'^E}{\sqrt{18 {Pe_m'^E}^{-1.2} + 2.35 Sc^{-0.38}}}$
	Pure mechanical dispersion $(10 < Re$ and $Pe_m^E < 10^6)$	$\frac{D_L}{D_m'} = \frac{Pe_m'^E}{25 Sc^{1.14}/Pe_m'^E + 0.5}$
	Dispersion out of Darcy domain $(Pe_m^E > 10^6)$	$\frac{D_L}{D_m'} = \frac{Pe_m'^E}{2}$

Using the sphere diameter as an Eulerian length scale has the advantage of being known *a-priori*. However, the nature of dispersion is Lagrangian, so the hypothesis here is that a Lagrangian length scale should be used to combine the molecular diffusion effects and the convection effects in dispersion. In the present study, it is aimed to find a Lagrangian length and time scale to obtain

the Lagrangian Peclet number, calculate the hydrodynamics dispersivity for different NPs in different porous types, and set up model equations for the dispersion coefficient with the effective Peclet number based on either the Eulerian or the Lagrangian length scale.

I.3. Aggregation of nanoparticles

The use of nanoparticles (NPs) has been increasing in various fields, such as the petroleum industry, agriculture, medicine, biotechnology, electronics, and so on.[49–55] For instance, in the field of petroleum engineering, the injection of NPs, which reduces the surface tension of oil-water or changes the wettability of oil-rock interfaces, could enhance oil recovery.[56,57] Therefore, the mobility of NPs injected in a reservoir strongly affects the efficiency of secondary hydrocarbon recovery. However, the release of nanoparticles in the subsurface could be harmful to the environment.[58–60] For example, the discharge of NPs from petroleum recovery projects or agricultural fertilizers can potentially contaminate aquifers.[61] Thus, understanding the mobility of NPs in porous media is critical to either improve desired effects or hinder undesired ones.

Aggregation of NPs in porous media is inevitable and significant because it changes the size, shape as well as properties of NPs as they propagate.[10–12] Clogging of pores may even occur; however, interactions among NPs have often been neglected in computation; and many studies consider particle movement to be caused by advection and diffusion.[62–65] Several experiments have reported on the formation of aggregates from NPs, such as CeO_2,[60] TiO_2,[11,66,67] ZnO,[10,53,68–70] and nanoscale zero-valent irons (NZVI).[71–75] Due to the importance of particle aggregation, many researchers have proposed simulation models for particle agglomeration in porous media.[59,73,76,77] Most of these models are based on stochastic approaches, which can predict the aggregation kinetics but fail to provide a detailed look into the morphology of aggregates.[59,76] Some models assume that the morphology remains constant during the aggregation process,[73,78] despite fluid

velocity or particle size being known to affect the morphology of aggregates. The modeling of aggregation based on probabilities, rather than the physics of particle-particle interactions, is a result of the difficulty in addressing the multiscale problem of combining the movement of nanoparticles with aggregation.[76] The movement of NP is governed by diffusion and convection; and it can be simulated at relatively large timesteps, on the order of 10^{-4} or 10^{-5}s. However, aggregation is controlled by particle-particle interactions, which are applicable when the distance between two particles is as small as a few nanometers; and it requires much smaller simulation timesteps (10^{-8} or 10^{-9}s).[76]

The Smoluchowski model has been used to predict the aggregation kinetics of nanoparticles.[58,73,78–80] This model considers the aggregation between two particles as a second-order rate process; and the change in concentration of an aggregate consisting of *k* primary particles is expressed as follows:[58,73,77,79–82]

$$\frac{dn_k}{dt} = \frac{1}{2}\alpha \sum_{i+j=k} \beta(i,j) n_i n_j - \alpha n_k \sum_{i=1}^{c} \beta(i,k) n_i \qquad \text{(I.3)}$$

where n_i, n_j, and n_k are the concentrations of particles containing i, j, and k single particles, respectively; t is time; $i, j,$ and k are the number of single particles in aggregates; c is the maximum number of particles in a cluster. The physicochemical properties involved in attachment between two particles are represented by the collision efficiency α, while the collision mechanism is reflected by the collision frequency function β. This model assumes that the agglomeration of particles is caused by three mechanisms: perikinetic, orthokinetic, and differential sedimentation. In the perikinetic mechanism, particle-particle collisions are driven by Brownian motion whereas the orthokinetic mechanism is induced by flow in a fluid that creates shear stress. The last mechanism, differential sedimentation, is a result of size differences among particles. In other

words, the small particles can move faster while the large ones tend to settle quicker and collide with the fast-moving particles on their paths. The total collision frequency function is the sum of collision frequency functions arising from all three mechanisms. They are given as below:[81,82]

$$\beta_{BR}(i,j) = \frac{2k_B T}{3\mu}(v_i^{1/3} + v_j^{1/3})(v_i^{-1/3} + v_j^{-1/3}) \tag{I.4}$$

$$\beta_{SH}(i,j) = \frac{G}{\pi}(v_i^{1/3} + v_j^{1/3})^3 \tag{I.5}$$

$$\beta_{DS}(i,j) = \frac{g}{12\mu}\left(\frac{\pi}{6}\right)^{-1/3}(\rho_p - \rho_f)(v_i^{1/3} + v_j^{1/3})^3|v_i^{1/3} - v_j^{1/3}| \tag{I.6}$$

where β_{BR}, β_{SH}, and β_{DS} represent the collision frequencies due to Brownian motion, shear stress, and size differences, respectively; k_B is the Boltzmann constant; T is temperature; v_i or v_j is the volume of particle i or j; μ is the dynamic viscosity of the fluid; G is the average velocity gradient; g is the gravitational constant; ρ_p and ρ_f are the densities of the particles and the fluid, respectively. This model applies the coalesced sphere assumption, which considers aggregates as compact spheres; however, in reality, aggregates have fractal-like shapes.[83] Thus, this model ignores the effects of the aggregate morphology on the kinetic model.

Lee et al. modified the Smoluchowski model by adding the fractal dimension of aggregates into the kinetic model.[81] The fractal dimension, D_f, is an index characterizing the density of an aggregate structure; and it varies from 1 to 3. The higher the fractal dimension, the denser the structure. The collision frequency functions caused by Brownian motion and fluid shear stress are expressed as:[81]

$$\beta_{BR}(i,j) = \frac{2k_B T}{3\mu}(v_i^{1/D_f} + v_j^{1/D_f})(v_i^{-1/D_f} + v_j^{-1/D_f}) \tag{I.7}$$

$$\beta_{SH}(i,j) = \frac{G}{\pi} v_o^{1-3/D_f} (v_i^{1/D_f} + v_j^{1/D_f})^3. \quad \text{(I.8)}$$

The collision frequency function caused by size differences among particles is modified as follows:

for $2 \leq D_f \leq 3$,

$$\beta_{DS}(i,j) = \frac{g}{12\mu}\left(\frac{\pi}{6}\right)^{-1/3}\left(\frac{\rho_o - \rho_f}{\rho_f}\right) v_o^{1/3-1/D_f} \left(v_i^{1/D_f} + v_j^{1/D_f}\right)^2 \left|v_i^{(D_f-1)/D_f} - v_j^{(D_f-1)/D_f}\right| \quad \text{(I.9)}$$

for $D_f \leq 2$,

$$\beta_{DS}(i,j) = \frac{g}{12\mu}\left(\frac{\pi}{6}\right)^{-1/3}\left(\frac{\rho_o - \rho_f}{\rho_f}\right) v_o^{4/3-3/D_f} \left(v_i^{1/D_f} + v_j^{1/D_f}\right)^2 \left|v_i^{1/D_f} - v_j^{1/D_f}\right| \quad \text{(I.10)}$$

where v_o and ρ_o are the volume and density of a primary particle.

Although taken into consideration, the fractal dimension is pre-defined based on the aggregation regime and assumed to be unchanged during the agglomeration process. In diffusion-limited aggregation, where the particle-particle attachment efficiency is equal to 1 (particles aggregate upon their first collision), the fractal dimension is in the range of 1.7 to 1.8. When the attachment efficiency is less than 1, the aggregation process is limited by the reaction rate. The fractal dimension in this reaction-limited aggregation is found to be between 1.9 and 2.1.[84] Raychoudhury et al. used the advection-dispersion equation and the modified Smoluchowski model to simulate the transport of NZVI through a packed column.[73] Similarly, Taghavy et al. employed Smoluchowski modeling in conjunction with a Random-Walk Particle Tracking method to investigate the aggregation and movement of NZVI through sphere packings.[78] They both selected D_f = 2.0 for the model to predict the aggregation in the reaction-limited regime. In

contrast, the fractal dimension has been reported to be impacted by many factors, such as fluid velocity and particle size.[85,86] Hence, both the original and the modified Smoluchowski models are unable to predict the morphology of aggregates when they travel in porous media.

Pham et al. utilized the lattice Boltzmann method to obtain the velocity field of fluid in sphere-packed beds and then applied the Lagrangian particle tracking (LPT) method to monitor the movement of NPs in the same media.[76] In LPT, particle propagation is a result of convection by the fluid flow and molecular diffusion of particles.[62] At each LPT timestep, the number of collisions between two particles was computed based on the particle size and distance. Aggregation was then modeled by multiplying the estimated number of collisions with an aggregation probability. The aggregation probability was determined by fitting simulation data to experimental results. The fractal dimension of 2.0 was also used to compute the aggregate size in reaction-limited aggregation. The mean cluster size was found to increase when the particle concentration went up or when the pore velocity decreased. It was also reported that the larger particles were closer to the pore surface than the smaller ones.

Monte Carlo models have also been implemented to simulate the aggregation of nanoparticle suspension at bulk conditions.[87–89] Hul et al. developed an off-lattice coarse-grained Monte Carlo model to investigate the aggregation and transport of NPs in porous media.[59] In this method, at each time step, the movement of each particle was generated with a random angle and a random distance (less than 5nm). Particles were not allowed to jump backward in the streamwise direction. In case a particle moved into the solid phase of the porous medium, it was bounced back to its previous position. When there were collisions between two particles, or between particles and collectors on the solid matrix, aggregation, attachment or detachment occurrence depended on probabilities that were defined by users and did not represent the physicochemical properties of

particles and collectors. With this model, the authors simulated the transport of particles through porous media and examined the effect of porosity, aggregation, attachment, and detachment on the shapes of breakthrough curves by varying probabilities.

Our aim is to build a new Lagrangian particle tracking model to study the aggregation of NPs and the morphology of aggregates in a porous medium, by taking physicochemical interactions among particles into consideration (to avoid using probabilities). This research focuses on simulating the transport of CeO_2 NPs suspended in potassium chloride (KCl) solutions through randomly packed spheres, and examining the effects of the ionic strength, fluid velocity, and particle size on the aggregation kinetics of CeO_2 particles and the morphology (such as fractal dimension and asphericity) of aggregates formed in porous media. The fluid flow through randomly packed spheres is obtained by the lattice Boltzmann method. Then, the NPs are uniformly released in the simulation domain; and their movement as well as agglomeration is examined by a force balance approach and Newton's second law of motion. The particles are subjected to various major forces including gravity, buoyancy, van der Waals attraction, electrostatic repulsion, drag, and random forces. This model keeps track of the positions of all particles at each timestep. When the distance between two particles is less than the primary minimum (where the attraction force between two particles is much larger than the repulsion force), it is assumed that they aggregate.

II. NUMERICAL METHODOLOGY

II.1. Velocity magnitude distribution for flow in porous media

II.1.1. Simulation setup

II.1.1.a. Velocity magnitude distribution for flow in sphere packings and scaffolds

The fluid flow in the pore space of different types of porous media, including sphere packings and scaffolds, was simulated by a lattice Boltzmann method (LBM).[90–93] Once the flow fields were solved, the PDF of the velocity magnitude in such geometries was calculated. The one-sample Kolmogorov-Smirnov (KS) goodness-of-fit tests[94] were utilized to examine if the velocity distributions in such geometries followed any common distribution form. This test is performed using the software EASYFIT version 5.6, which has been often used in prior studies.[95–104] Moreover, the pore space of each porous geometry was investigated using the watershed method,[105,106] to probe whether the pore size distribution is correlated to the velocity distribution.

The investigated sphere packing types included the minimum computational domain for periodic ideally ordered media, i.e., for SC (1 sphere), BCC (2 spheres), FCC (4 spheres), a monodisperse packing of 40 spheres with a diameter of 31.1 μm, a monodisperse packing of 432 spheres with a diameter of 14.1 μm, a bidisperse packing of 600 spheres (200 spheres with a diameter of 17.3 μm and 400 spheres with a diameter of 8.7 μm), a bidisperse packing with 750 spheres (250 spheres with a diameter of 16.1 μm and 500 spheres with a diameter of 8.0 μm) and a tridisperse packing of 1,000 spheres (200 spheres with a diameter of 33.5 μm, 200 spheres with 20.9 μm and 600 spheres with 12.6 μm). The random packings were generated by the code of Baranau and co-workers,[107,108] which applied Lubachevsky–Stillinger generation algorithms.[109–111] Moreover, to improve the accuracy of the pore size characterization for SC, BCC, and FCC, domains containing more spheres than the minimum periodic cell (such as 125 spheres in SC

packing, 250 spheres with BCC, and 256 spheres with FCC) were created. In this way, the effect of the smaller pore space at the boundaries of the minimum computational domain is mitigated. To make this clearer, consider the simple minimum unit cell for the SC in Figure II.1a. If one were to use this image to obtain the pore size, they would obtain 8 pores (at the 8 corners of the cubic domain) with one size, but that size would be 1/4 of the size of the actual pores in the periodic SC domain. With regards to highly porous media typically used in tissue engineering, the velocity distributions for both types of scaffolds – fiber and foam scaffolds – were also studied. The nonwoven fiber mesh scaffold was manufactured by spunbonding technique[112,113] and its digital image was reconstructed by using Microcomputed Tomography and Matlab image processing.[114] The scaffold was not isotropic, because it was manufactured by placing the nonwoven under pressure in one direction (which was the flow direction). Therefore, the LBM was run for the fiber scaffold with the flow in two directions, the *x* and *y* directions.

The digital generation of the structure of the foam scaffolds was aimed to reproduce scaffolds like those induced by the salt leaching method.[115] The foamy scaffolds used herein were created computationally by following these steps: First, a sphere-packing geometry was created with the known location of each sphere by utilizing the sphere-packing generation code. Second, the sphere sizes were increased by 10%; so that the spheres would overlap with their neighbors. Last, the area occupied by spheres was converted to the void phase, and the void area was converted to the solid phase. At this step, the geometry of the foam scaffold was created, as the solid spheres became foam bubbles. In this study, we investigated two foam scaffolds including the one created by monodisperse packing with a bubble foam diameter of 158.8 μm and the other formed by bidisperse packing with a foam bubble diameter of 113.7 μm and 159.2 μm. See Figures II.1, II.2, and II.3 for images of the porous media used.

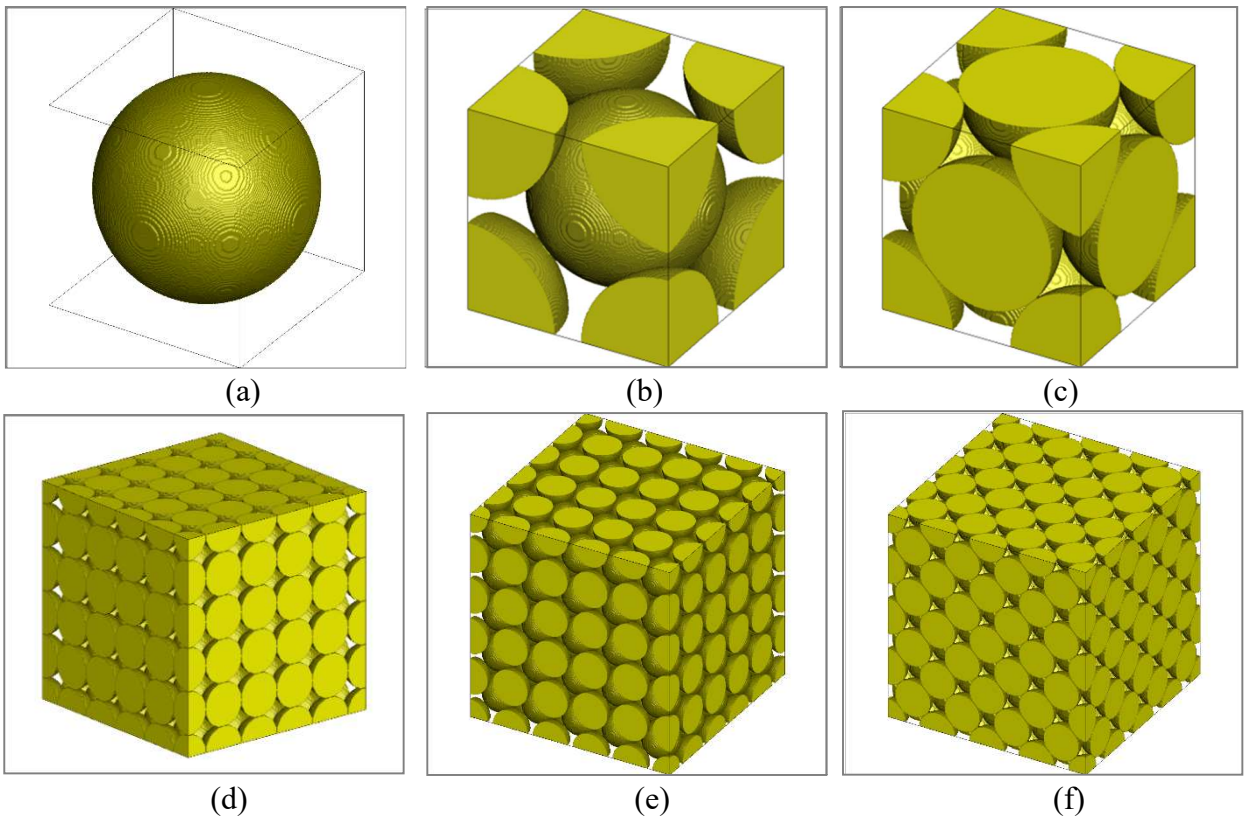


Figure II.1. Geometries of ideally packed spheres including (a) SC - 1 sphere, (b) BCC - 2 spheres, (c) FCC - 4 spheres, (d) SC - 125 spheres, (e) BCC - 250 spheres, and (f) FCC - 256 spheres.

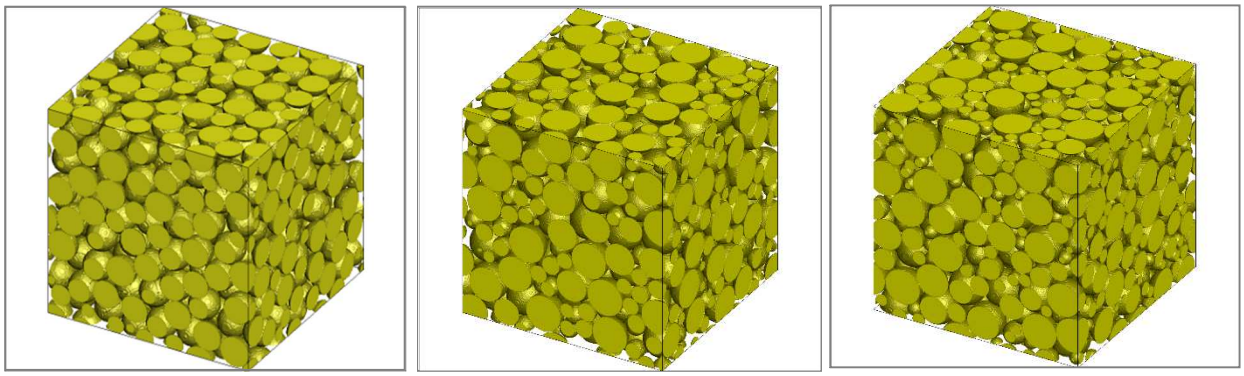
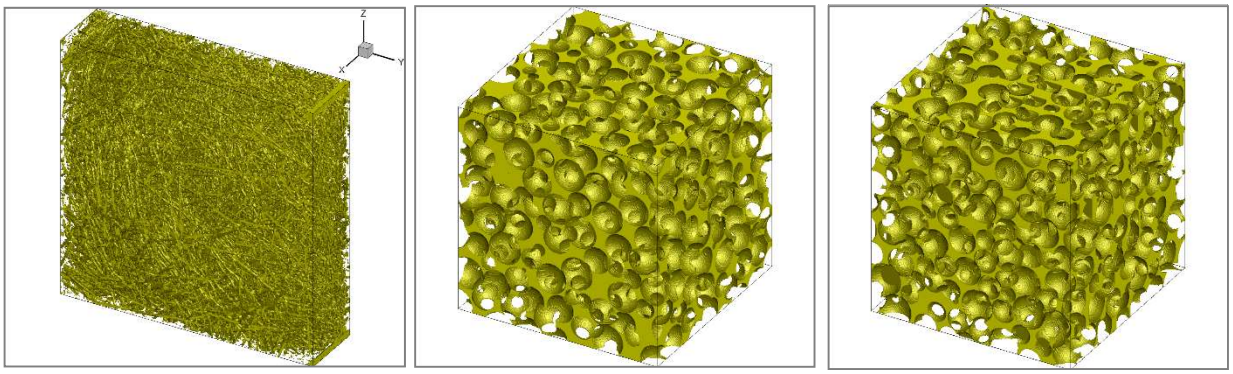


Figure II.2. Geometries of randomly packed spheres containing (a) monodisperse spheres, (b) bidisperse spheres, and (c) tridisperse spheres.

Table II.1. Summary of the geometry characteristics of the porous media investigated in this study.

Geometry	Domain size (μm^3)	Porosity	Mesh size	Size of structural elements (μm)
SC - 1 sphere	100 x 100 x 100	0.48	201 x 201 x 201	100.0 (1 sphere)
SC - 125 spheres	100 x 100 x 100	0.48	401 x 401 x 401	20.0 (125 spheres)
BCC - 2 spheres	100 x 100 x 100	0.32	201 x 201 x 201	86.6 (2 spheres)
BCC - 250 spheres	100 x 100 x 100	0.32	401 x 401 x 401	17.3 (250 spheres)
FCC - 4 spheres	100 x 100 x 100	0.26	201 x 201 x 201	70.7 (4 spheres)
FCC - 256 spheres	100 x 100 x 100	0.26	401 x 401 x 401	17.7 (256 spheres)
Monodisperse packing 1	100 x 100 x 100	0.37	401 x 401 x 401	31.1 (40 spheres)
Monodisperse packing 2	100 x 100 x 100	0.37	401 x 401 x 401	14.1 (432 spheres)
Bidisperse packing 1	100 x 100 x 100	0.32	401 x 401 x 401	17.3 (200 spheres) 8.7 (400 spheres)
Bidisperse packing 2	100 x 100 x 100	0.32	401 x 401 x 401	16.1 (250 spheres) 8.0 (500 spheres)
Tridisperse packing	200 x 200 x 200	0.31	501 x 501 x 501	33.5 (200 spheres) 20.9 (200 spheres) 12.6 (600 spheres)
Fiber scaffold - *x* direction	5400 x 5400 x 1360	0.85	541 x 541 x 137	34.8 ± 1.85 (average fiber diameter)
Fiber scaffold - *y* direction	5400 x 1360 x 5400	0.85	541 x 137 x 541	34.8 ± 1.85 (average fiber diameter)
Monodisperse foam scaffold	1000 x 1000 x 1000	0.80	401 x 401 x 401	158.8 (400 bubbles)
Bidisperse foam scaffold	1000 x 1000 x 1000	0.82	401 x 401 x 401	113.7 (300 bubbles) 159.2 (300 bubbles)



(a) (b) (c)

Figure II.3. Geometries of (a) fiber scaffold, (b) monodisperse foam scaffold, and (c) bidisperse foam scaffold.

The detailed characteristics of all the porous media were summarized in Table II.1. The domain size of sphere packings and foam scaffolds was chosen to ensure that they are representative of the porous media. This means that the volume of the simulation box was not smaller than the representative elementary volume of the porous media.[116,117] This was established by measuring the average velocity of a small cube starting from the center of the domain and then extended until it reached the whole volume of the domain. The volume was considered representative of the average volume when both the streamwise and spanwise velocities were not changing as the computational domain size increased.[65] Figure II.4 is an example of the representative volume analysis for random sphere packing containing 432 spheres. The velocities in x, y, and z directions were stable when the length of the domain was larger than 40 μm, indicating that the simulation box with a length of 40 μm was representative. Since the box, sized 100 x 100 x 100 μm^3, contained 432 spheres, the domain, sized 40 x 40 x 40 μm^3, was packed with $432/(100/40)^3 = 28.8$ spheres. Therefore, both sphere packings packed with 40 and 432 spheres were representative.

The selection of mesh size for each domain was based on grid independence analysis, which meant that the pore average velocity and the full velocity distribution of the fluid would not change with a finer mesh size than the selected one. (See Appendix A.1 for examples of the grid

independence analysis for FCC and monodisperse sphere packing with 432 spheres). The flow through porous media was simulated using water at room temperature with a viscosity of 0.001 Pa.s and a superficial velocity of 0.1cm/s. These conditions ensured that the flow was in the Darcy regime, with laminar fluid flow.

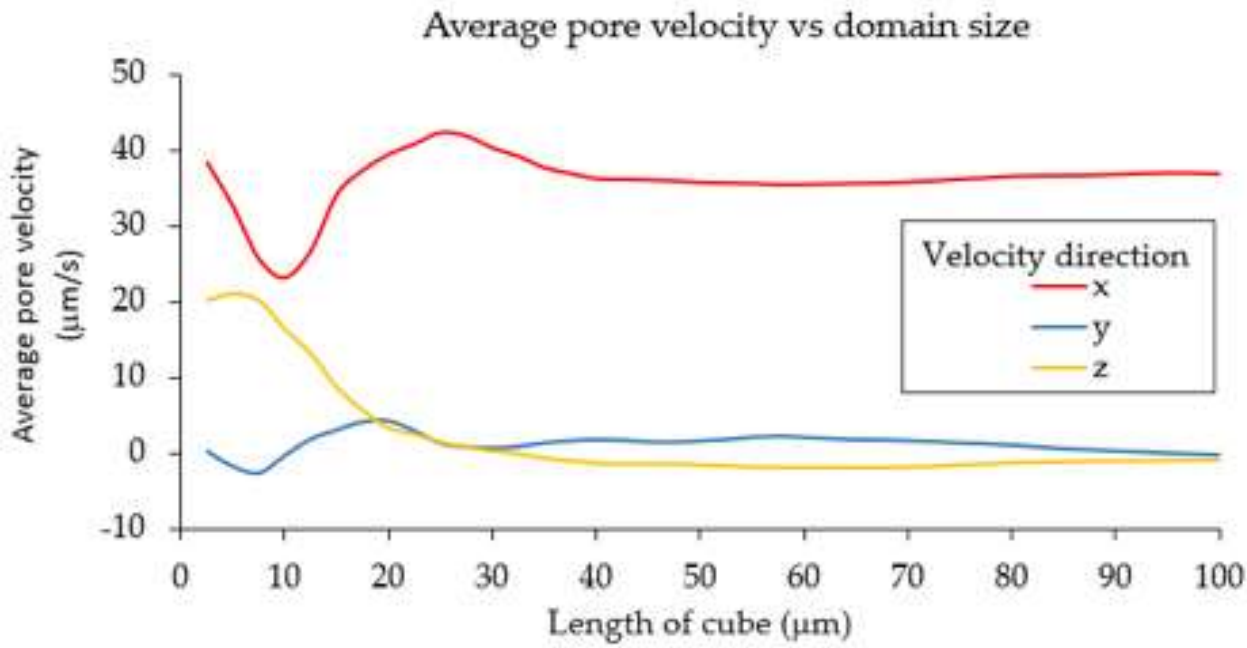
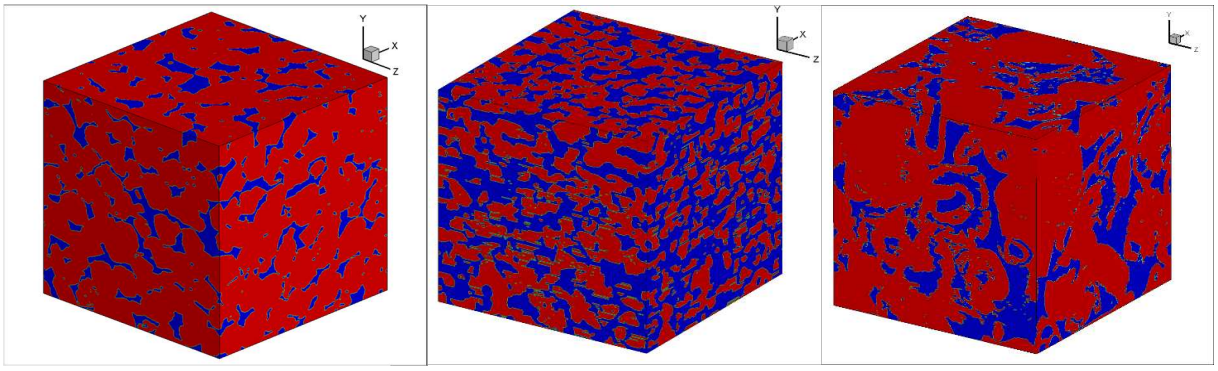


Figure II.4. Pore velocity calculated by averaging over an increasing part of the domain volume. The average pore velocity changed with the domain size when water at room temperature flows through the monodisperse sphere packing, consisting of 432 spheres, in x direction.

II.1.1.b. Relationship between pore fluid velocity distribution and pore size distribution

The velocity distributions in real porous media such as sphere packings with random configurations (monodisperse, bidisperse, and tridisperse as seen in Figure II.2), a fiber scaffold (Figure II.3a), sandstones (Bentheimer,[118] Berea, Doddington,[119] S1[120] and S2[120]), a carbonate sample (C1),[120] a synthetic silica sample (A1),[120] were also investigated to check if they follow the same distribution model that the velocity magnitude distributions in sphere packings and scaffolds do. In this study, it is also examined if the pore-size and velocity magnitude distributions are statistically identical by using the two-sample KS goodness of fit test.[121–124]

The Bentheimer and Doddington samples with a grid size of 300x300x300 were extracted from digital images of larger samples obtained through the literature.[118,119,125] The Berea sandstone was created from micro-computed tomography (μCT) images obtained by our research group with a mesh size of 300 x 300 x 300.[6] We also investigated two sandstone samples (S1 and S2), a synthetic silica sample, A1, with a mesh size of 300 x 300 x 300, and a carbonate sample, C1, with a mesh size of 400 x 400 x 400, which was available through a Dissertation.[120] Our LBM code has periodic boundary conditions; therefore, these geometries were flipped into three directions (x, y, and z) to ensure continuous flow through the domain boundaries.[6,126] Consequently, Bentheimer, Doddington, Berea, S1 and S2 domains for LBM runs had a mesh size of 599 x 599 x 599 while the C1 domain had a mesh size of 799 x 799 x 799. In addition, dead ends and isolated pores in all the investigated porous media were removed. Further information about the geometries used for determining the relationship between pore-size and velocity magnitude distributions was summarized in Table II.2. In addition, Figure II.5a, b, and c illustrate the images (prior being flipped) of sandstone (S1), synthetic silica (A1), and carbonate (C1) samples that were not flipped in three directions.



(a) (b) (c)

Figure II.5. Geometries of (a) a sandstone - S1, (b) synthetic silica - A1, and (c) carbonate - C1. The red color represents the solid phase, while the blue one indicates the pore space of porous media.

Table II.2. Details of domains of all porous media examined in this work and results for two-sample KS tests for the pore volume and velocity magnitude distributions. The pore volumes and local velocity magnitudes in a porous type will be distributed by the same distribution if the two-sample KS test statistic is lower than 0.152, which is the critical value at the significance level of 0.2.

Geometry	**Domain size (μm^3)**	**Porosity (%)**	**Sample resolution**	**Size of structural elements (μm)**	**Calculated two-sample KS test statistic**
Berea	2691 x 2691 x 2691	13.5	599 x 599 x 599	-	0.059
Sandstone S1	5192 x 5192 x 5192	14.1	599 x 599 x 599	-	0.011
Bentheimer	1796 x 1796 x 1796	19.5	599 x 599 x 599	-	0.034
Doddington	1610 x 1610 x 1610	21.6	599 x 599 x 599	-	0.113
Carbonate C1	2274 x 2274 x 2274	23.3	799 x 799 x 799	-	0.053
Sandstone S2	2964 x 2964 x 2964	24.6	599 x 599 x 599	-	0.019
Tridisperse packing	200 x 200 x 200	31.3	501 x 501 x 501	33.5 (200 spheres) 20.9 (200 spheres) 12.6 (600 spheres)	0.058
Bidisperse packing	100 x 100 x 100	32.2	401 x 401 x 401	16.1 (250 spheres) 8.0 (500 spheres)	0.058
Monodisperse packing	100 x 100 x 100	37.1	401 x 401 x 401	14.1 (432 spheres)	0.110
Synthetic silica A1	2302 x 2302 x 2302	42.9	599 x 599 x 599	-	0.036
Fiber scaffold - *x* direction	5400 x 5400 x 1360	85.0	541 x 541 x 137	34.8 ± 1.85 (average fiber diameter)	0.066
Fiber scaffold - *y* direction	5400 x 1360 x 5400	85.0	541 x 137 x 541	34.8 ± 1.85 (average fiber diameter)	0.042

II.1.2. Lattice Boltzmann method

Many approaches can simulate the flow of fluid in porous media such as continuum, molecular dynamics, and lattice Boltzmann method. In the continuum approach, to solve the flow field, it is important to solve the ordinary and partial differential equations, obtained by applying conservation equations of momentum, heat, and mass for an infinitesimal control volume. However, it is very challenging to solve such equations for flow in porous media due to complex boundary conditions as well as complicated geometries. On the other hand, the porous medium can be considered made of atoms or molecules; and we can utilize molecular dynamics to simulate the flow of fluid in such a medium. However, this method is just applicable to the microscale. Therefore, the lattice Boltzmann method has been widely used to solve the flow fields in porous media because it could bridge the gap between continuum and molecular approaches. In this method, a group of particles is considered a unit that is represented by a distribution function. Each unit is just allowed to travel in certain defined directions. Thus, it has many advantages; for example, it is applied for flow in complex domains or multi-phase flow within the mesoscopic scale. Moreover, it can be easily paralleled, which significantly reduces the computational cost.

II.1.2.a. Algorithm

The flow of fluids through porous media was simulated by an in-house written code that is based on the lattice Boltzmann method (LBM). In this method, the porous medium domain is meshed into lattice points of two types: solid nodes and fluid nodes. The basis of LBM is to solve iteratively the Boltzmann equation - a model showing the change of the particle distribution function at every time step when fluid particles move between the fluid nodes in specified directions.[90,92] These directions are determined by the lattice model, commonly designated as DmQn where m is the dimensionality and n is the number of directions that the particles are

allowed to travel.[6,91,115] Based on accuracy tests that were conducted for different lattice models, including D3Q15, D3Q19, and D3Q21,[127] and the validation of the LBM code for porous media,[115,65] the lattice model D3Q15 is selected in this study since it provides accurate results using less computational resources. Moreover, the movement of fluid particles is considered to include three steps - streaming, collision, and forcing, and is represented as follows:

$$\underbrace{f_i(\vec{x}+\vec{e}_i\Delta t, t+\Delta t) = f_i(\vec{x},t)}_{Streaming} + \underbrace{\Omega_i(\vec{x},t)}_{Collision} \pm \underbrace{ff_i}_{Forcing} . \tag{II.1}$$

In the streaming step, a group of fluid particles, having the distribution function f_i, moves along the direction i with velocity $\vec{e}_i$ from position $\vec{x}$ to $\overrightarrow{(x}+\vec{e}_i\Delta t)$ during a time step Δt. The collision among particles during streaming is characterized by the Bhatnagar-Gross-Krook model (BGK) to determine the collision operator Ω_i,[6,91,115] given by

$$\Omega_i(\vec{x},t) = -\frac{1}{\tau_r}\left(f_i - f_i^{eq}\right). \tag{II.2}$$

The relaxation time τ_r and equilibrium distribution function f_i^{eq} are calculated as follows:

$$\nu = \frac{1}{3}(\tau_r - \frac{1}{2}) \tag{II.3}$$

$$f_i^{eq}(\vec{x}) = w_i\rho\left[1 + \frac{\vec{e}_i.\vec{U}}{c^2} + \frac{(\vec{e}_i.\vec{U})^2}{2c^4} - \frac{\vec{U}^2}{2c^2}\right] \tag{II.4}$$

where ν is the kinetic viscosity, w_i is a lattice specific weighing factor, c is the speed of sound and $\vec{U}$ is the macroscopic velocity.[6,90,91,115] The last term ff_i corresponds to the pressure drop occurring during the streaming step. In addition, the mass and momentum conservation equations are used to determine the fluid velocity at each one of the lattice points[6,91,115]

$$\rho = \sum_{i=0}^{n} f_i \tag{II.5}$$

$$\rho\vec{U} = \sum_{i=0}^{n} f_i \, \vec{e}_i. \tag{II.6}$$

With regards to the boundary conditions, the no-slip boundary condition together with the bounce-back technique was applied at the solid-fluid surfaces.[6,91] In other words, if a fluid particle moved towards and hit the wall, it would return to its original fluid node in the opposite direction. The periodic boundary condition was also used in the three space directions *x*, *y* and *z* to simulate an infinite domain.[65]

II.1.2.b. Code validation and verification

To verify the LBM code, we calculated the permeability of periodic simple cubic (SC), face-centered cubic (FCC), or body-centered cubic (BCC) porous media and then compared our results with those of two other groups. The size of the simulation box used for each geometry was 100 × 100 × 100 μm; and the domain consisted of 201 nodes in each x, y, and z direction. The LBM was used to run for different values of the forcing factor (the pressure drop over the domain length), resulting in different velocity fields. Next, Darcy's empirical law, showing the relation between the pressure drop $\frac{\Delta P}{L}$ through the flow and the superficial fluid velocity U_s was applied to determine the permeability, k, of different packing arrays.[128] Darcy's law is expressed as:

$$U_s = -\frac{k}{\mu}\frac{\Delta P}{L} \tag{II.7}$$

where μ is the dynamic viscosity of the fluid. The k value was then divided by the sphere diameter squared to obtain a dimensionless permeability. Our results for the dimensionless permeability of different geometries, including SC, FCC, and BCC, agreed well with the ones of Chapman and Higdon [129] that were obtained by solving the unsteady Stokes equations for the microscopic flow. Moreover, Eshghinejadfard et al. [130] used their own LBM code to calculate the permeability of

FCC and BCC and showed similar results to ours. The details of the comparison are shown in Table II.3.

Table II.3. Comparison of the results for dimensionless permeability with prior results. The reported error is the relative absolute error compared to references.

Geometry	Porosity	Dimensionless Permeability (k/d_p^2)			Relative Error (%) Compared to	
		Present Results	Reference (1) [129]	Reference (2) [130]	Reference (1) [129]	Reference (2) [130]
FCC	0.26	1.75E-04	1.74E-04	1.70E-04	0.76%	2.96%
BCC	0.32	5.10E-04	5.02E-04	5.10E-04	1.49%	0.10%
SC	0.48	2.61E-03	2.53E-03		3.10%	

Moreover, the LBM code was verified for laminar flow through different sphere packing types (SC, BCC, and FCC) of fixed-bed columns. This flow is usually modeled by the Blake–Kozeny (BK) equation,[128] which shows the correlation between the pressure drop over the length with the superficial velocity:

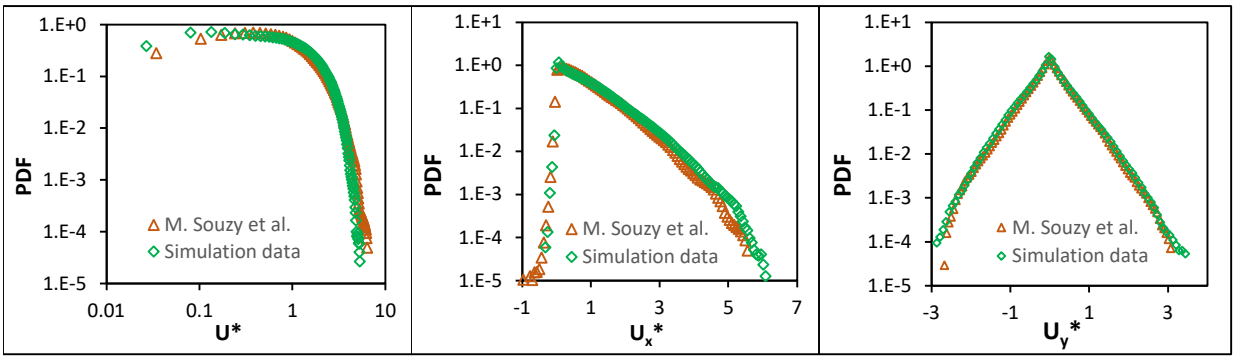
$$\mathrm{U}_s = \frac{\Delta P}{L}\frac{d_p^2}{150\mu}\frac{\varepsilon^3}{(1-\varepsilon)^2}. \tag{II.8}$$

The results are presented in Table II.4, revealing that SC followed the BK correlation with a less than 1% error, while other types of packing deviated from the BK equation with errors of 8.08% and 17.7% for BCC and FCC, respectively. In prior work out of our laboratory, this code was also validated against flow cases with known analytical solutions, such as flow in a slit, in a pipe, and flow around an infinite array of spheres [115].

Table II.4. The lattice Boltzmann method (LBM) code verification by Blake–Kozeny equation. The reported error is the relative absolute error for the calculated superficial velocity.

Parameter	SC	BCC	FCC	RPS
Porosity, ϕ	0.48	0.32	0.26	0.37
Spheres' diameter, d_p (cm)	1.00E-03	8.66E-03	7.07E-03	1.41E-03
Pressure drop, $\Delta P/L$ (g/cm^2 s^2)	3.66E+03	1.67E+04	5.93E+04	5.33E+05
Pore velocity (cm/s)	2.00E-01	2.00E-01	2.00E-01	2.00E-01
Superficial velocity, U_s (cm/s)	9.53E-02	6.40E-02	5.19E-02	7.42E-02
Blake–Kozeny velocity (cm/s)	9.62E-02	5.92E-02	6.31E-02	9.08E-02
Relative error	0.91%	8.08%	17.70%	18.26%

To further validate the code, the full three-dimensional (3D) velocity distribution of Trident X-100 flowing through randomly packed spheres obtained from our code was compared to experimental data obtained by Souzy et al.,[1] as illustrated in Figure II.6a. Figure II.6a is a demonstration of the distribution of the normalized pore velocity magnitude $U^* = \frac{U}{\overline{U}}$, where U is the pore velocity magnitude and $\overline{U}$ is the mean pore velocity magnitude, while Figures II.6b and Figure II.6c show how the normalized longitudinal velocity $U_x^* = \frac{U_x}{\overline{U}}$ and axial velocity $U_y^* = \frac{U_y}{\overline{U}}$ were distributed, where U_x and U_y are velocities in the x and y directions, respectively. There was very good agreement between the present results and the experimental results of Souzy et al.,[1] as seen in Figure II.6. The experimental data presented in Figure II.6 were reported to be in good agreement with results reported elsewhere,[8,22,131,132] meaning that the LBM results agree with experiments from different laboratories.



(a) (b) (c)

Figure II.6. (a) Details of the velocity magnitude distributions of the flow through packed bed containing monodisperse spheres (sphere diameter = 0.2 cm, porosity = 37%, average pore velocity magnitude $\overline{U}$= 1.27 x 10^{-2} cm/s) in random configuration that was measured by experiment (Souzy et al.[1]) and the present LBM simulation (green data points), (b) streamwise velocity, and (c) spanwise velocity. It is seen that the LBM computation results agree with the experiments not only in the mean, but also in the whole range of the velocity distribution and in both the streamwise and spanwise directions.

II.1.3. Probability density function for velocity magnitude

Applying LBM can solve the velocity field of flow through a porous medium, providing information on the velocity at each fluid node within the domain. The velocity magnitude of the 3D velocity vector at each fluid node, $U = \sqrt{U_x^2 + U_y^2 + U_z^2}$, is examined where U_x, U_y, U_z are the velocity components in *x, y* and *z* directions, respectively. It is then normalized by dividing by the mean pore velocity magnitude, $\overline{U}$, as

$$U^* = \frac{U}{\overline{U}} . \qquad \text{(II.9)}$$

The range of the normalized velocity magnitude is divided into 100 equal bins and the velocity PDF is found based on the fractional occurrence over the bin width.

II.1.4. Pore-size calculation - Watershed segmentation

The geometry of the porous media used was converted to a binary image (the value for solid pixels was 1 and the value for void pixels was 0) and was divided into N_x two-dimensional slices perpendicular to the flow direction in the *x*-axis (N_x is the number of the lattice mesh points

in the *x*-axis). The watershed method was applied for each of the 2D planes to identify the pores; and the calculated pore size was the area of each pore in each 2D slice.

In general, the watershed method is an image-processing method for the segmentation of connected objects.[105,106,133,134] This method assumes that the void space has depth and the depth at each void pixel is proportional to the distance from that void pixel to the nearest solid one. It is assumed that the void area in each plane has the shape of two connected circles; hence, two neighboring void objects are considered as two holes with the deepest areas located at the centers of the holes. These two holes are defined as *catchment basins*. Fluid coming from the bottom of a basin (i.e., the center of the hole) is in contact with fluid coming from neighboring basins and the first line of contact is called the watershed ridge line. In the algorithm, the distance from each void pixel to the nearest solid one, which is considered as the depth of each pixel, is calculated, and the line with the steepest descent is determined as the watershed ridge line. Consequently, two void objects or two pores are separated by the watershed ridge line; and the area of each of them can be estimated. Further information about this algorithm can be found elsewhere.[105,106,133] FigureII.7 is a demonstration of how the watershed segmentation algorithm extracted pores in 2D planes for cases of FCC, monodisperse sphere packing, and monodisperse foam scaffold.

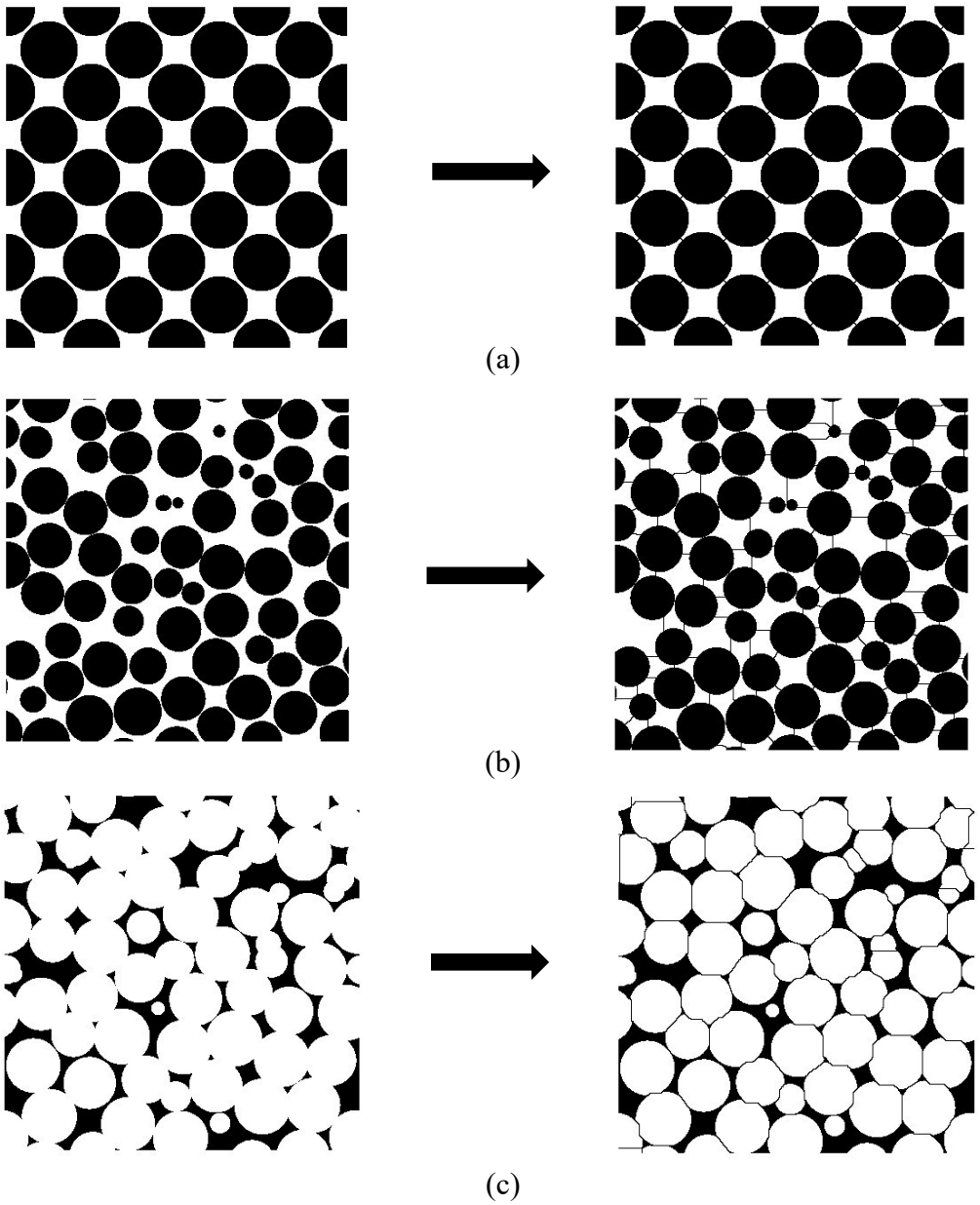


Figure II.7. Examples of 2D pore extraction by using the watershed method for (a) FCC, (b) packing of monodisperse spheres, and (c) monodisperse foam scaffold. The black color indicates the solid matrix and the white color indicates the void pore space. The thin black straight lines appearing in the panels to the right indicate pore boundaries found using the watershed algorithm.

II.1.5. Pore-size calculation– Maximal ball (MB) algorithm

The maximal ball algorithm[134–138] is one of the most reliable and well-known methods to describe the pore structure of porous media. The pore-network extracting code, based on the maximal ball algorithm and developed by the research group of Pore-Scale Modelling and Imaging

at the Department of Earth and Science Engineering, Imperial College London (https://github.com/ImperialCollegeLondon/pnextract), is applied to determine the size of each pore in porous media. In this method, the set of the largest spheres centered at each voxel in the pore space and tangent to the grain is generated. The balls inscribed in other larger balls are then eliminated; therefore, the balls touching the solid boundary and containing at least one voxel that does not belong to other balls were used to describe the pore space of the geometry. The two connected pores have two sets of MBs; and those sets have common MBs which are used to define the throat of the two pores. The volume of a pore (or throat) is the total number of voxels in that pore (or throat).

The pore volume estimated by the MB algorithm is then divided by the mean pore volume $V^* = V/\bar{V}$, where V is the pore volume, $\bar{V}$ is the average pore volume, and $V^*$is the dimensionless or normalized pore volume. The pore volume PDF is determined by the same method used to determine the velocity magnitude PDF.

II.2. Hydrodynamic dispersivity based on Lagrangian Peclet number

II.2.1. Simulation setup

Numerical experiments were conducted for two types of porous media, with infinite arrays of spheres packed in the FCC and randomly packed spheres (RPS). The computational domain size was the same for both types of porous media (100 × 100 × 100 μm), but the diameter of the spheres was different. The FCC domain was the minimum periodic cell for the FCC configuration, which contained four spheres with a diameter of 70.76 μm, whereas the simulation box for randomly packed spheres (or the monodisperse sphere packing with random configuration) consisted of 432 spheres of a 14.06 μm diameter each. In the RPS configuration, 432 spheres were

packed in a cubic domain by the Lubachevsky–Stillinger simulation algorithm.[109,111,126] The images of the two packing types are shown in Figures II.1c and II.2a.

The simulation boxes for FCC and RPS were discretized into LBM lattice nodes. The number of lattice nodes greatly affected the accuracy of the results, as did the computational time. Details of the grid independence analysis that was conducted are presented in Appendix A.1. Finally, the number of nodes was chosen to balance accuracy with computational resources so that the FCC domain was meshed with a 201 × 201 × 201 mesh, while a 401 × 401 × 401 mesh was applied for the RPS domain. Next, the LBM code in conjunction with a D3Q15 lattice velocity model was implemented to obtain the flow field of water at room temperature through porous media, with the pore velocities 0, 50, 100, 200, 500, 1000, 2000, 3000, and 4000 μm/s. Next, 50,000 NPs were released in the flow domain at randomly and uniformly selected positions in the pore space, and the velocity and trajectory of each of these particles were tracked using the LPT algorithm, as already discussed. For each velocity field, different LPT runs with different values of the particle Schmidt number (*Sc* = 100, 1000, 7080, and 10,000) were performed, providing data for *Sc* covering two orders of magnitude. Moreover, the range of the Schmidt number was chosen to cover particles with diameters from 0.22 to 5 nm, and *Sc* = 7080 was the Schmidt number of Janus particles (d_p = 3.6 nm) in water, which has been investigated in prior work to lower oil-water interfacial tension [29]. Thus, thirty-six LBM/LPT simulations were conducted for each one of the two porous media configurations.

II.2.2. Lagrangian Particle Tracking

LPT is an effective method to track the trajectories of particles in a Lagrangian framework while they move in a flow field. However, there are several assumptions when this method is applied. Firstly, the nanoparticles (NPs) are considered passive, so the presence of NPs does not

modify the flow field. Secondly, the NP concentration is low, so the particle-particle interactions are not taken into consideration. Thirdly, the NP–wall interactions and the adsorption of NPs on the wall of the packing spheres are neglected. In short, there are just two kinds of transport contributing to the motion of the NPs—the convection by the flow field and the molecular diffusion of NPs. Therefore, the equation of motion of the NPs can be expressed by:

$$\vec{X}_{t+\Delta t} = \vec{X}_t + \Delta t.\vec{U}_t + \Delta\vec{X}_m \tag{II.10}$$

where $\vec{X}_t$ is the position of a NP at time *t* and $\vec{X}_{t+\Delta t}$ is the new position of that NP in the next time step $(t + \Delta t)$.[93,139] The velocity of the nanoparticle $\vec{U}_t$, which leads to the convective transport, can be obtained from the LBM flow field using a trilinear interpolation scheme to calculate the velocity of the NPs, $\vec{U}_t$, at its position between the grid nodes.[6,93,139] The second motion $\Delta\vec{X}_m$, the molecular diffusion, of the particles is estimated by Einstein's theory for Brownian motion. After moving because of convection, each particle undertakes a Brownian motion jump that is calculated according to a random number drawn from a normal distribution with a zero mean (because the Brownian motion is equally probable to be in the positive or the negative direction) and a standard deviation σ determined by the NP diffusivity D_m. The standard deviation in each space direction is found as follows:

$$\sigma = \sqrt{2D_m\Delta t} = \sqrt{\frac{2\nu\Delta t}{Sc}} \tag{II.11}$$

where the Schmidt number *Sc* is the ratio of the fluid kinematic viscosity ν and the NP molecular diffusivity [128]. At this point, by estimating the traveling distance of all NPs caused by convection and Brownian motion, the position of each particle can be tracked at every single time step. In the case that the NPs move into the solid packing after a time step, they are bounced back to their current position in the fluid phase. To be more specific, the new position of each particle in every

single time step was checked, and if it was inside the grains, the new position was not updated. The time step in LPT was chosen so that NPs never moved more than one-half of the LBM mesh unit. We determined the timestep by ensuring that any LPT particle that moved with the maximum fluid velocity in every time step plus the maximum Brownian motion in the same direction did not move more than half of the lattice unit. This algorithm has been validated with Taylor–Aris diffusion theory and has shown excellent results [139].

II.2.3. Lagrangian time scale and Velocity Autocorrelation Function

A Lagrangian length scale, l^L, is determined based on the relevant Lagrangian time scale and the average velocity, u_p, of all NPs, which is equal to the average pore velocity of $l^L = \tau^L u_p$. Taylor defined the Lagrangian time scale as [140]:

$$\tau^L = \int_0^\infty R^L(\tau) d\tau \tag{II.12}$$

where $R^L(\tau)$ is the velocity autocorrelation function (VACF). While Taylor's work was focused on turbulent velocity fluctuations along the trajectories of fluid particles, the analogous VACF for porous media would be based on the velocity fluctuations of the NP velocities relative to the average NP velocity at each time step. Furthermore, since the NPs move with both Brownian motion and convection, the VACF should be the material autocorrelation function, as proposed by Saffman.[141] In that work, it was recognized that a scalar marker does not follow the same path as a fluid particle, since it can move off a streamline because of Brownian diffusion. The VACF would need to be defined with the velocity of a diffusing particle, instead of the velocity of a fluid particle, as follows:

$$R^L(t, t_0) = \frac{\overline{V_j'(t) V_j'(t_0)}}{\overline{V_j'^2(t)}^{1/2} \overline{V_j'^2(t_0)}^{1/2}} \tag{II.13}$$

where t_0 is the initial time, and $V_j'(t)$ is the velocity fluctuation of NP j, $V_j'(t) = V_j(t) - \bar{V}_j(t)$. This equation has been used for dispersion in turbulent flow to estimate the Lagrangian time scale.[142–146] At small times after the NP release, the VACF is almost equal to unity, because the initial velocity is correlated with itself; however, over time, the VACF drops to zero. This happens because the random molecular movement of the particles takes them away from their original velocity streamlines, and the velocity of NPs as time advances does not correlate with the initial velocity of the NPs.[140,142,143] Hence, the Lagrangian time scale represents the time that the particles need to "forget" the velocity of the location from where they came, and it is appropriate to be used to cover the effect of molecular diffusion in the dispersion.

II.2.4. Hydrodynamic dispersion coefficient

The longitudinal hydrodynamic dispersion coefficient is determined based on the positional variance method:[139,147]

$$D_L = \lim_{t\to\infty} \frac{1}{2}.\frac{d\sigma^2}{dt} \qquad \text{(II.14)}$$

where the position variance σ^2 is calculated in each direction as:

$$\sigma^2 = \overline{(X_J - \bar{X}_J)^2}. \qquad \text{(II.15)}$$

The dispersion coefficient, calculated for the flow velocity equal to 0 was considered as the effective molecular dispersion D_m'.

II.3. Aggregation of nanoparticles

II.3.1. Simulation set up

II.3.1.a. Aggregation of nanoparticles in bulk

Aggregation of 10mg/L CeO_2 particles in various KCl solutions including 0.001M, 0.02M, 0.1M, 0.15M, and 0.2M was simulated by our Lagrangian Particle Tracking model based on the

force balance approach (LPT/FB), and was compared with the experimental results of Li et al.[148] 10,544 primary particles were randomly released in the simulation box, sized 0.3 x 0.3 x 0.3 mm^3; and the radius of a primary particle was 95nm. (See Appendix B.2 for the simulation box size independence analysis). Parameters obtained from experiments, including temperature $T = 298$ K, the relative dielectric constant of the liquid $\varepsilon = 78.5$ (for water),[148] surface potential $\psi = 45$ mV,[149] and Hamaker constant $A = 5.57\times10^{-20}$ J,[148–150] were used in this study. The mean hydrodynamic radius of particles and the fractal dimension of aggregates were computed over time and compared with the experimental results.

II.3.1.b. Aggregation of nanoparticles in porous media

The LBM code was employed to simulate the flow of potassium chloride aqueous solutions through randomly packed spheres, with a porosity of 37%, at different average pore velocities. The porous medium was a representative simulation box, sized 0.419 x 0.419 x 0.419 mm^3; and it contained 40 spheres, each with a diameter of 130.3μm. The number of spheres was chosen based on a representative elementary volume analysis, carried out in our previous study.[65] The average hydraulic diameter of the sphere packing was 51.3 μm, which is equivalent to around 49 lattice units (one lattice unit is defined as the grid resolution, *dx*). The simulation domain was meshed into 401 x 401 x 401 grid points (see the grid independence in Appendix B.4). At this stage, velocity fields of KCl solutions through randomly packed spheres were obtained. The mean pore velocities in the streamwise direction investigated in this study were 50, 100, 200, 500, and 2000 μm/s.

The aggregation model (LPT/FB) was then applied to simulate the movement and aggregation of CeO_2 particles in KCl solutions through the sphere packing with a random configuration. Table II.5 is a summary of the numerical experiments that were performed to

investigate the effects of the ionic strength, the pore velocity, and the particle size on the aggregation process. In the simulations, all particles were uniformly released in the porous domain, while the number of particles was calculated to ensure that the particle concentration was 10 mg/L.

Table II.5. Details of simulations performed by the multiscale model for aggregation and movement of CeO_2 nanoparticles in randomly packed spheres with the presence of ionic strength.

Effects of	Number of particles	KCl concentration (M)	Particle radius (nm)	Pore velocity (μm/s)
Ionic strength	10,544	0.001	95	500
	10,544	0.02	95	500
	10,544	0.2	95	500
Pore velocity in diffusion-limited aggregation	10,544	0.2	95	50
	10,544	0.2	95	100
	10,544	0.2	95	200
	10,544	0.2	95	500
	10,544	0.2	95	2000
Pore velocity in reaction-limited aggregation	10,544	0.02	95	50
	10,544	0.02	95	100
	10,544	0.02	95	200
	10,544	0.02	95	500
	10,544	0.02	95	2000
Particle size in diffusion-limited aggregation	6,792	0.2	110	500
	7,809	0.2	105	500
	10,544	0.2	95	500
	14,720	0.2	85	500
Particle size in reaction-limited aggregation	6,792	0.02	110	500
	7,809	0.02	105	500
	10,544	0.02	95	500
	14,720	0.02	85	500

II.3.2. Lagrangian particle tracking based on force balance approach (LPT/FB)

The movement of nanoparticles in porous media is investigated by applying a force balance, based on Newton's second law of motion. The rate of change in momentum of a particle is considered proportional to the total forces applied on that particle, given as:[50,151]

$$m\frac{dV}{dt} = F_g + F_b + F_d + F_r + F_e + F_{vdW} \tag{II.16}$$

where m and V are the mass and velocity of the particle, respectively.

The various major forces exerted on NPs are the gravity force F_g,[151] buoyancy force F_b,[151] drag force F_d,[151,152] random force F_r,[153] electrostatic repulsion force F_e,[154–156] and van der Waals force F_{vdW}.[154–156] While the gravity force is downward and caused by the mass of the particle itself, the buoyancy force is an upward force generated by the fluid on the immersed particle; and they are calculated as follows:

$$F_g = \frac{\pi}{6}\rho_p g D^3 \tag{II.17}$$

$$F_b = \frac{\pi}{6}\rho g D^3 \tag{II.18}$$

where ρ_p and ρ are the densities of particles and fluid; g represents the gravity constant; and D denotes the particle diameter.[151]

While particles move in a fluid flow field, the particle velocity and the fluid velocity are not the same. The difference in velocities generates the drag force on a particle, calculated as follows:[151]

$$F_d = 3\pi\mu D(U - V) \tag{II.19}$$

where μ is the dynamic viscosity of the fluid; U is the fluid velocity, obtained by interpolating the LBM velocity field; and V is the particle velocity.

While particles move in a certain fluid, the fluid molecules collide with the particles and exert a force on the particles. The net effect of this kind of collisions from fluid molecules to particles is represented by the random force. It depends on the particle size as well as the fluid viscosity, and is given as follows:

$$F_r = \sqrt{\frac{6\pi k_B T D \mu}{\Delta t}}\xi \tag{II.20}$$

where k_B is the Boltzmann constant; T is the temperature, ξ is an independent Gaussian random number with zero mean and unit variance; and Δt is the simulation timestep.[152]

The electrostatic force is computed as follows:

$$F_e = -2\pi\varepsilon\varepsilon_0\psi^2 R\left(\frac{ke^{-kh}}{1+e^{-kh}}\right) \tag{II.21}$$

$$k = \sqrt{\frac{2N_A I e^2}{\varepsilon\varepsilon_0 k_B T}} \tag{II.22}$$

where ε is the relative dielectric constant of the fluid; ε_0 is the dielectric permittivity of a vacuum, 8.854×10^{-12} $CV^{-1}m^{-1}$; ψ is the surface potential of particles in the solution; k is the inverse Debye length; N_A is Avogaro's number, 6.02×10^{-23} mol^{-1}; I is the ionic strength; and e is the unit charge, 1.602×10^{-19} C.[156]

The van der Waals attraction force between two particles is the result of interactions between instantaneous dipoles of atoms, which are created by the orbiting electrons. This force is distance-dependent; therefore, it quickly vanishes if interacting particles are far away from each other. It can be estimated as below:[151,156]

$$F_{vdW} = \frac{32A}{3}\left[\frac{R^6}{(2R+h)^3(4Rh+h^2)^2}\right] \quad \text{(II.23)}$$

where A is Hamaker constant; R is the radius of a primary particle and h is the separation distance between two particles. In this study, the rotational movement of particles and interaction forces between particles and collectors are not taken into consideration. Moreover, the effect of particles on the flow field is also neglected.

Figure II.8 is an illustration of the computational procedures conducted at each simulation step. At the beginning of each simulation step, the initial positions of all particles are known; and they are used to find neighbors for each particle. Two particles are neighbors and can interact with each other when the distance between their centers is less than a cut-off distance, R_c; and in this study, the cut-off distance is assumed to be three times the diameter, D, of a primary particle (R_c = 3 x D = 3 x 190nm = 570 nm). The explanation for choosing 3D as the cut-off distance is presented in Appendix B.5. It would take significant computing time to calculate the distance between each particle and all the remaining particles in the simulation box to find all neighbor pairs (all-pair method). Our code, however, utilizes the cell subdivision algorithm,[157] which significantly reduces the computational time. For example, with a system of 10,544 particles, the cell subdivision method is about 200 times faster than the all-pair one.

Next, a check for aggregation of particles is carried out between neighbors to find all aggregation events at this step. If a separation distance between two particles is less than the primary minimum, those two particles are assumed to coagulate permanently. In this state, the particles remain in their relative positions and do not separate at any time forwards. Other primary or coagulated particles can join them through the same mechanism to form a bigger cluster. By knowing the positions of all the particles, it is possible to obtain the hydrodynamic radius (R_h), the

fractal dimension (D_f), and the asphericity (As) of each aggregate. The calculation of R_h, D_f, and As is elaborated in the next sections. After the aggregation checks, the number of clusters is known. In our numerical framework, a cluster can be a single particle or an aggregate consisting of multiple primary particles. The interaction forces (F_e and F_{vdW}) applied on each particle are computed based on its neighbor list. The force exerted on a cluster due to van der Waals or electrostatic interactions is calculated as the sum of the forces acting on its constituent particles. Similarly, the gravity and buoyancy forces of a cluster are also determined by adding the forces acting on each individual particle. However, the drag and random forces acting on a cluster are computed using Eqn. II.19 and II.20, which require the use of the cluster hydrodynamic radius.

Once all the forces applied on each cluster are computed, the new velocity of each cluster can be found based on Eqn. II.16. In our study, aggregation is considered to be irreversible; therefore, all the particles comprising a cluster and the cluster itself travel at the same velocity. With a known timestep, Δt, and the new velocity of the particles, it is possible to determine the new positions of all the particles; and the new positions are checked to guarantee that no particles are overlapping or inside the solid phase. In case a particle or a cluster hits the wall, it rebounds to its previous position. The periodic boundary condition is also implemented. When a particle or a cluster moves out of the simulation box, it returns to the box from the opposite side. At this point, all the calculations for this simulation step are completed. The new positions of particles at this simulation step become the initial positions for the next simulation step; and all the calculations in the previous step are repeated. This approach allows the position and velocity of each particle to be tracked and investigated at each timestep, making it possible to observe how aggregates form and evolve over time.

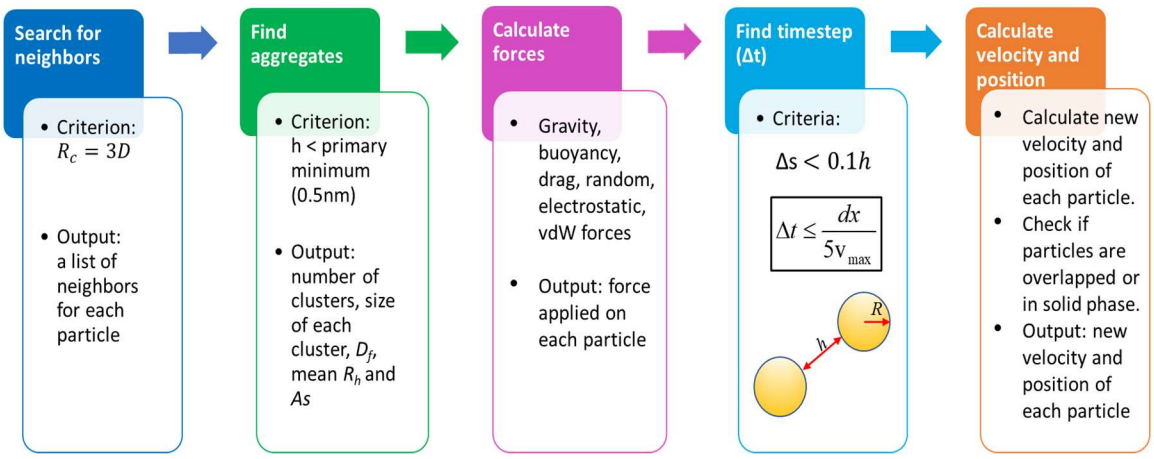


Figure II.8. Calculations are performed for every simulation step in LPT/FB aggregation model. *h* is the distance between two particles; *dx* is the mesh resolution in the x direction; and Δs is the distance that a particle travel at the current step.

The most challenging issue of simulating this multiscale process is selecting an appropriate timestep that could reflect interactions among particles as well as their movements due to convection and diffusion. If the timestep is large, the particles will move and pass through their nearest neighbors without agglomeration; therefore, interactions among particles would be ignored and aggregation would be simulated inaccurately. However, if the timestep for each simulation step is too small, the method will have extreme computational costs. To overcome this challenge, instead of using a fixed timestep, a dynamic timestep is used. The timestep at each simulation step varies based on two constraints, as detailed in Appendix B.1. Firstly, at each simulation step, the minimum distance between the two nearest particles is computed; and the maximum distance that a particle in the nearest pair can travel is limited to be less than one-tenth of this minimum distance. This ensures that particle-particle interactions are accounted for, and no particles can overlap or pass through each other. Secondly, particles are not allowed to move more than one-fifth of the grid resolution (*dx*) of the simulation domain; which ensures that no particles can travel through the solid phase of porous media.[91,115,139] With these two constraints, when the minimum distance between the two nearest particles is large, the timestep is large, and on the order of 10^{-4} or 10^{-5} s.

However, a very small timestep, on the order of 10^{-8} or 10^{-9} s, is used when there are at least two particles that are close to each other (h < D). This model takes a long time to simulate the aggregation, especially the reaction-limited one, because the particles need to collide many times before aggregating or expelling each other. To overcome this limitation, when the distance between two particles is small, all the particles that do not have neighbors are frozen; and calculations related to forces, velocities, and positions are performed only for particles having neighbors or having interactions with other particles. If one of three criteria is satisfied: two particles aggregate; one particle moves out of the interaction zone; or the total freezing time is larger than a user-defined freezing time, the model will unfreeze all frozen particles, and the motion of these particles is simulated with a timestep equal to the freezing time. This method saves computing time because it skips the calculations for particles that do not interact, without impacting accuracy. The user-defined freezing time is selected to make sure that it does not affect the physics of the process; and in this study, it is equal to 10^{-4}s. The selection of user-defined freezing timestep is justified in Appendix B.3.

II.3.3. Fractal dimension

The fractal dimension represents how compactly the single particles are placed within a cluster; and its value is between 1 and 3.[81,158] Note that the denser the cluster, the higher the fractal dimension.[81,158] An aggregate with a fractal dimension close to 1 has a shape as a line of particles, while one with a fractal dimension of about 3 has a compact structure looking like a sphere.[81,159] The fractal dimension of fractal-like clusters can be expressed by the following equation:[84,159–161]

$$n = k_f \left(\frac{R_g}{R}\right)^{D_f} \tag{II.24}$$

where n is the number of primary particles in the cluster; k_f is the scaling prefactor; and R is the radius of primary particles. R_g is the radius of gyration of the cluster, which is the root mean square distance of particles from the center of mass, and is defined as[160,162]

$$R_g = \sqrt{\frac{\sum_{i=1}^{n} r_i^2}{n}} \tag{II.25}$$

where r_i is the distance from the center of the i-th primary particle to the center of mass of the aggregate. In our model, R_g is calculated for all clusters having at least 3 primary particles; and D_f is computed from Eqn. II.24 as shown in Figure II.9.[82]

The fractal dimension is reported to change with the aggregation regime. For instance, the D_f of clusters formed in diffusion-limited aggregation is found to be between 1.7 and 1.8, while D_f in reaction-limited aggregation is observed to be between 1.9 and 2.1.[81,84,159,160]

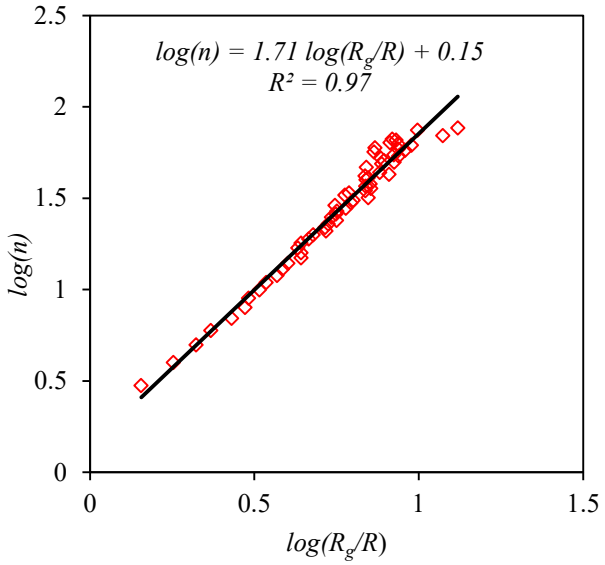


Figure II.9. Fractal dimension of aggregates is defined from the relationship between R_g/R and n as seen in Eqn. II.24. The slope of the line is the fractal dimension, which is equal to 1.7, in this case of aggregation of CeO_2 particles of D = 190nm in a solution of 0.2M KCl and at bulk conditions.

II.3.4. Hydrodynamic radius and asphericity of an aggregate

The hydrodynamic radius of an aggregate is the radius of a hard sphere that diffuses the same as the aggregate;[160–162] and it can be experimentally measured by Dynamic Light Scattering.[148,160–162] The hydrodynamic radius can be computed based on the structure of the aggregate. Hess et al. applied Kirkwood-Riseman theory[163,164] to calculate the translational diffusion coefficient of an aggregate based on its structure (or its radius of gyration). Then, the calculated diffusion coefficient is used to compute the radius of a sphere via the Stokes-Einstein equation. The expression showing the relationship between the radius of gyration and the hydrodynamic radius is given below: [161,162]

$$R_h = \frac{2(D_f - 1)\sqrt{(D_f + 2)}}{D_f^{1.5}} R_g. \tag{II.26}$$

The aggregate morphology is also represented by the asphericity, which quantifies the deformation of an aggregate from a spherical shape; and it is in the range from 0 to 1.[84,152,165] The value of asphericity is 0 for a three-dimensional spherical aggregate, 0.25 for a two-dimensional disc-like aggregate, and 1 for a one-dimensional rod-like aggregate.[165–168]

The asphericity is mathematically expressed as below:[166–168]

$$As = \frac{(R_1^2 - R_2^2)^2 + (R_2^2 - R_3^2)^2 + (R_3^2 - R_1^2)^2}{2R_g^4} \tag{II.27}$$

where R_1^2, R_2^2, R_3^2 are the eigenvalues of the moment of inertia tensors T as follows:

$$T_{lk} = \frac{\sum_{i=1}^{n}(S_{il} - S_l^{CM})(S_{ik} - S_k^{CM})}{n} \tag{II.28}$$

where S_{ik} and S_{il} are the positions of particle i in directions k and l of a Cartesian coordinate system, respectively (l and k are integers, varying from 1 to 3); S_k^{CM} and S_l^{CM} are the positions of the center of mass of an aggregate in Cartesian directions *k* and *l*; n is the number of primary particles in the aggregate.

However, the asphericity does not represent how dense an aggregate is. For example, both aggregates in Figures II.10a and II.10b are bound by the same sphere but they have different packing rates (63% and 3.4%) and different fractal dimensions (3 and 1.2). Interestingly, they both have the same asphericity of 0. Similarly, the two-dimensional aggregates in Figures II.10c and II.9d have the same asphericity of 0.25 but their fractal dimensions are completely different from each other (2 and 1.1). On the contrary, the fractal dimension cannot describe the shape of the aggregate boundary. Therefore, it is important to calculate the fractal dimension and asphericity to characterize the density and the shape of aggregates. Both D_f and As are evaluated herein to provide a full understanding about the morphology of aggregates.

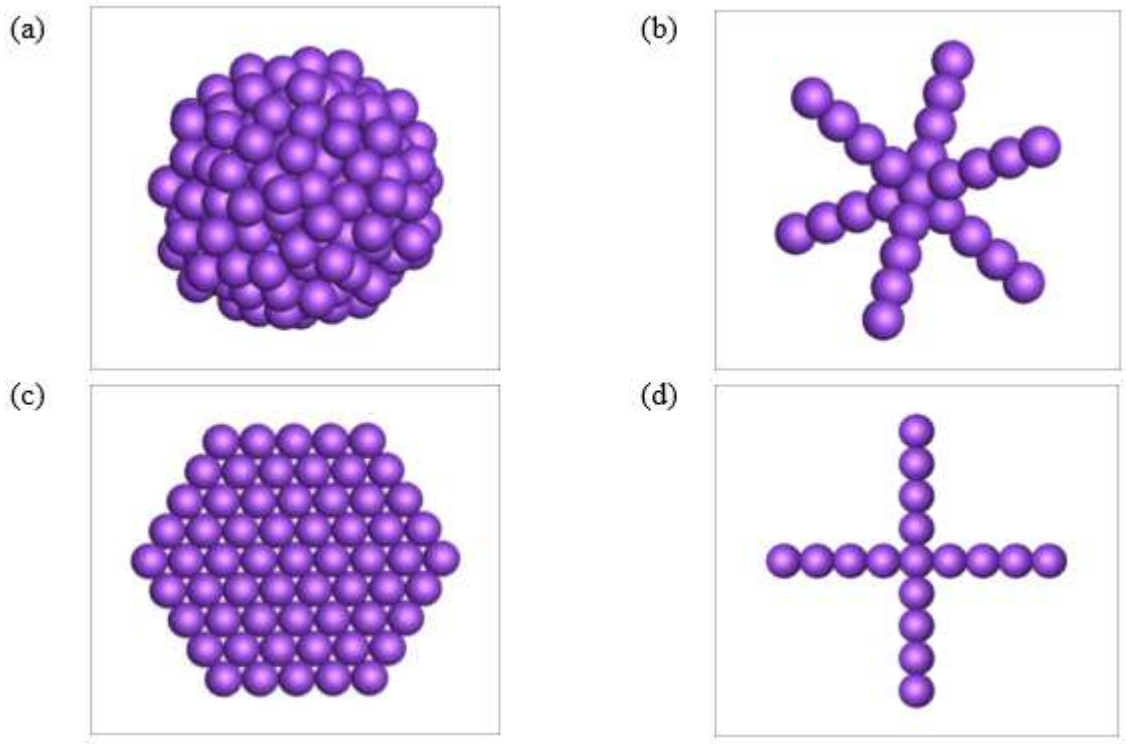


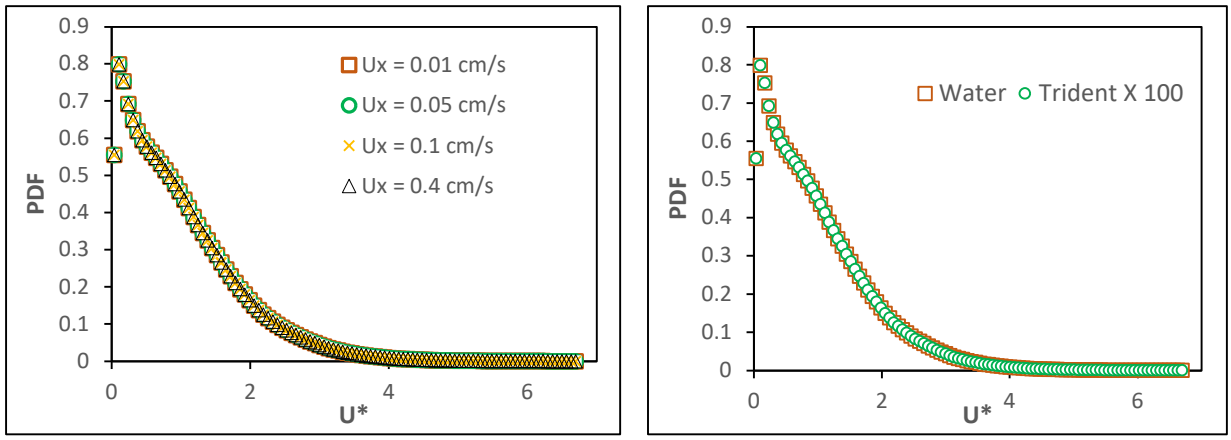
Figure II.10. (a) Particles are distributed in a spherical cluster with D_f= 3 and As = 0, (b) Particles are arranged in an orderly 3D structure with D_f= 1.2 and As = 0, (c) a 2D cluster has a hexagonal shape with D_f = 2 and As = 0.25, (d) a 2D cluster that is inscribed in the same circle as the hexagonal cluster in 3(c); and it has D_f= 1.1 and As = 0.25.

III. RESULTS

III.1. Velocity Magnitude Distribution for Flow in Porous Media

III.1.1. Velocity magnitude distribution for flow in sphere packings and scaffolds*

The distribution of the normalized velocity magnitude of the flow in monodisperse sphere packing is shown in Figure III.1 for different fluid velocities and different types of fluids. It is seen in Figure III.1a that the normalized velocity magnitude (calculated in Eqn. II.9) did not change when the driving force or the fluid velocity varied. Furthermore, as shown in Figure III.1b, the distribution of normalized velocity magnitude of the water flow through mono-sphere packing was identical to that of the Trident X-100 flow through the same porous type. Hence, it is confirmed that the distribution of normalized pore velocity magnitude remained unchanged for Newtonian fluids that flowed through the porous media, as expected for low Reynolds numbers in the Darcy flow regime.



(a) (b)

Figure III.1. (a) The distributions of normalized pore velocity magnitude for water flow in monodisperse sphere packing at different pore velocities in the *x* direction, and (b) the velocity distribution of different fluids with pore velocity in *x* direction of 0.1 cm/s.

* The results presented in this section have been published in Industrial & Engineering Chemistry Research.[175]

An illustration of the pore velocity magnitude in planes that are perpendicular to the *y*-axis and parallel to the flow direction in SC, FCC, monodisperse sphere packing, foamy scaffolds, and the fiber scaffold is displayed in Figure III.2. High velocities were observed in pore throats as shown in Figure III.2a, Figure III.2b, Figure III.2d and Figure III.2e; and a similar finding has been reported in previous studies.[131,132] However, in a pore or a throat, the low velocities were spotted near the solid matrix, while higher velocities were found at the center of the pore and the highest velocities were seen at the pore throats as clearly shown in Figure III.2d and Figure III.2e. These observations are rational explanations for the high value of the PDF at the lowest velocity bin in SC, BCC, and foam scaffolds as seen in Figure III.3b and Figure III.3c because of their very big pores and very small throats. Furthermore, based on observations of the graphs of the monodisperse packing (Figure III.2c) and the fiber scaffold (Figure III.2f), the fluid flowing through flow paths with big pores achieved higher velocities than the fluid traveling through alternative flow paths with small pores. This result makes sense intuitively when one considers flow through parallel pipes, where the fluid transports through the bigger pipes with higher velocity due to less resistance to flow. Therefore, the pore structure and the geometry of the open pore space affected the velocity distribution in porous materials quite significantly.

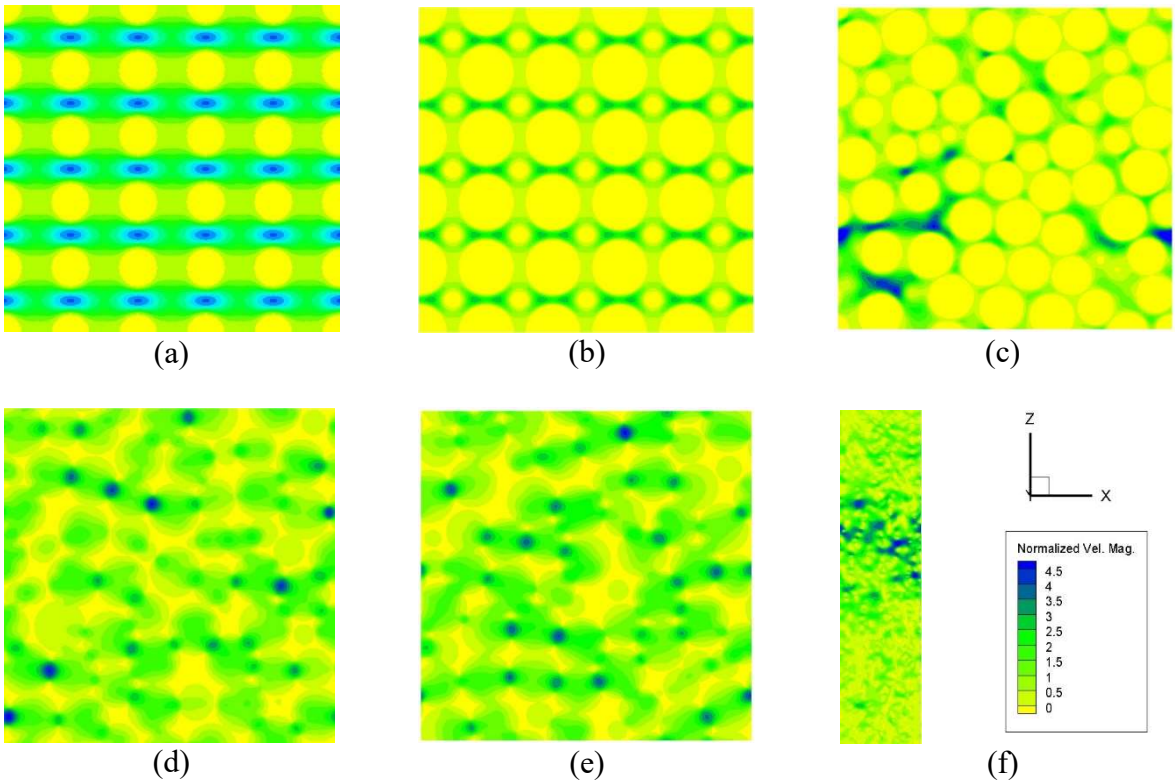


Figure III.2. Details of normalized pore velocity magnitudes in 2D planes perpendicular to the streamwise axis and parallel to the flow direction in (a) SC, (b) FCC, (c) the monodisperse sphere packing, (d) the monodisperse foam scaffold, (e) the bidisperse foam scaffold, and (f) the fiber scaffold. The areas seen in yellow color designate the solid phase, where the velocity magnitude is zero.

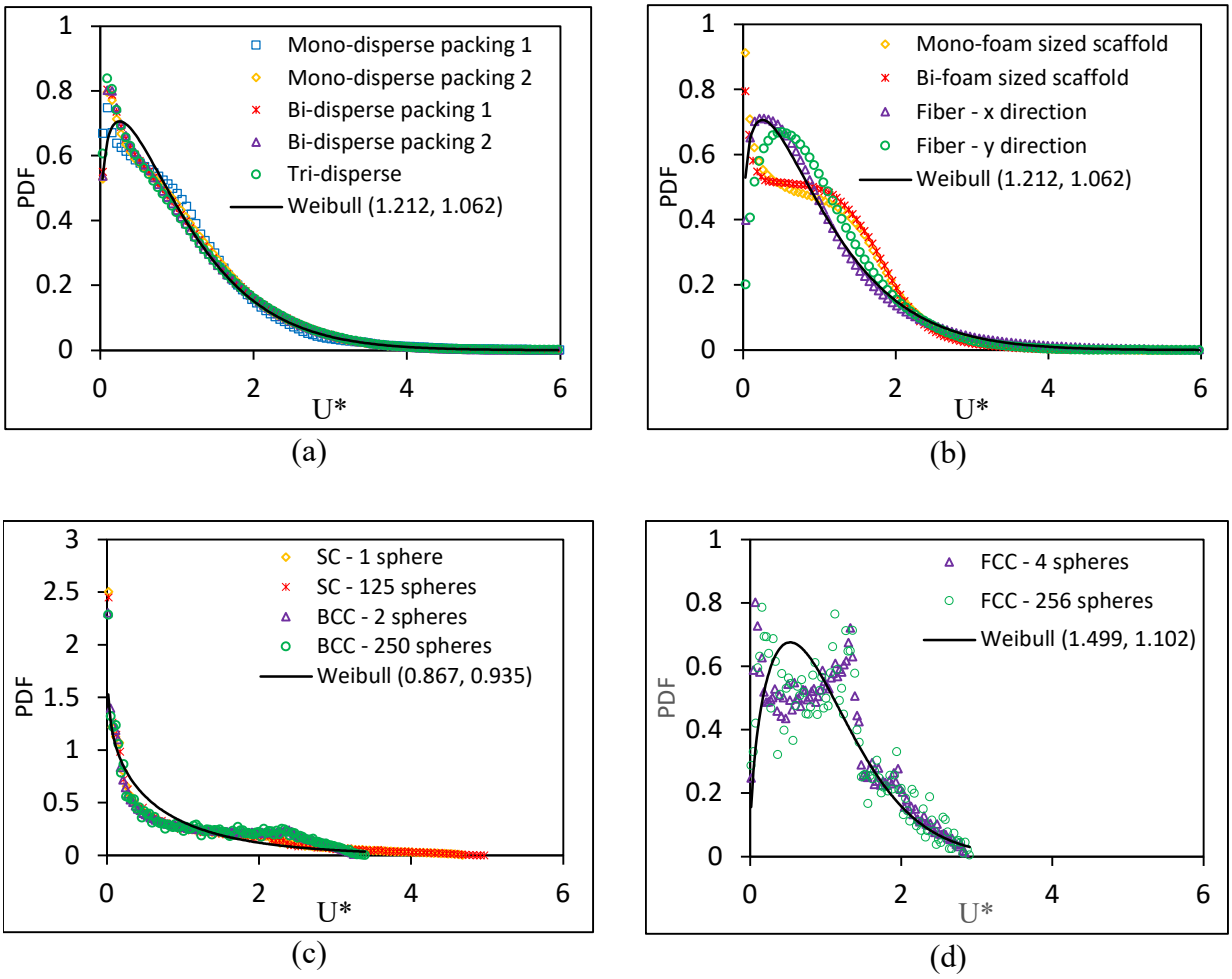


Figure III.3. Graphs of the distributions of the 3D normalized velocity magnitude together with the distribution tested with the null hypothesis – the Weibull distribution for (a) random sphere packings, (b) scaffolds, (c) SC, BCC, and (d) FCC.

Figure III.3 is an illustration of the 3D velocity magnitude distributions in random sphere packings (Figure III.3a), scaffolds (Figure III.3b), SC and BCC (Figure III.3c), and FCC (Figure III.3d). The distributions of velocity magnitude in different random sphere packings including monodisperse, bidisperse and tridisperse were very close to each other. Similarly, the monodisperse foam scaffold and the bidisperse foam scaffold appeared to have similar distributions for the pore velocity magnitude. Moreover, the velocity magnitude distribution of flows through the nonwoven fiber scaffold in two different directions (x and y) showed a minor

discrepancy. In contrast, velocity distributions in sphere packings with the configuration SC, BCC and FCC did not show good agreement with the distributions in randomly generated sphere packings.

Our main objective was to seek a predictable form of distribution that would fit the velocity distribution in the sphere packings and scaffolds within acceptable accuracy. If this occurred, then we would investigate whether it is possible to discover one unique distribution to describe all the data in all the sphere packings and scaffolds within statistical accuracy. First, data of the velocity distribution in such porous media were tested against 65 common distribution forms using the software Easy Fit 5.6 and a Kolmogorov-Smirnov (KS) goodness-of-fit test that is available with this software. The tested null hypothesis was "the PDF of the normalized pore velocity magnitude distribution follows the X probability density function," where X was used to designate each one of the 65 different PDFs available with Easy Fit 5.6. The KS test measured the maximum vertical difference between the cumulative distribution function of the PDF in the null hypothesis and that of the observed data, which is called the KS statistic.[94] The null hypothesis would be rejected if the KS statistic value was larger than the critical value corresponding to a significance level. For example, when the critical value of the KS statistic corresponding to the significance level of 0.2 is 0.1, it means that in 20% of random samples, the maximum allowable deviation between the sample cumulative distribution and the null hypothesis cumulative distribution is 0.1. Therefore, the higher the significance level is, the more likely it is for the null hypothesis to describe the observed data. Moreover, this test also calculated the p-value, which is the probability of explaining the data values in the observations with the assumption that the null hypothesis is correct. A small p-value indicates a low likelihood that the investigated data are explained by

accepting the null hypothesis. In this study, a distribution used in the null hypothesis was accepted to represent the data when the significance level was 0.2, and the p-value was higher than 0.2.[169]

Table III.1. The p-values from the KS tests conducted for velocity distributions in different types of sphere packings and scaffolds including data from ref.[1] against the six best distribution forms. The table also displays the shape and scale factors (α and β) for the Weibull distribution that best fits each porous medium. The p-values of the KS test conducted for the null hypothesis testing whether the Weibull universal form (α = 1.212, β = 1.062) was a good fit are illustrated in the last column. The attained significance level was 0.2 in all cases except for those with p-value marked with a, b, or c where that level was 0.1, 0.01, or 0.00, respectively.

Distribution types	Johnson SB	Beta	Pearson 6	Burr	Log-Pearson 3	Weibull			Weibull universal form
	p-value	p-value	p-value	p-value	p-value	p-value	α	β	p-value
SC-125 spheres	0.11[a]	1.00	0.74	0.62	0.51	0.62	0.833	0.914	0.00[c]
SC-1 sphere	0.12[a]	0.00[b]	0.76	0.64	0.56	0.65	0.836	0.916	0.00[c]
BCC-250 spheres	0.44	1.00	0.52	0.49	0.57	0.49	0.902	0.957	0.01[b]
BCC-2 spheres	0.48	1.00	0.15[a]	0.50	0.58	0.50	0.905	0.959	0.01[b]
FCC-256 spheres	1.00	1.00	0.44	0.76	0.99	0.77	1.499	1.102	0.28
FCC-4 spheres	1.00	0.97	0.32	0.71	0.98	0.69	1.483	1.099	0.24
Monodisperse packing 1	0.99	0.11[a]	0.95	1.00	0.99	1.00	1.204	1.063	1.00
Monodisperse packing 2	0.99	0.67	0.99	0.99	0.99	1.00	1.212	1.063	1.00
Monodisperse -Souzy[3]	1.00	1.00	1.00	1.00	1.00	1.00	1.341	1.091	0.90
Bidisperse 1	0.99	1.00	1.00	0.99	1.00	1.00	1.186	1.059	0.99
Bidisperse 2	0.99	1.00	1.00	1.00	1.00	1.00	1.190	1.060	0.99
Tridisperse	0.97	1.00	1.00	1.00	1.00	1.00	1.164	1.052	0.96
Fiber-x	1.00	0.92	1.00	1.00	1.00	1.00	1.212	1.064	1.00
Fiber-y	1.00	1.00	1.00	1.00	1.00	1.00	1.46	1.105	0.51
Monodisperse foam scaffold	0.92	0.52	0.28	0.72	0.92	0.72	1.26	1.064	0.63
Bidisperse foam scaffold	0.98	0.56	0.41	0.74	0.97	0.73	1.34	1.082	0.48

The details of the distribution forms with the highest significance levels and p-values for the velocity distribution in all porous media tested were presented in Table III.1. Only the six best distribution forms were presented out of the 65 tested. Based on the statistical data, Weibull, Burr, and Log-Pearson 3 were the most appropriate distributions that fit the velocity magnitude PDF in sphere packings and scaffolds, since they all attained a significance level of 0.2 and the average p-value was higher than 0.8. The data from Suzy et al.[3] are also shown in Table III.1; and they follow the same trend as our data.

Among the distributions listed in Table III.1, the Weibull distribution was selected to be further studied, because (a) the average p-value was higher than for other distribution types, and (b) the parameters of the Weibull PDF shown in Table III.1did not vary as much as the parameters of the other distributions. In this respect, it was simpler and more accurate to search for a common form of the Weibull distribution for velocities in all the examined media. Moreover, the Weibull distribution has been found to describe random variables in various physical applications including industrial engineering, biology, materials engineering, medicine, agriculture, and so on.[170] It is also especially useful in modeling environmental data, such as wind velocities[170–172] and wind energy.[172–174] The PDF of the normalized velocity magnitude U* in the Weibull distribution is given as follows[172] :

$$f(U^*) = \frac{\alpha}{\beta}\left(\frac{U^*}{\beta}\right)^{\alpha-1} exp\left(-\left(\frac{U^*}{\beta}\right)^{\alpha}\right);\ U^* \geq 0$$
$$f(U^*) = 0 \qquad ;\ U^* < 0 \tag{III.1}$$

where α is the shape factor characterizing the shape of the distribution (i.e., how the distribution is skewed) and β is the scale factor of the Weibull distribution that characterizes the range of it. It is important to also note that the random variable in a Weibull distribution has to be positive (as is

the case here with the velocity magnitude) and that the mean of the distribution is given as $\beta\ \Gamma(1 + \frac{1}{\alpha})$, with Γ the gamma function. When the two parameters, the shape and scale factors, of the distribution are known, all other PDF characteristics can be found analytically, so one can know the most common value of the pore velocity magnitude (i.e., the mode of the distribution), or the variance, skewness and kurtosis of the distribution.

The next step was to probe whether the shape and scale factors for a single Weibull distribution can be used to fit the velocity distributions for all the sphere packing and scaffold types. The KS goodness of fit test was used to test whether the normalized pore velocity distribution in such porous media can be described by one universal Weibull model. The shape and scale factors of this distribution were expected to vary within the range of values listed in Table III.1. The best Weibull distribution was the one with shape factor α =1.212 and scale factor β = 1.062. The KS goodness of fit test for this distribution was now based on testing the null hypothesis that "the data observed follow a Weibull distribution with α =1.211 and β = 1.062.". This null hypothesis was accepted as a model for the normalized velocity magnitude distribution in random sphere packings and nonwoven fiber scaffolds. It could also describe the distribution of the normalized pore velocity magnitude in the monodisperse foam scaffold and the bidisperse foam scaffold with a p-value of 0.63 and 0.48, respectively. However, it was rejected for the cases of SC and BCC; and it poorly represented the pore velocity distribution in FCC. The details of significance levels and p-values from the KS test for this null hypothesis were summarized in the last column of Table III.1. Therefore, there were two new Weibull distributions proposed for non-random sphere packings. Weibull (α = 0.867, β = 0.935), shown in Figure III.3c was suggested to represent the velocity distributions for SC and BCC with a significance level of 0.2 and p-value of 0.50 and 0.44 respectively. Moreover, Weibull (α = 1.499, β = 1.102) demonstrated in Figure

III.3d was recommended for modeling the velocity distribution in FCC with a significance level of 0.2 and p-value of 0.75.

Figure III.9 is a display of the velocity and pore area distribution in all the examined porous media. The normalized pore area, A^*, was calculated as $A^* = \frac{A}{\bar{A}}$,where A is the area of the pore calculated in 2D planes using the watershed method and $\bar{A}$ is the average area of all the pores in the geometry. It can be observed that the pore size distribution in ideal, ordered sphere packings (SC, BCC, and FCC) appeared to be discrete (intermittent). On the contrary, the random sphere packings and the fiber scaffolds that followed the same distribution had rather continuous pore area distributions. Moreover, in these porous types, the pore area distribution and velocity distribution both demonstrated a positive skewness and had the same trend. Hence, one can conclude that the pore size in the pore-network configuration directly impacted the velocity distribution. For the case of foam scaffolds, it appeared that the pore area distributions were semi-continuous; therefore, their velocity distributions were statistically represented by the common Weibull proposed for random sphere packings and fiber scaffolds. In brief, it was hypothesized that when the pore sizes were distributed in a more random manner and not dominated by a few length scales, the fluid flowed in different directions, through pores and pore throats with different sizes, so that the velocity distribution could be described by one universal PDF.

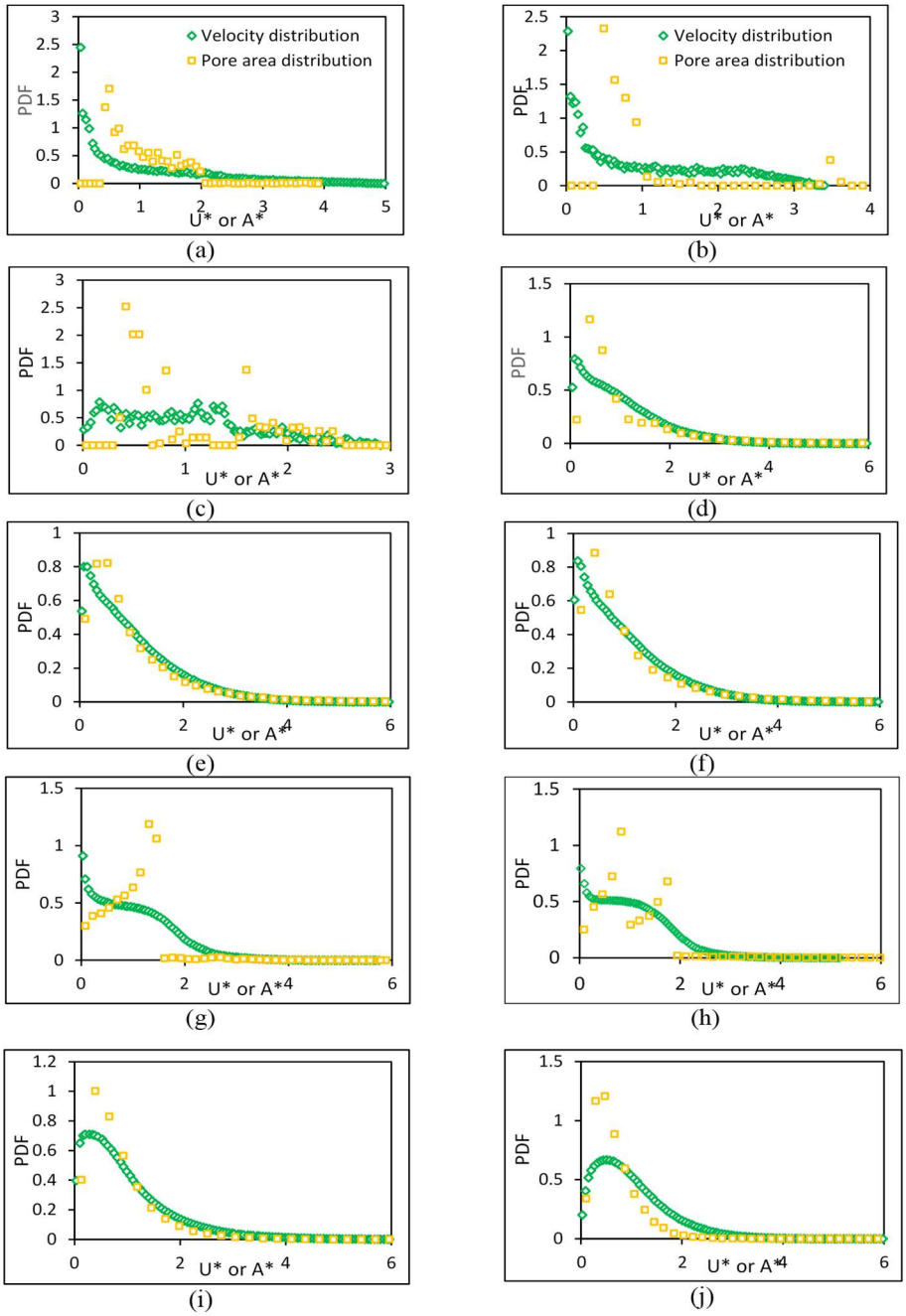


Figure III.4. Distributions of normalized velocity magnitude and normalized pore area in all types of porous materials including (a) SC, (b), BCC, (c) FCC, (d) monodisperse sphere packing, (e) bidisperse sphere packing, (f) tridisperse sphere packing, (g) monodisperse foam scaffold, (h) bidisperse foam scaffold, (i) fiber scaffold with flow in *x* direction and (j) fiber scaffold with the flow in the *y* direction.

III.1.2. Relationship between pore fluid velocity distribution and pore size distribution[†]

Since velocity distributions in sphere packings with random configurations and scaffolds, which have continuous pore-size distribution, can be predicted by a single Weibull model, we aimed to examine if there is any single distribution model that could represent the velocity distributions for all real porous media. Hence, we continued to compute the distributions of the velocity magnitude in different 12 porous media with porosity varying from 13.5% to 85%, including five samples of sandstones (Bentheimer,[118] Berea, Doddington,[119] S1[120] and S2[120]), three types of sphere packings (monodisperse, bidisperse, and tridisperse),[175] a carbonate sample (C1),[120] a synthetic silica sample (A1),[120] and an anisotropic fiber scaffold[114] that was investigated using flow in two different flow directions. However, the velocity magnitude distributions in such porous media with a wide range of porosity behaved too differently that it failed to find a single distribution equation that could fit the velocity distributions in all the examined porous media. The pore-networks of such porous media were studied to investigate their effects on the velocity profiles. The pore-network was extracted by the MB algorithm which could calculate the pore-size as well as its distribution.

The PDF and the cumulative distribution function (CDF) of both velocity magnitude and pore volume distribution in Berea sandstone, carbonate C1, synthetic silica A1, randomly packed spheres of three different sizes (tridisperse sphere packing), and fiber scaffold with the flow in the x direction are illustrated in Figure III.5. It is shown that regardless of the porous medium types, the longer the tail of the velocity distribution, the longer the tail of the pore volume distribution. In low porosity media, such as Berea or Bentheimer, the range of pore size is large with the maximum normalized pore volume of 40 and 14 respectively. In contrast, for media with higher

[†] The results presented in this section have been published in *AIChE Journal*.[188]

porosity including synthetic silica, sphere-packings, and fiber scaffolds, the pore size and the velocity range are relatively smaller with the maximum value equal to around 7.

The two-sample KS goodness of fit test[121–124] was used to determine whether the normalized pore volume PDF and the normalized velocity magnitude PDF in a porous medium follow the same PDF model. The null hypothesis that was tested is "The PDF that the two variables (i.e., the normalized pore size and the normalized velocity magnitude) follow is the same". The null hypothesis was accepted at a certain significance level when the KS statistic was less than a critical value corresponding to that significance level. In this test, the values of the KS statistic were calculated as the maximum difference between the cumulative distribution functions of the two sets of data. This is based on the definition of the KS statistic. The critical value is dependent on the significance level and the sample size of each data set, and is given as $d_a(m,n) = \sqrt{-\frac{1}{2}\ln\left(\frac{a}{2}\right)\left(\frac{m+n}{m.n}\right)}$ where a is the significance level, m and n are the sizes of two data sets.[122,176] The null hypothesis is accepted when the KS statistic is smaller than the critical value and it is rejected when the critical value is larger than the KS statistic. Note that the higher the significance level, the smaller the critical value. In the other words, the acceptance of the null hypothesis at higher significance level becomes a stricter criterion.[124,177,178] Several studies have utilized a significance level of 0.2 to test such a null hypothesis.[6,179–181] More importantly, both charts of PDFs and CDFs illustrate that the normalized pore volume distribution and the normalized velocity magnitude distribution of a porous medium are comparable. Table II.2 also displays the two-sample KS statistic for comparing these two distributions in all the porous media examined. The two-sample KS statistic for all cases is much smaller than the critical value $d_\propto(m,n) = 0.152$ for the case of significance level equal to 0.2 and the number of bins equal to100 for both distributions. Therefore, it was concluded that the pore velocity magnitude and pore

volume PDFs were statistically similar. This finding is aligned with results from a previous computational study that found a positive correlation between the "local permeability" and the average distance from the wall in pore throats.[182] The local permeability was defined as the permeability through an individual pore throat. The average distance from the wall was calculated as the average distance of the computational mesh points within the pore space of that throat and the nearest mesh point on the solid matrix. The local permeability was increasing with the average distance from the wall, indicating that the pore size affects the permeability (and thus velocity) of the fluid. In addition, the results in the present study are supported by prior reports on the relation between PDFs of the streamwise pore velocity and pore size (i.e., the width of the pores normalized by the computational grid space) in stochastically generated isotropic porous media.[4] The velocity PDF was found to follow an exponential model and the pore size followed a stretched exponential model, while the parameters of the PDF models depended on the porosity. Hence, we can conclude that the pore structure of a porous medium determines the pore velocity distribution of the flow. It is also evident that the velocity distribution in a porous medium can be tuned by adjusting its geometry. In our previous work, for porous media generated with ideally arranged spheres (i.e., body-centered cubic, face centered cubic and simple cubic arrangements) the pore size distribution and velocity distribution were not alike.[175] In those cases the pore volume distribution was not continuous, but was either discrete or semi-continuous. For arranged spheres, the number of pores was small, so that the PDF of the normalized pore volume was discrete. The same was true for scaffolds that were not fibrous but foamy. Therefore, when the porous media present a continuous distribution of pore volume, the velocity distribution can be estimated accurately. In terms of predicting the velocity PDF, it is possible when one can obtain the pore volume distribution experimentally. In that case, the average fluid velocity magnitude in the pores can be found by

dividing the superficial velocity (Darcy velocity) of the fluid by the medium porosity, and then using the pore volume distribution. Given the availability of 3D printers and the capabilities to print a porous medium with exact 3D geometry, one can manufacture porous media with prescribed pore volume distributions to achieve desired velocity distributions. This ability can be valuable in several applications, including the design of porous scaffolds optimized for tissue engineering.

(a)

(b)

(c)

(d)

(e)

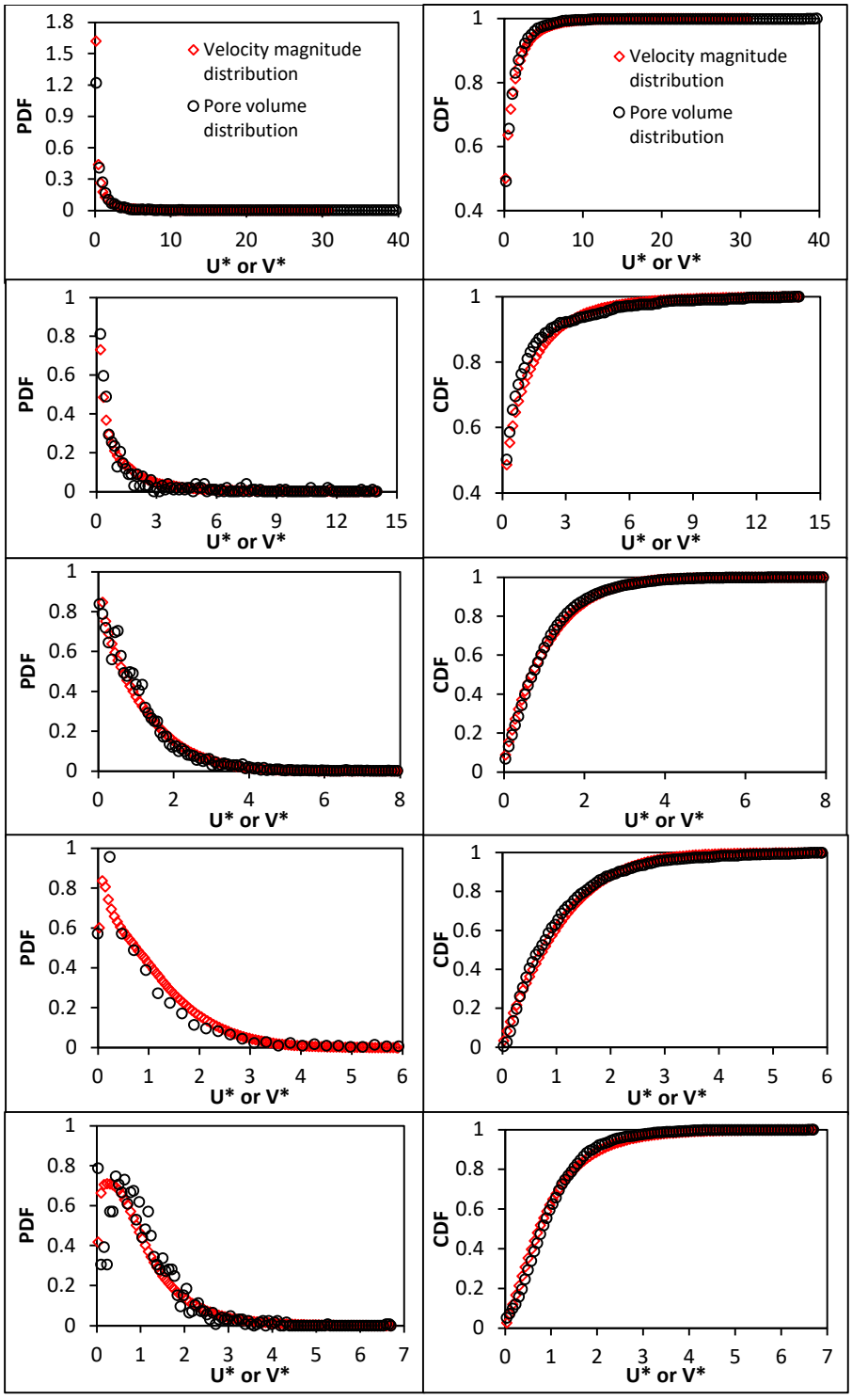


Figure III.5. The probability density function (PDF) and the cumulative distribution function (CDF) for normalized velocity magnitude and normalized pore volume in various porous media: (a) Berea sandstone, (b) carbonate C1, (c) synthetic silica A1, (d) tridisperse sphere packing, (e) fiber-x.

III.2. Hydrodynamic dispersivity based on Lagrangian Peclet number‡

III.2.1. Lagrangian time scale and Velocity Autocorrelation Function

Figure III.6 is a presentation of the VACF of the streamwise velocity in different cases, when water at room temperature flowed through a porous bed packed with an infinite array of spheres arranged in the FCC geometry. The VACF was calculated based on the initial velocity at the beginning of the LPT run ($t_o = 0$), which started once the flow field had reached a steady state. Figure III.6 consists of four graphs, Figures III.6a – d, that represent the VACF of four different types of diffusion NPs with Schmidt numbers of 100, 1000, 7080, and 10,000, respectively. For each value of *Sc*, the velocity autocorrelation functions for various values of average pore velocity, ranging from 50 to 4000 μm/s, are illustrated. Similarly, Figure III.7 is a demonstration of the results for the geometry of randomly packed spheres at the same simulation conditions as Figure III.6. In Figure III.8, the effect of molecular diffusion on the Lagrangian timescale is highlighted. In other words, the dependence of the VACF on Sc, for both the FCC (Figure III.8a) and RPS geometries (Figure III.8b), at the same average pore velocity of 1000 μm/s, is highlighted.

As seen in Figures III.6-8, the velocity autocorrelation coefficients started from unity and dropped to zero in different patterns; and the VACF dropped depending on the Schmidt number, average velocity, and geometry. Therefore, the Lagrangian timescale also changed with these parameters because it was calculated as the area formed by the velocity correlation and the two coordinate axes x and y (see Eqn. II.12 and II.13). Figures III.6 and III.7 demonstrate that the Lagrangian timescale decreased when the velocity increased. This means that particles in high pore velocity cases tend to drop off the flow lines quicker at a constant molecular diffusion coefficient. At the same time after the NP release, the NPs in high pore velocity simulations traveled farther

‡ The results presented in this section have been published in *Fluids*.[65]

in the streamwise direction and had the opportunity to experience a longer tortuous path than NPs in lower pore velocity cases. Moreover, from Figure III.8, it is firmly seen that the higher the Schmidt number, the larger the Lagrangian timescale. This observation can be explained by considering that, when the Schmidt number was high, the random movement because of molecular diffusion was small relative to the movement due to convection. Hence, it took a longer time for the NPs to completely stop following the flow streamlines and for the velocity autocorrelation coefficient to drop to zero. In addition, when the same type of fluid and NPs flowed through the porous media with the same average velocity, the characteristic time scale in the case of the FCC-packed bed was much larger than that in the RPS bed. The reason for this is that the FCC configuration was less tortuous than the RPS configuration. When the particles traveled in the porous media, not only random jumps of particles by diffusion but also their movement due to interactions with the spheres in the packed bed moved them away from their streamline trajectories. Hence, the particles, moving in more tortuous paths, interacted with the wall more often. This could explain why they quickly decorrelated with their initial velocity.

There are two important messages about the Lagrangian scale that should be highlighted. First, Figures III.6 and III.7 show that with the same geometry, the Lagrangian timescale changed with molecular diffusivity (or Schmidt number) and flow velocity. Hence, the relevant length scale also varied with Schmidt number and flow velocity. In contrast, for the same geometry, the Eulerian length scale was unchanged, because it only related to the geometrical configuration of the porous medium. Second, by comparing the change of Lagrangian timescale in Figures III.6 and III.7 with that in Figure III.8, it can be seen that the effects of the Schmidt number (molecular diffusion) were more prominent than the effects of flow velocity and geometry.

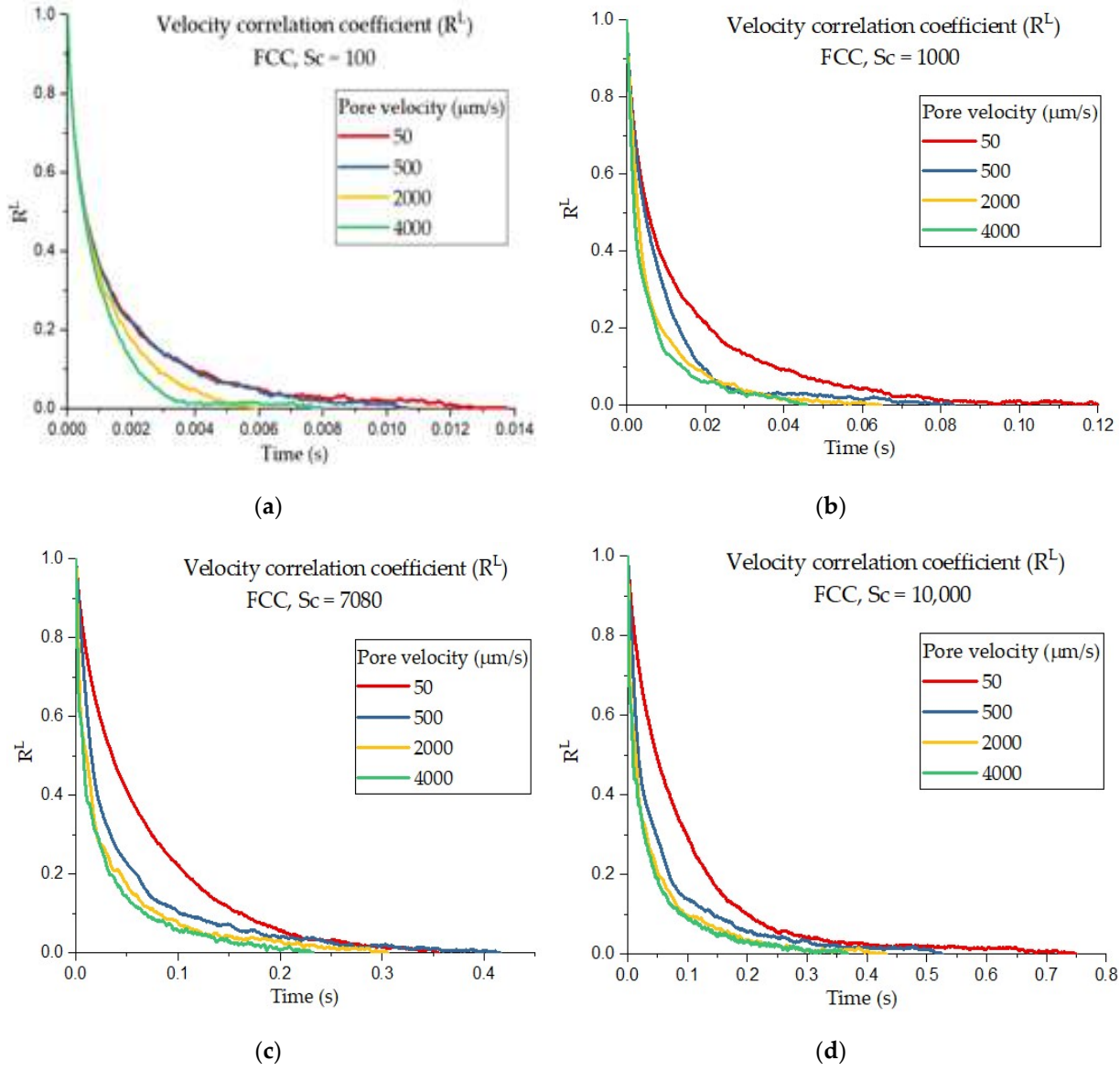


Figure III.6. The velocity correlation coefficient for the packed bed with an FCC geometry with time for (**a**) Schmidt number (Sc) = 100, (**b**) Sc = 1000, (**c**) Sc = 7080, and (**d**) Sc = 10,000. Each graph contains a velocity autocorrelation coefficient for different average pore velocities.

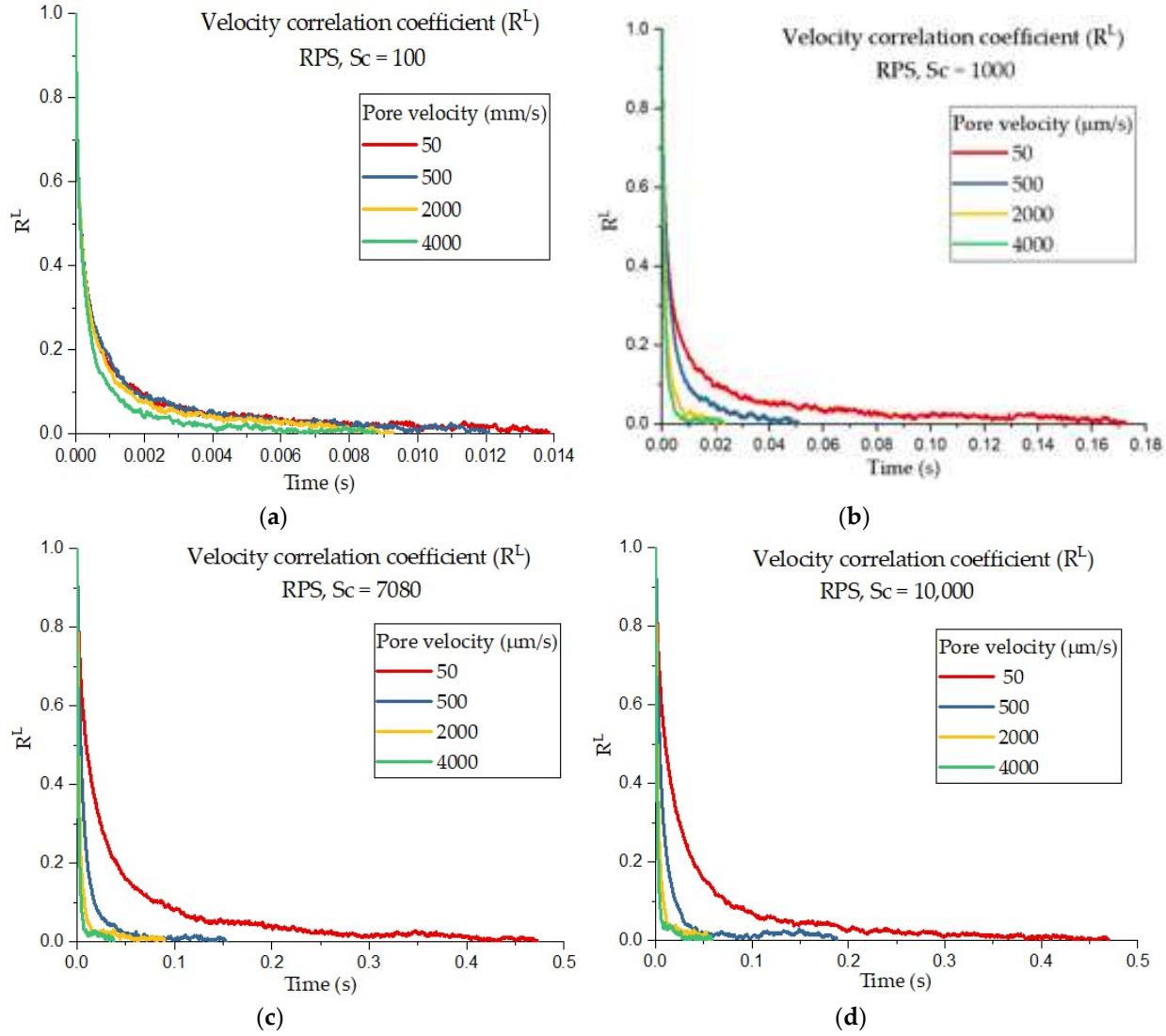
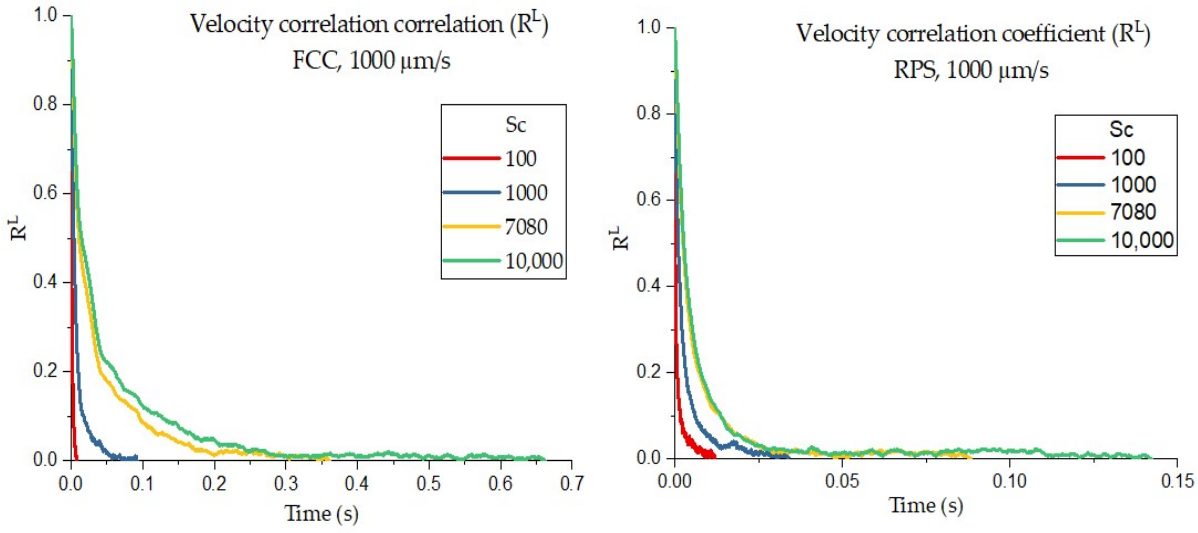


Figure III.7. The velocity correlation coefficients for the packed bed with an RPS geometry with time for (a) Sc = 100, (b) Sc = 1000, (c) Sc = 7080, and (d) Sc = 10,000. Each graph contains velocity autocorrelation coefficients for different average pore velocities.



(**a**) (**b**)

Figure III.8. The effect of the Schmidt number on the velocity correlation coefficient, as well as Lagrangian timescales for both cases including the FCC (a) and RPS (b) configurations at the same average pore velocity of 1000 µm/s.

III.2.2. Hydrodynamic dispersivity

All the data from numerical experiments related to the hydrodynamic dispersion coefficient and Lagrangian timescale for the flow of NPs through FCC- and RPS-packed beds are summarized in Appendix A.2. There were, in total, thirty-six experiments carried out for each porous bed configuration. Four types of NPs with *Sc* = 100, 1000, 7080, and 10000 were released in the flow field with an average pore velocity of 0, 50, 100, 200, 500, 1000, 2000, 3000, and 4000 µm/s. The value of the dispersion coefficient in the static flow field (u = 0) was used as the effective diffusivity D'_m to estimate the ratio of dispersion over diffusion (D_L/D'_m). In addition, the effective Peclet number was obtained from the Eulerian length scale (diameter of the packed spheres, see Equation (4)) or the Lagrangian length scale ($l^L = u\tau^L$), as follows:

$$Pe'^L_m = \frac{ul^L}{D'_m} = \frac{u^2\tau^L}{D'_m}. \quad \text{(III.2)}$$

Figure III.9 is a plot of the ratio of the hydrodynamic dispersion coefficient over the effective molecular diffusion coefficient for particles in the FCC-packed bed as a function of the effective Peclet number. Figures III.9a, III.9b displays the dependence of the coefficient ratio on the effective Eulerian Peclet number and the effective Lagrangian Peclet number, respectively. The examined ratio is linearly correlated with the effective Lagrangian Peclet number. The same analysis was done for the randomly-packed bed; the results are reported in Figure III.10.

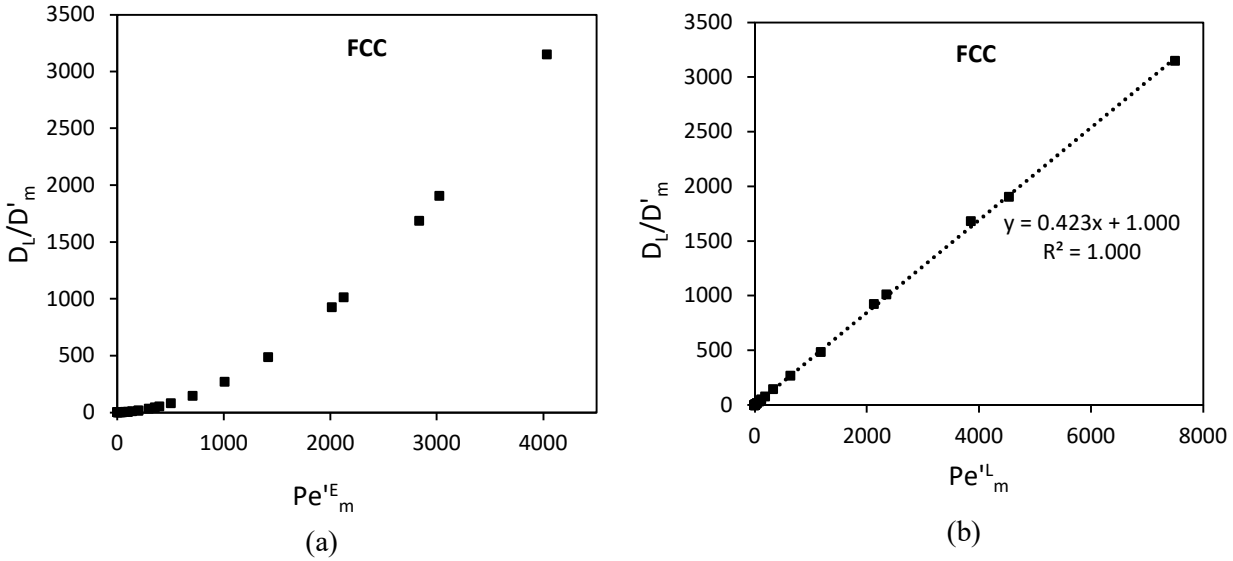
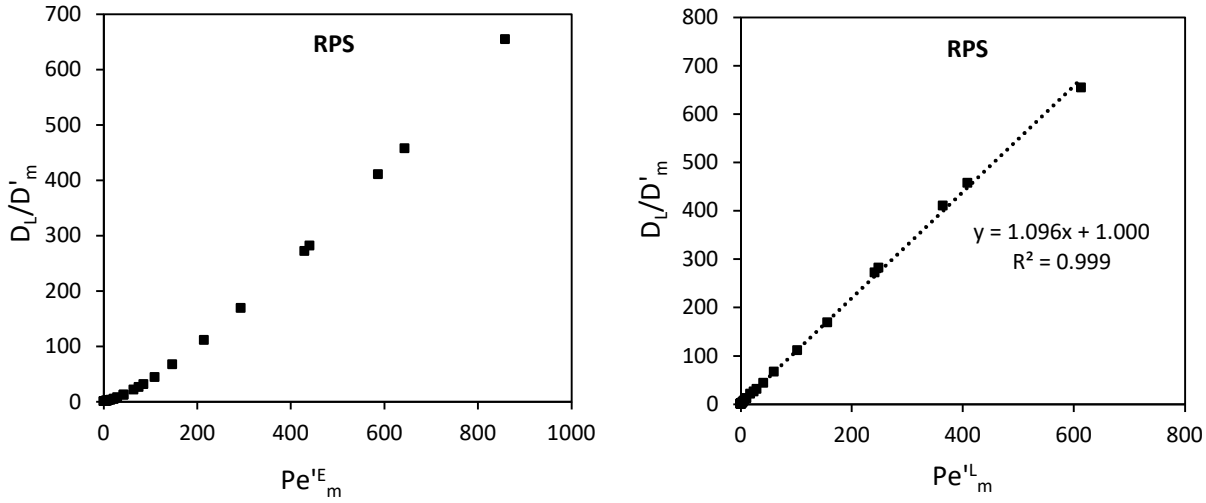


Figure III.9. The ratio of the hydrodynamic dispersion coefficient over the effective molecular diffusion coefficient in an FCC as a function of (a) the effective Eulerian Peclet number based on sphere diameter and (**b**) the effective Peclet number determined from the Lagrangian length scale.[65]



(a) (b)

Figure III.10. The ratio of the hydrodynamic dispersion coefficient over the effective molecular diffusion coefficient in an RPS as a function of (a) the effective Eulerian Peclet number based on sphere diameter and (b) the effective Peclet number determined from the Lagrangian length scale.[65]

By examining Figure III.9 and Figure III.10, it is seen that the ratio of the dispersion coefficient and the diffusion coefficient is a function of Peclet number. Figure III.9a and Figure III.10a indicate that the ratio does not linearly depend on the Eulerian Peclet number $Pe_m'^E$. As the relationship between the dispersion coefficient and Eulerian Peclet number is not clear, to correlate the dispersion and diffusion ratio with the Eulerian Peclet number, we suggested two correlation schemes (1 and 2) that give a minimum value of the mean relative error for this case. In contrast, only the linear equation in correlation scheme 3 was found to be suitable to correlate the dispersion and diffusion ratio with the effective Lagrangian Peclet number as displayed in Figure III.9b and Figure III.10b. The three schemes are well-presented in Table III.2 for FCC and Table III.3 for RPS.

Table III.2. Three correlation schemes for hydrodynamic dispersion of particle transport in an FCC-packed bed.

Correlation Scheme	Correlation Equation	Mean Relative Error
1	$Pe_m'^E < 700 \quad \frac{D_L}{D_m'} = 0.000343(Pe_m'^E)^2 + 1$ $Pe_m'^E > 700 \quad \frac{D_L}{D_m'} = 0.000168\,(Pe_m'^E)^2 + 0.112Pe_m'^E + 1$	6.3%
2	$\frac{D_L}{D_m'} = 1 + 0.00126(Pe_m'^E)^{1.774}$	3.3%
3	$\frac{D_L}{D_m'} = 1 + 0.423Pe_m'^L$	3.3%

Table III.3. Three correlation schemes for hydrodynamic dispersion of particles transport in RPS-packed bed.

Correlation Scheme	Correlation Equation	Mean Relative Error
1	$Pe_m'^E < 500 \quad \frac{D_L}{D_m'} = 0.00853(Pe_m'^E)^2 + 1$ $Pe_m'^E > 500 \quad \frac{D_L}{D_m'} = 0.000365\,(Pe_m'^E)^2 + 0.462Pe_m'^E + 1$	14.6%
2	$\frac{D_L}{D_m'} = 1 + 0.114(Pe_m'^E)^{1.283}$	15.5%
3	$\frac{D_L}{D_m'} = 1 + 1.096Pe_m'^L$	3.1%

Among these three correlation schemes, the third correlation with the effective Lagrangian Peclet number appeared to be superior for three reasons. It had a higher accuracy in comparison with the first and second schemes, based on an effective Eulerian Peclet number, as seen by the smaller mean relative error of Scheme 3, especially for the case of RPS. Moreover, while there was uncertainty in selecting the form of the correlation equation with effective Eulerian *Pe*, the

form of the equation with effective Lagrangian *Pe* was uniform no matter what mode of particle transport was dominant (molecular diffusion or convection). There were at least two unknown parameters in the correlation equation with Eulerian *Pe*, and it was difficult to determine to which properties they related. On the contrary, the equation of the effective Lagrangian *Pe* contained only one unknown coefficient, *A*, as given by:

$$\frac{D_L}{D'_m} = 1 + A\, Pe'^{L}_{m} \tag{III.3}$$

or

$$D_L = D'_m + AU_p l^L = D'_m + A\,\frac{l^{L\,2}}{\tau^L}. \tag{III.4}$$

Though this is a simple equation, it still can express the nature of hydrodynamic dispersion. According to this equation, the coefficient D_L is the sum of two terms. The first term is the effective molecular diffusion coefficient D'_m, and the second term $A\, l^{L\,2}/\tau^L$ is proportional to the characteristic length scale squared over the characteristic timescale. More importantly, with this kind of form, the second term represents the coefficient of mechanical dispersion. Therefore, this correlation equation matches the theory that hydrodynamic dispersion is a combination of molecular diffusion and convective transport. This confirmed that the Lagrangian scale is a proper approach to represent the theory of hydrodynamic dispersion. A large number of numerical experiments were performed to confirmed that his correlation type held for other porous media such as SC (A = 1.169), BCC (A = 0.923), bidisperse sphere packing (A = 0.985), tridisperse sphere packing (A = 1.019), fiber scaffold (A = 0.789), and foam scaffold (A = 0.572). The charts showing the relationship between the ratio of longitudinal dispersivity over the effective molecular diffusivity and the effective Lagrangian Pe of such porous media were presented in Appendix A.3. In this equation, only the parameter *A* changes with various geometry structures; therefore, it is reasonable to argue that *A* represents the properties of porous media.

III.3. Aggregation of nanoparticles

III.3.1. Validation results against aggregation of NPs in bulk

Figures III.11a and III.11b illustrate the Derjaguin-Landau-Verwey-Overbeek (DLVO) forces ($F_{vdW} + F_e$) and the net DLVO energy between two particles as a function of the separation distance between them; and Figure III.12 is a display of changes in the mean hydrodynamic radius of aggregates with time, obtained by both experiments and simulations. In Figure III.11a, the attraction force was dominant over the repulsion force; and there was no energy barrier for the aggregation of particles in KCl solutions of 0.1M, 0.15M, and 0.2M as shown in Figure III.11b. Thus, aggregation of CeO_2 particles in such KCl solutions took place in the diffusion-limited regime. As a result, the aggregation of CeO_2 particles was strongly promoted as per Figure III.12; and the mean hydrodynamic radius curves of particles over time in these electrolyte solutions were very similar. In 0.02M KCl solution, the attraction force was slightly larger than the repulsion force when the separation distance was more than 10 nm as seen in Figure III.11a. However, when two particles came closer to each other, the electrostatic force was dominant over the van der Waals force. Therefore, as seen in Figure III.11b, there was an energy barrier for two particles to agglomerate; and the aggregation of CeO_2 particles in 0.02M KCl was in the reaction-limited regime. Consequently, the aggregation of CeO_2 particles still occurred in this case but the rate was not so fast as that of diffusion-limited aggregation. It is seen in Figure III.11b that the energy barrier increased when the electrolyte concentration decreased. The electrostatic force of CeO_2 particles in 0.001M KCl was much higher than the van der Waals force; and the energy barrier was too high for the two particles to attach. Consequently, almost no aggregates were formed in this case, as displayed in Figure III.12. It is important to note that data related to the mean

hydrodynamic radius of aggregates, obtained by our simulation, agreed well with the ones from experimental results in all investigated regimes.

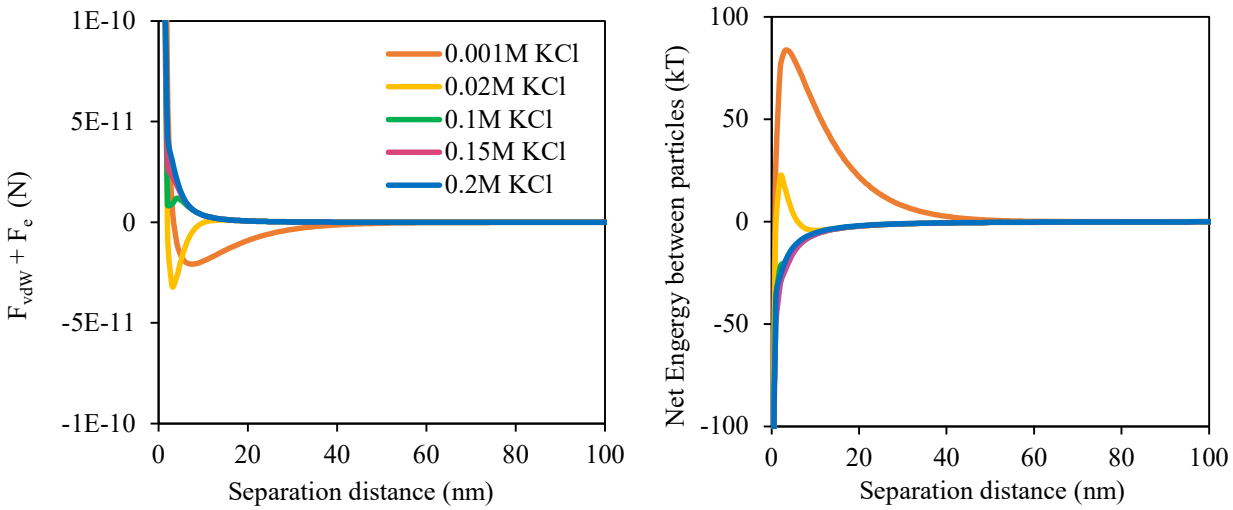


Figure III.11. Interaction forces (a) and the net interaction energy (b) between two particles in aqueous suspension under different KCl concentrations.

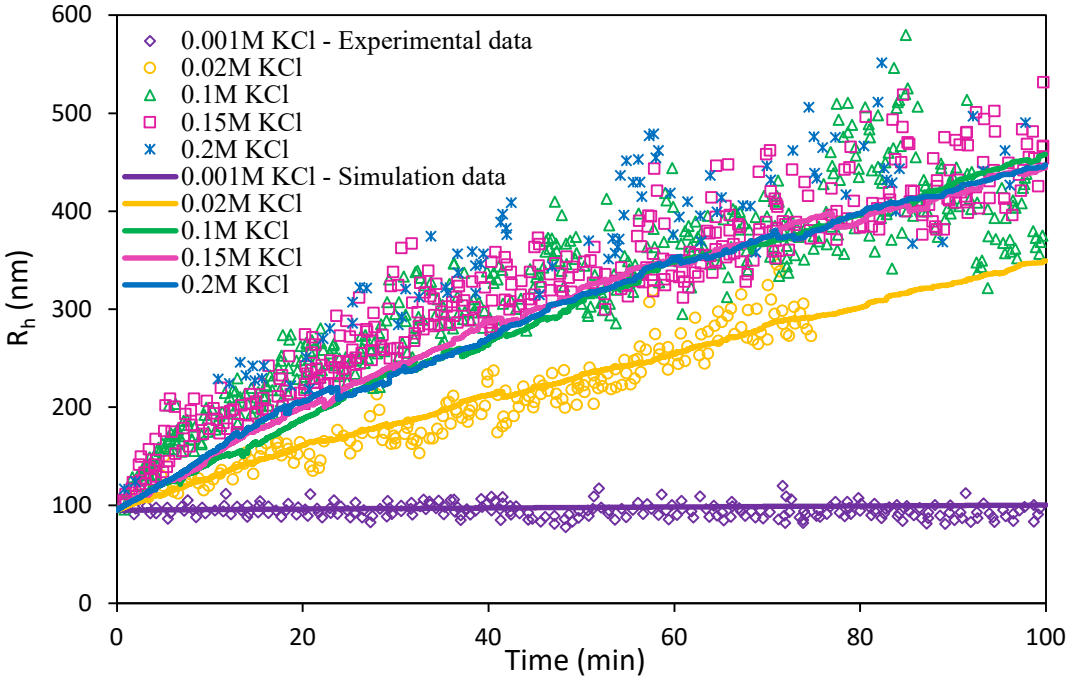


Figure III.12. The hydrodynamic radius of aggregates measured by experiments[148] and simulations during the aggregation process of CeO_2 nanoparticles in different KCl concentrations.

The fractal dimensions calculated by our model during the aggregation process are displayed in Figure III.13. In the diffusion-controlled aggregation (0.1M, 0.15M, and 0.2M KCl), the fractal dimension was about 1.7, while it was around 1.88 in the case of reaction-controlled aggregation (0.02M KCl). The fractal dimension of aggregates has been commonly reported in the range of 1.7 to 1.8 for diffusion-limited aggregation and 1.9 to 2.1 for reaction-limited aggregation.[84] Hence, the fractal dimensions predicted by our model were very close to the results from other groups who have conducted laboratory experiments.

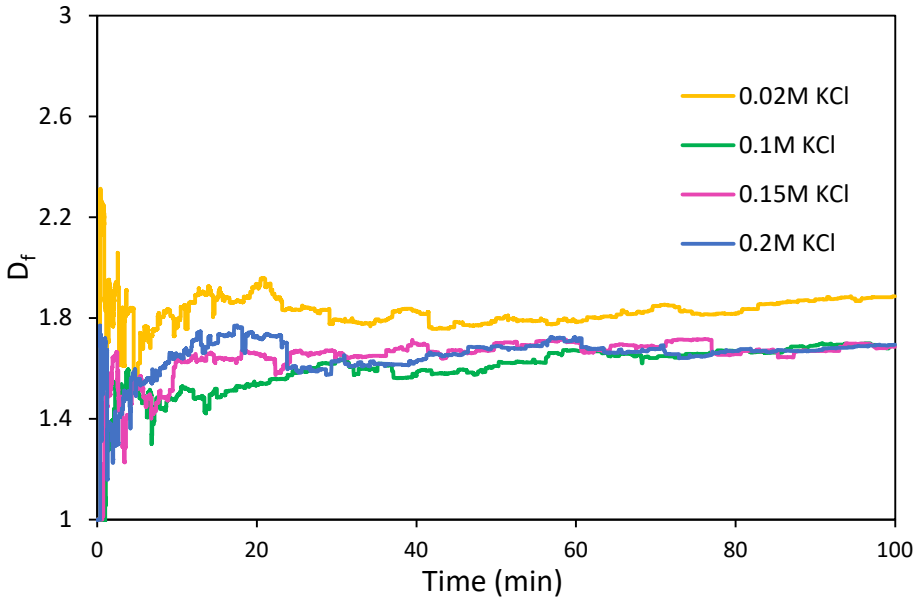


Figure III.13. Fractal dimensions of aggregates in reaction-limited aggregation (0.02M KCl) and diffusion-limited aggregation (0.1M KCl, 0.15M KCl, and 0.2M KCl) were calculated by the simulation.

III.3.2. Aggregation in porous media

III.3.2.a. Effects of the ionic strength

Simulations of CeO_2 particles moving and aggregating in sphere packings, at the pore velocity 500 μm/s, in KCl solutions with different concentrations, including 0.001M, 002M, and 0.2M showed that the influence of the ionic strength on the aggregation of nanoparticles was

significant. Figure III.14a is a display of the mean hydrodynamic radius of aggregates as a function of dimensionless time. Time in pore volume units is defined as the ratio of the elapsed time over the average residence time of the fluid in the simulation box, which was calculated by dividing the length of the simulation box by the mean pore velocity in the streamwise direction.[76] Similar to what was observed in the bulk (see section 4.1), the increase in the electrolyte concentration led to rapid aggregation kinetics. However, when the salt concentration was higher than the critical coagulation concentration (CCC), meaning that the aggregation was in the diffusion-limited regime, the electrolyte concentration did not affect the aggregation rate, as seen in Figure III.12. Figure III.14b represents the ratio of the number of single particles (N_1) and the number of clusters (NC_{total}) as a function of time. When the electrolyte concentration was equal to 0.001M, almost no aggregates were formed; and the ratio N_1/NC_{total} was constant with time. The fraction of single particles over the total number of clusters dropped significantly when the ionic strength or aggregation kinetics increased.

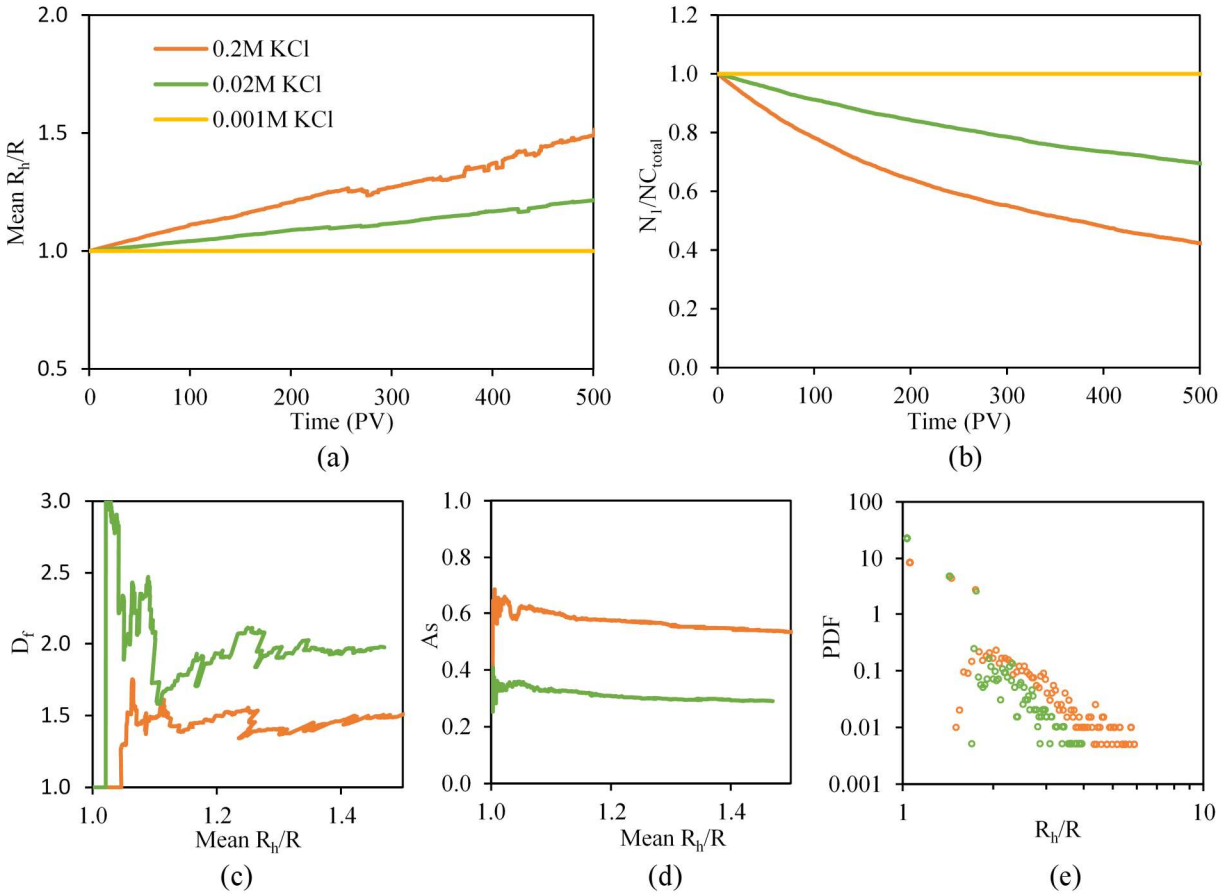


Figure III.14. Effects of potassium chloride concentration on (a) the aggregation kinetics, (b) the ratio between the number of single particles over the total number of clusters, (c) the fractal dimension, (d) the asphericity, and (e) the probability density function of cluster size at t = 500 PV. The investigated electrolyte concentrations included 0.001M, 0.02M, and 0.2M KCl.

Charts in Figures III.14c and III.14d show the fractal dimension and asphericity of aggregates as functions of the ratio of the mean particle hydrodynamic radius over the radius of a single particle; and they provide a strong indication that the ionic strength had a significantly strong impact on the structure of aggregates. The fractal dimension of aggregates produced in the diffusion-limited aggregation was much smaller than that in the reaction-limited regime; and the opposite trend was observed for the asphericity. It is revealed that reaction-limited aggregates were denser and had shapes closer to spheres than diffusion-limited aggregates. In Figure III.15a, we present clusters that appeared during diffusion-limited aggregation when CeO_2 particles traveled

in porous media at 500 PV. They had a fractal dimension of 1.55 and asphericity of 0.53. As shown in Figure III.15b, clusters were formed in the reaction-limited aggregation regime with a fractal dimension of 1.95 and asphericity of 0.3. Similar results have been found in prior literature. The difference in morphology is a consequence of the attachment efficiency. In the diffusion-limited aggregation, the attachment efficiency was 1, which means that two particles agglomerated upon their first collision. On the contrary, the attachment efficiency in reaction-limited aggregation is less than one and its value depends on the repulsive force. In this case, two particles need to collide many times before they permanently stick to each other, which gives them more chances to achieve a more spherical and denser configuration.[82]

Figure III.14e is a presentation of the particle size distribution in the two aggregation regimes for CeO_2 particles in the porous medium at 500 PV. It is reasonable that the probability to find large particles in diffusion-limited aggregation was considerably higher than in reaction-limited aggregation. When multimer particles collided, they had a high probability to attach to each other, so the agglomerate size increased faster than when multiple collisions between monomer particles were necessary.

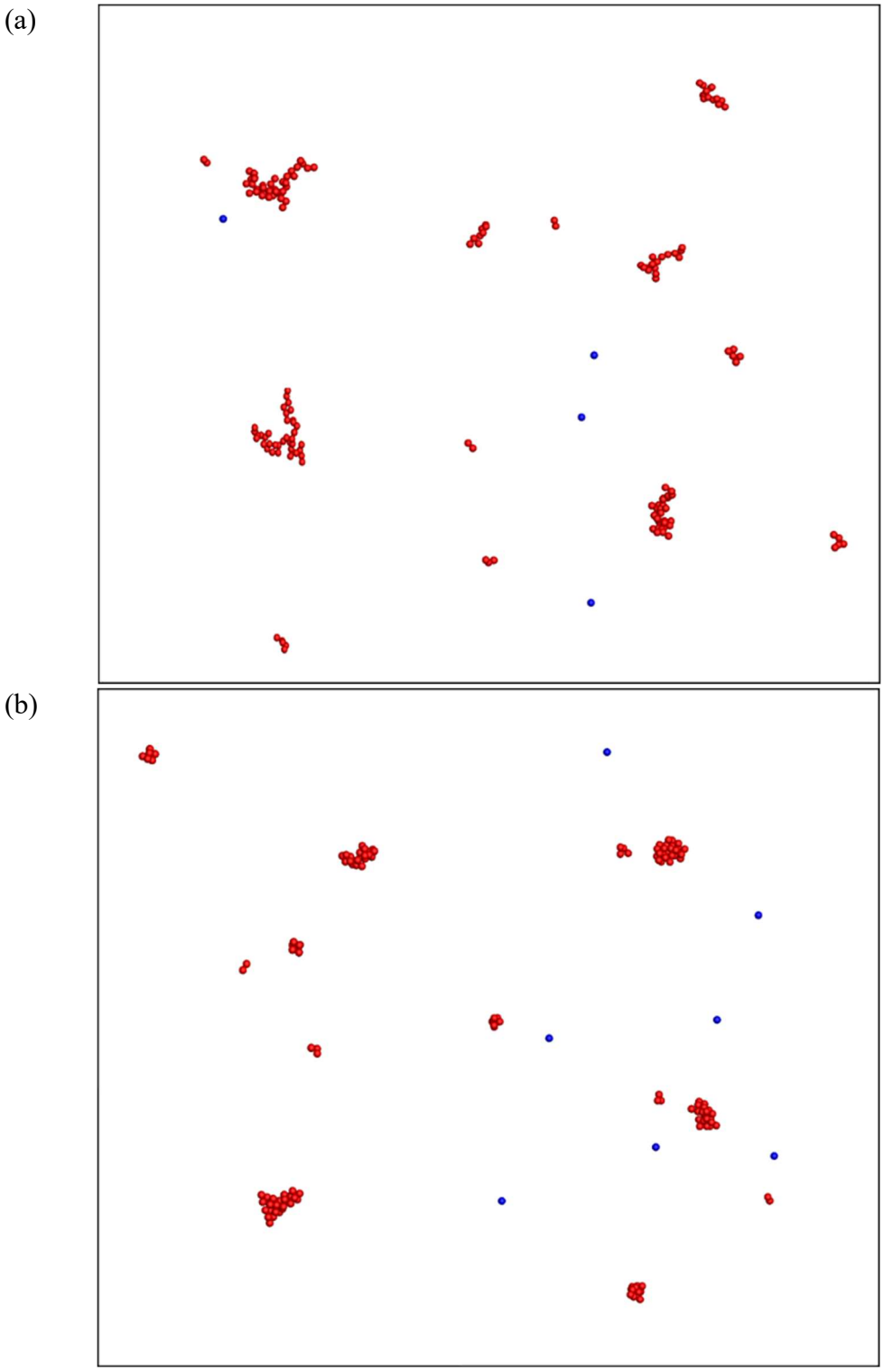


Figure III.15. Illustration of computed clusters in (a) diffusion-controlled aggregation with D_f = 1.55, A_s = 0.53, and (b) reaction-controlled aggregation with D_f= 1.9, A_s = 0.3. The solid phase of the porous medium is not shown. Red dots represent agglomerates, while blue dots are monomer particles that did not yet agglomerate.

III.3.2.b. Effects of the pore velocity on diffusion-limited aggregation

The velocity of the fluid in the pores plays a rather important role in the aggregation rate of nanoparticles and the morphology of aggregates in the diffusion-controlled regime, as shown in Figure III.16. It can be seen in Figure III.16a that the aggregation kinetics decreased as the pore velocity increased. When the pore velocity increased, the particles moved faster through the porous medium; and their residence time was too short for them to interact and agglomerate with other particles. This finding is similar to the results from a previous computational study[76] and experiments.[12,183] For example, Bizmark et al.[12] used confocal microscopy to visualize the process of particles injected through a column packed with spheres. At a high injection rate (high pore velocity), particles were distributed along the column while at a low injection rate, particles were aggregated and localized near the inlet of the column. The experimental outcomes proved that aggregation occurred quickly at low pore velocity; and aggregates, which were formed near the inlet, blocked the movement of small particles. On the other hand, at high velocity, fewer aggregates were produced and particles could travel through the whole column easily.

Based on Figure III.16c, the aggregates, produced at high pore velocities, had high fractal dimensions. A similar result was found in a prior study of Turetta et al.[184] Colloidal particles aggregated fast at low sedimentation velocity to form clusters with low fractal dimension, while aggregates produced slowly at high sedimentation velocity had high fractal dimension. This aligns with the expectation that aggregates, formed at slower kinetics, achieved a denser structure. When particles aggregated faster, the number of single particles dropped significantly, as seen in Figure III.16b. Thus, throughout the aggregation process, aggregates grew as a result of collisions among multimer particles, which produces clusters with more open branches and low fractal dimension.[82]

On the contrary, when aggregation kinetics is slow, the number of single particles decreased slowly; and the aggregation occurred mainly due to single particle-multimer particle collisions. Hence, single particles filled the empty space within clusters to create aggregates with high fractal dimension.

The fluid velocity did not impact on the asphericity, as shown in Figure III.16d. When particles traveled through porous media at different pore velocities, the aggregates formed during such processes almost have the same asphericity of around 0.5. Figures III.16a, III.16b, and III.16c illustrate three different ways that a small particle, represented by a blue circle, attaches to a large cluster, displayed in red color. In Figures III.17a and III.17b, the small particle attaches to the larger one in ways that reduce the compactness (i.e., the fractal dimension) of the cluster. Simultaneously, by changing the cluster boundary, its asphericity is affected. In Figure III.17c, the single particle fills an empty space in the existing cluster, which enhances the fractal dimension without changing the boundary enclosing the cluster (i.e., the asphericity). In our case, the high velocity greatly increased the fractal dimension and did not affect the asphericity. Thus, it is rational to hypothesize that at high velocities, filling the gap within existing clusters with small particles (as in Figure III.17c) was favorable in the aggregation process.

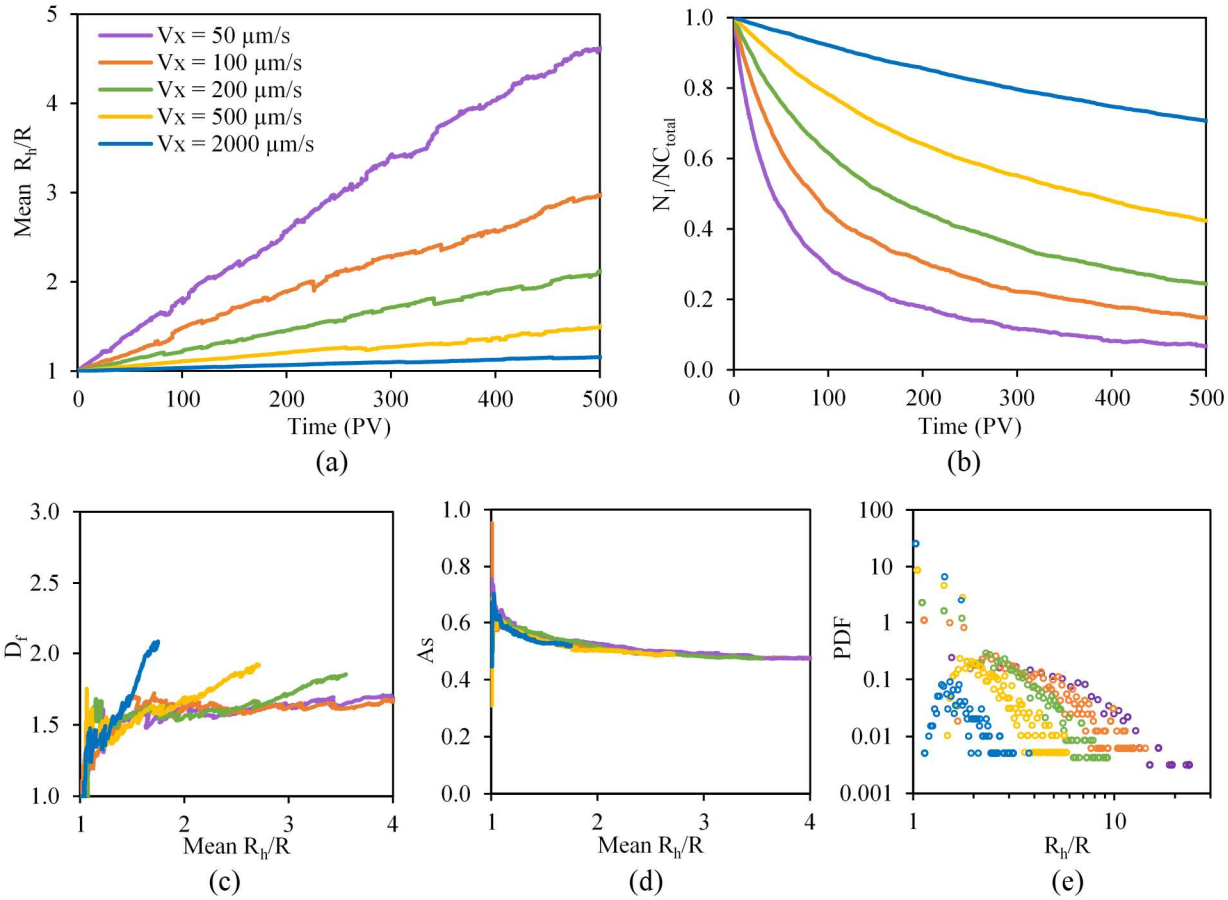


Figure III.16. Effects of the pore velocity on (a) the aggregation kinetics, (b) the ratio between the number of single particles over the total number of clusters, (c) the fractal dimension, (d) the asphericity, and (e) the probability density function of cluster size at t = 500 PV in the diffusion-limited regime. Particles, suspended in 0.2M KCl solution, traveled through randomly packed spheres with the pore velocity varying from 50 µm/s to 2000 µm/s.

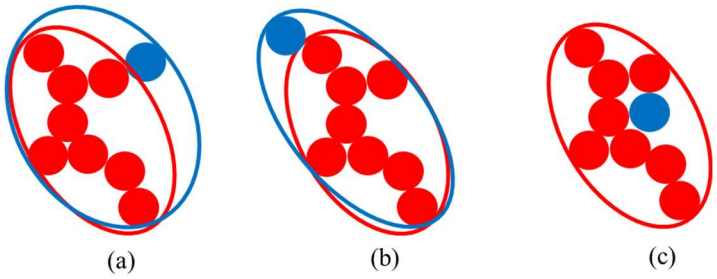


Figure III.17. The attachment of a single particle in blue color to a large cluster in red color (a) reduces the fractal dimension and asphericity because the boundary is expanded from the red ellipse to the blue ellipse, (b) lowers the fractal dimension and improves the asphericity since the blue boundary differs from a sphere, (c) enhances the fractal dimension without changing the asphericity.

III.3.2.c. Effects of the pore velocity on reaction-limited aggregation

The pore velocity was found to accelerate the aggregation kinetics of nanoparticles in porous media, as clearly shown in Figures III.18a and III.18b. In our study, when the pore velocity was 2,000 μm/s, the aggregation of particles became insignificant. It is noticed in Figure III.18c that the computed fractal dimension of aggregates at different pore velocities fluctuated. The reason is that due to slow kinetics in reaction-limited aggregation, the number of aggregates was small; thus, the fractal dimension was very sensitive to any changes related to the size of aggregates. Moreover, the average fractal dimension of clusters at different velocities was almost similar and around 1.9, which was much higher than that in the diffusion-controlled aggregation at low pore velocities. Similarly, no difference was observed for the asphericity of clusters at different pore velocities; and its value was around 0.3. This is understandable because aggregation was in the reaction-limited regime regardless of the pore velocity; hence, the morphology of aggregates was mainly controlled by the aggregation regime or ionic strength.

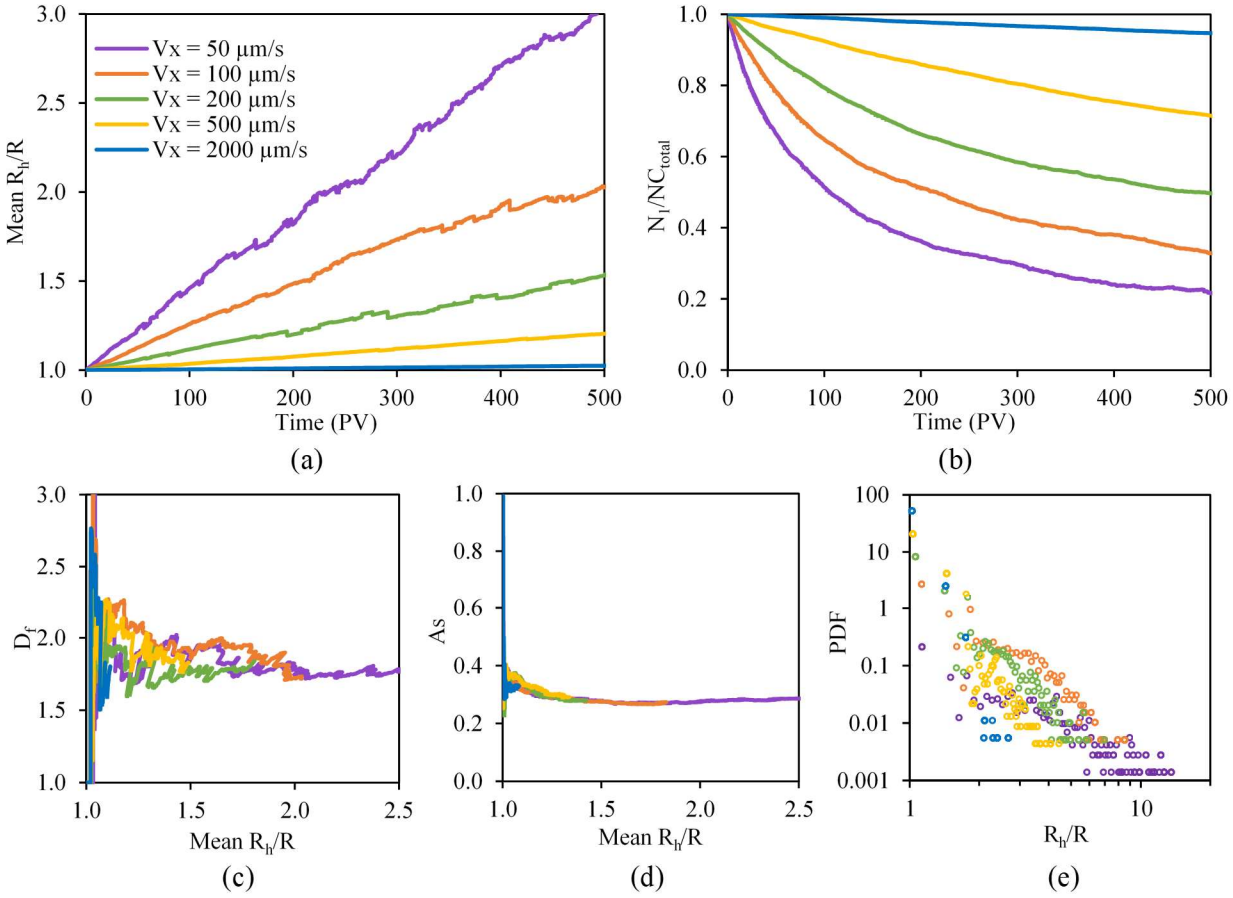


Figure III.18. Effects of the pore velocity on (a) the aggregation kinetics, (b) the ratio between the number of single particles over the total number of clusters, (c) the fractal dimension, (d) the asphericity, and (e) the probability density function of cluster size at t = 500 PV in the reaction-limited regime. Particles, suspended in 0.02M KCl solution, traveled through randomly packed spheres with the pore velocity varying from 50 µm/s to 2000 µm/s.

III.3.2.d. Effects of the particle size on diffusion-limited aggregation

Effects of the particle size in diffusion-reaction aggregation were investigated by changing the particle size as well as the number of nanoparticles, while the particle concentration was constant at 10mg/L. Figures III.19a and III.19b indicate that the kinetics of diffusion-controlled aggregation increased with a decrease in the single particle radius. The high molecular diffusivity of small particles caused an increase in the number of particle-particle collisions. The reduction in particle size for the same concentration would lead to increase in the specific area of the particles, as well as the electrostatic repulsion force. However, in diffusion-controlled aggregation, the van

der Waals force was dominant over the repulsion force. Therefore, the increase in the repulsion force did not have an effect; and in this case, the particle size reduction enhanced the molecular diffusivity and the collision efficiency of particles without reducing the probability to aggregate, thereby promoting the aggregation rate.

Even though the particle size affected the aggregation rate, it did not alter the morphology of diffusion-limited aggregates, as shown in Figures III.19c and III.19d. In a previous study out of our laboratory, large particles had large Lagrangian timescales and dropped off their streamlines slowly (due to small molecular diffusivity).[65] Lagrangian timescale is the period of time that the velocities of particles still correlate with their initial velocities. After this period of time, particles no longer correlate with their initial velocities and no longer travel on their initial streamlines. Thus, the large Lagrangian timescale or the poor flexibility in changing streamlines of large particles reduced the attachment among particles arriving at a cluster from various directions, and thus the fractal dimension. However, the large particles with slow aggregation kinetics should promote the fractal dimension. As a result of balancing the slow aggregation kinetics and the large Lagrangian timescale of large particles, the clusters produced by large particles in general did not have higher fractal dimensions than those formed by the small particles. Thus, the fractal dimension and asphericity reached the typical values of diffusion-limited aggregates, which is about 1.6 and 0.55, respectively. Our results related to the fractal dimension agree with experimental findings of Chowdhury and co-workers.[185] By performing aggregation experiments of TiO_2 suspended in KCl solution, they concluded that the fractal dimension was insensitive to the particle size when the attachment efficiency was close to 1.

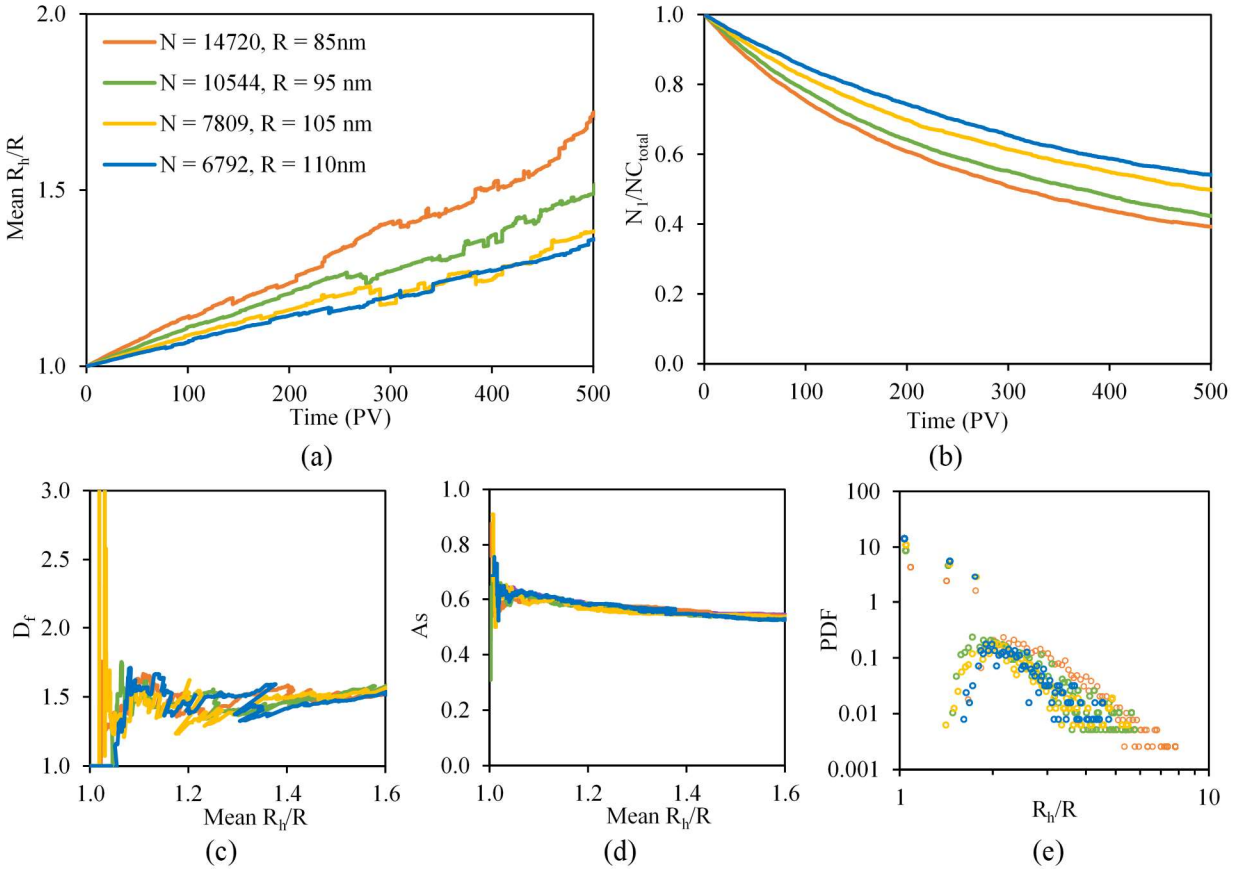


Figure III.19. Effects of the particle size on (a) the aggregation kinetics, (b) the ratio between the number of single particles over the total number of clusters, (c) the fractal dimension, (d) the asphericity, and (e) the probability density function of cluster size at t = 500 PV in diffusion-limited regime. Particles, suspended in 0.2M KCl solution, traveled through randomly packed spheres at the pore velocity 500 µm/s.

III.3.2.e. Effects of the particle size on the reaction-limited aggregation

The effects of the primary particle size on the reaction-limited aggregation and the diffusion-limited aggregation were not the same. The aggregation rate of single particles with a radius of 85 nm was less than that of larger primary particles as seen in Figure III.20a. However, Figure III.20b shows that when the size of primary particles was larger than 85 nm, aggregation kinetics did not change. The high molecular diffusivity of small particles increased the collision efficiency, which facilitated agglomeration. However, small particles had higher specific areas that caused an increase in repulsion forces between particles, reduced attachment efficiency, and

hindered agglomeration. Hence, when the particle size was small, enhancement of the electrostatic force (or reduction of sticking efficiency) was dominant over the increase in collision efficiency, thereby slowing down the aggregation kinetics. Once the particle size became larger than a certain value, the increase in collision probability and the reduction of attachment efficiency balanced out; thus, there were no changes in the aggregation rates of particles sized larger than 95 nm.

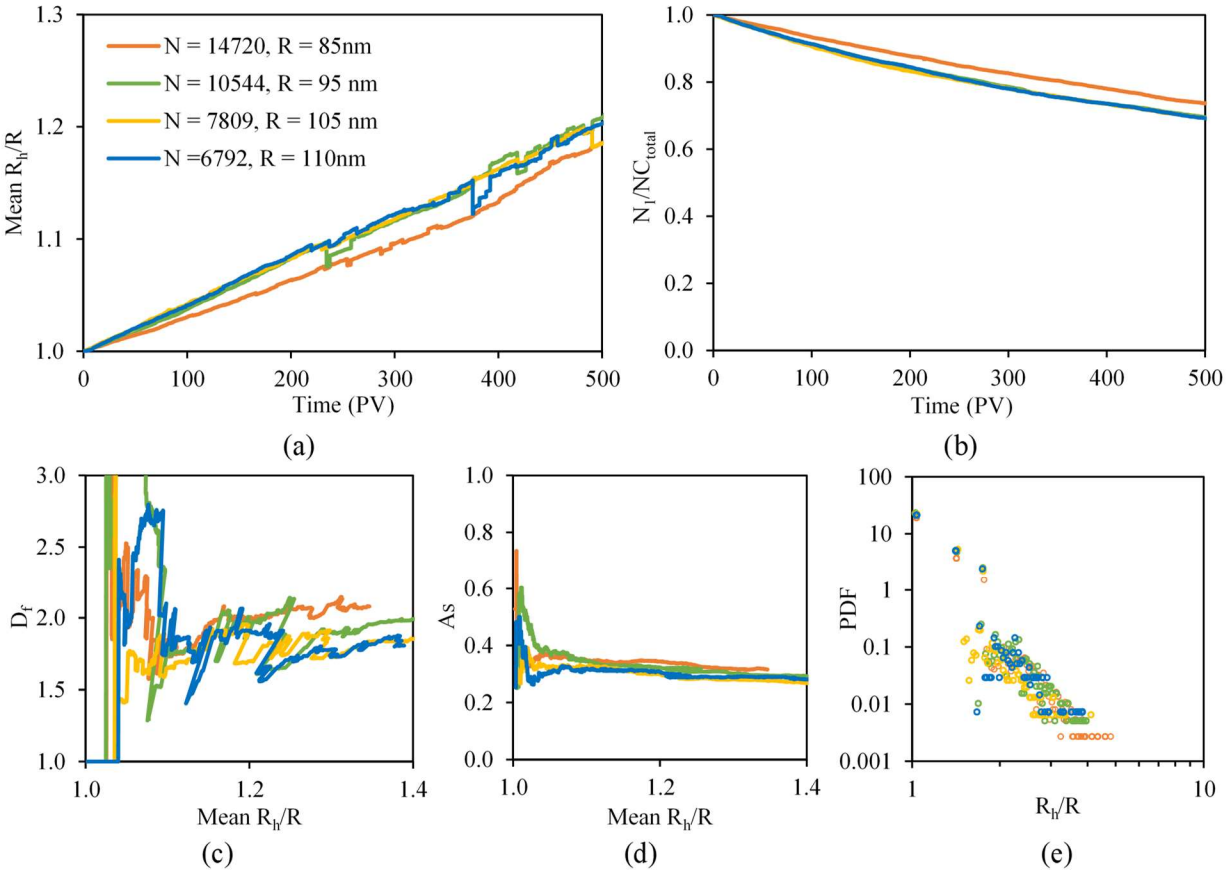


Figure III.20. Effects of the particle size on (a) the aggregation kinetics, (b) the ratio between the number of single particles over the total number of clusters, (c) the fractal dimension, (d) the asphericity, and (e) the probability density function of cluster size at t = 500 PV in the reaction-limited regime. Particles, suspended in 0.02M KCl solution, traveled through randomly packed spheres at the pore velocity of 500 μm/s.

When the primary particle size increased, the attachment efficiency declined and particles had to collide many times before aggregating with others, which helped them to gain some degree of interpenetration and a high fractal dimension.[82] Chowdhury et al.[185] obtained similar results

regarding the effect of particle size on reaction-controlled aggregates. The fractal dimension of aggregates formed by the aggregation of primary particles with high specific areas (or small radii) was greater than that of aggregates produced by the aggregation of single particles with small specific areas (or large radii).

III.3.2.f. Formation and behavior of large clusters

One noteworthy finding from the computations was the creation of some very large aggregates. Observations indicate that particles suspended in high electrolyte concentrations and moving through porous media at low pore velocities tend to aggregate rapidly, resulting in the formation of very large clusters over long residence times. For example, when particles moved through randomly packed spheres at 100 μm/s, in 0.2M KCl solution, many clusters that can be called "giant" were found to be very close to the grains at t = 1,000 PV, as shown in Figure III.21. These giant clusters were very close in shape with clusters observed in microscopic images taken in laboratory experiments.[186,187] Among them, the largest clusters consisted of 3,510 single particles, which was almost a third of the total number of primary particles in the simulation box. Figure III.22a is an illustration that aggregation kinetics kept increasing with time, while the ratio of the number of primary particles and the total number of clusters (N_1/NC_{total}) dramatically dropped from 1 at zero PV to around 0.2 at 400 PV and slightly changed in value afterwards. This could be explained by the fact that when the number of single particles or small clusters was low, large particles aggregated with each other to create much larger clusters. It can be seen in Figure III.22e, after 400 PV, the tails of particle size distributions were remarkedly extended. At 1,000 PV, the radius of the largest aggregate was 80 times larger than the single particle radius. Due to the confined geometry, the large clusters starting to deposit on the grains were often denser and

had high fractal dimensions, which lifted D_f of all clusters in the simulation box from 1.6 to 1.86, as seen in Figure III.21c and slightly lowered As.

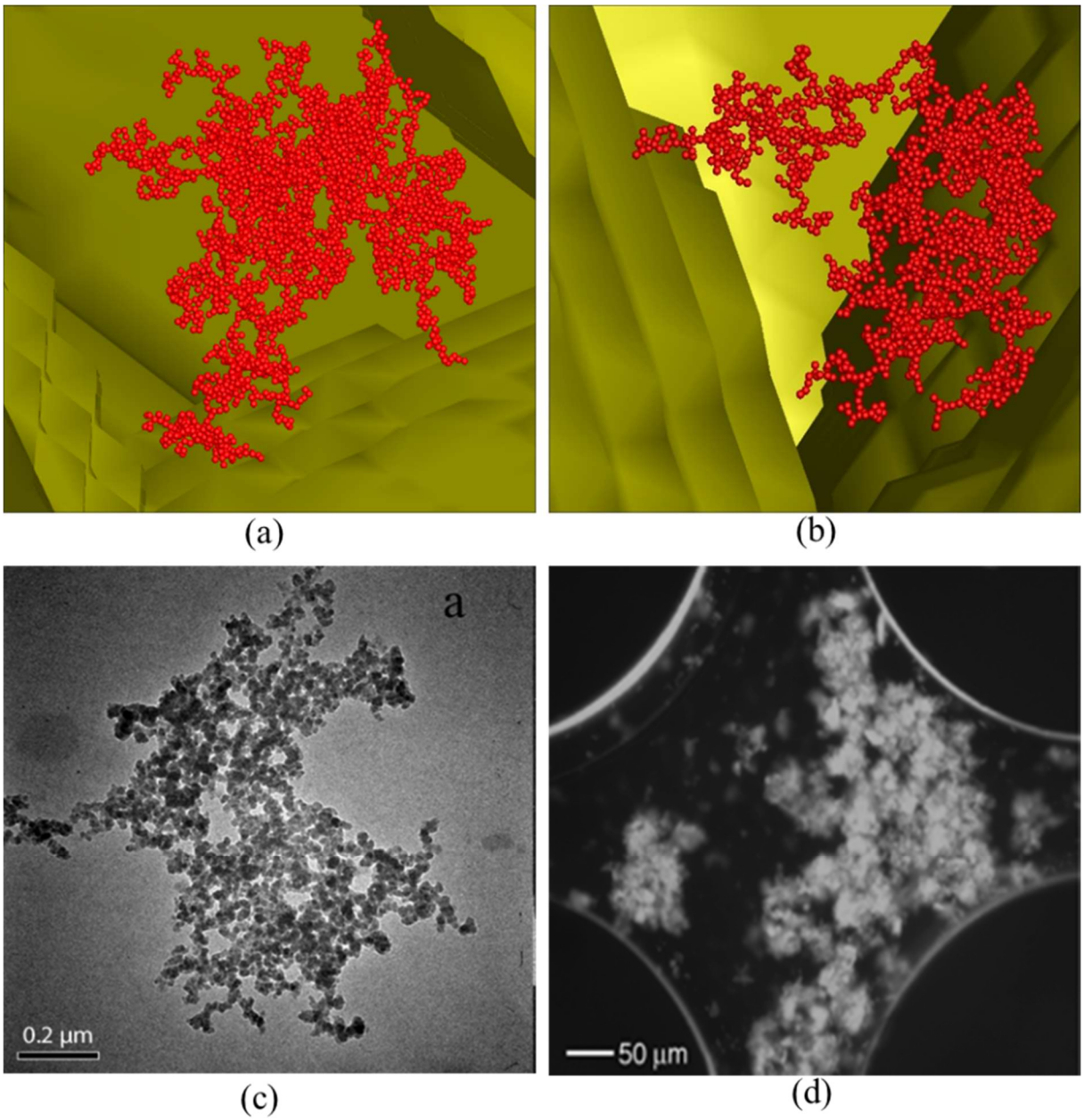


Figure III.21. Images of (a), (b) two enormous ceria clusters obtained by our simulations (particles involved in the aggregation are shown in red; and the solid matrix of the porous medium is displayed in yellow), (c) a large silica cluster obtained by the lab microscope (reprinted from a publication[186] with permission from Elsevier), (d) a large titania aggregate obtained by the lab microscope (reprinted from a publication[67] with permission from American Chemical Society).

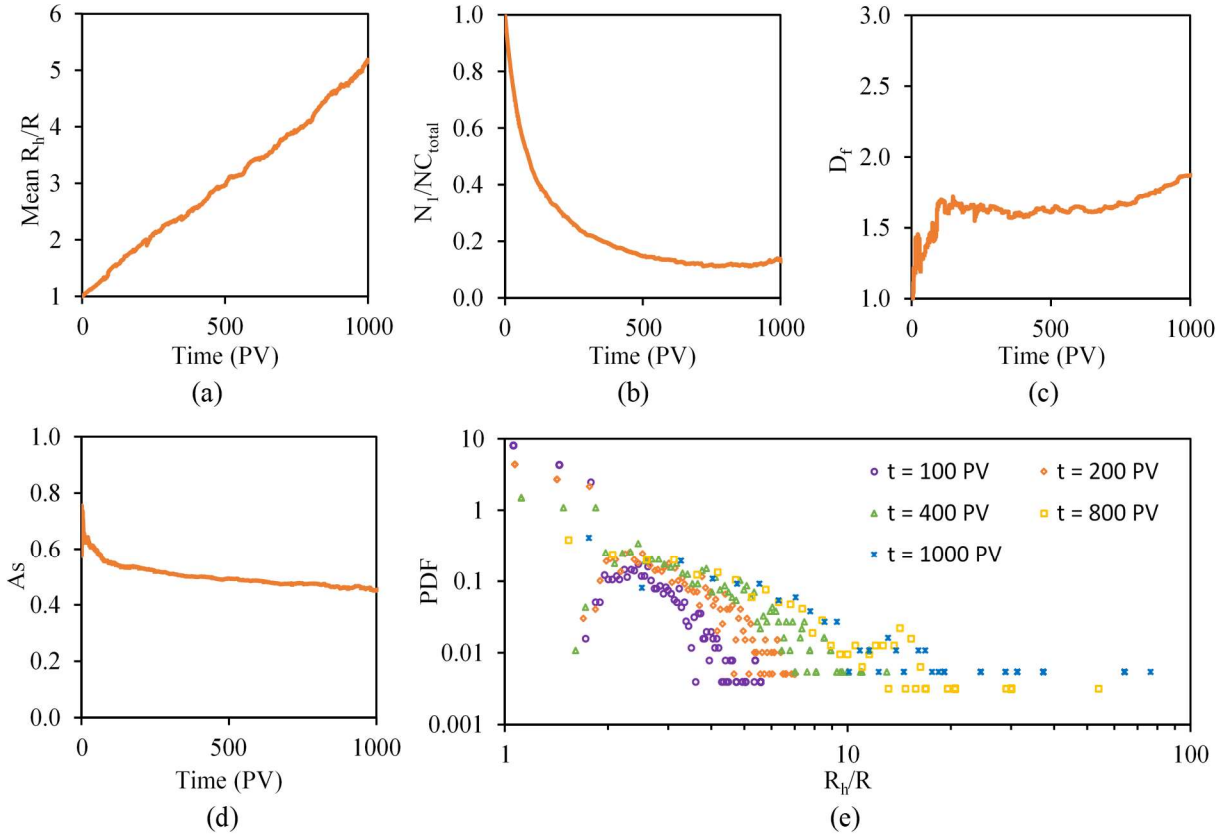


Figure III.22. Simulation results of CeO_2 particles in 0.2M KCl solution through a sphere packing, at 100 µm/s, from 0 PV to 1000 PV include (a) aggregation kinetics, (b) the ratio between the number of single particles and the total number of clusters, (c) the fractal dimension, (d) the asphericity, and (e) the cluster size probability density function at different times such as 100 PV, 200 PV, 400 PV, 800 PV and 1000 PV.

III.3.2.g. Positions of clusters relative to the walls and their velocities

Scatter plots in Figure III.23a illustrate the minimum distances from clusters to the nearest walls at different times 0 PV, 400 PV, 800 PV, and 1200 PV when 10 mg/L CeO_2 particles, suspended in 0.2 M KCl, traveled through the pore space between randomly packed spheres with the average pore velocity of 500 µm/s in the streamwise direction. Each point represents the minimum distance from a cluster, which could be a single particle or an aggregate containing many single particles, to the wall. The minimum distance from a cluster to the wall is the smallest distance from the surface of a particle within the cluster to the nearest wall. It can be seen that at t = 0 PV, all the particles were randomly distributed in the simulation domain; thus, the distances

from clusters to the wall varied from almost 0 to 26 lattice units (one lattice unit is equal to the grid resolution, *dx*). As time went by, there were more aggregates produced, and the large clusters were found to be closer to the walls. Similarly, the velocity magnitudes of large clusters varied in a small range of low values, while single particles or small aggregates obtained a wide range of velocity magnitude. In general, the large particles stayed closer to the solid phase of porous media and traveled at low velocities. At t = 1200 PV, it is observed that there were many large clusters (consisting of more than 100 particles) remaining stationary near the grains. Among them, a cluster with 125 primary particles was found. The distances from each particle within the cluster to the nearest walls at 0 PV, 400 PV, 800 PV, and 1200 PV were used to draw the distance and velocity profile for each particle, as shown in Figure III.24. The cluster, staying still near the grain, was a result of the aggregation of 125 single particles, which is located at various positions relative to walls (from 0 to 21 lattice units) at t = 0 PV. Their velocity magnitudes were also very divergent, showing that the cluster was formed by both slow-moving and fast-moving particles. A similar analysis, performed for a cluster produced by 167 particles is displayed in Figure III.25; and it reveals the same conclusion.

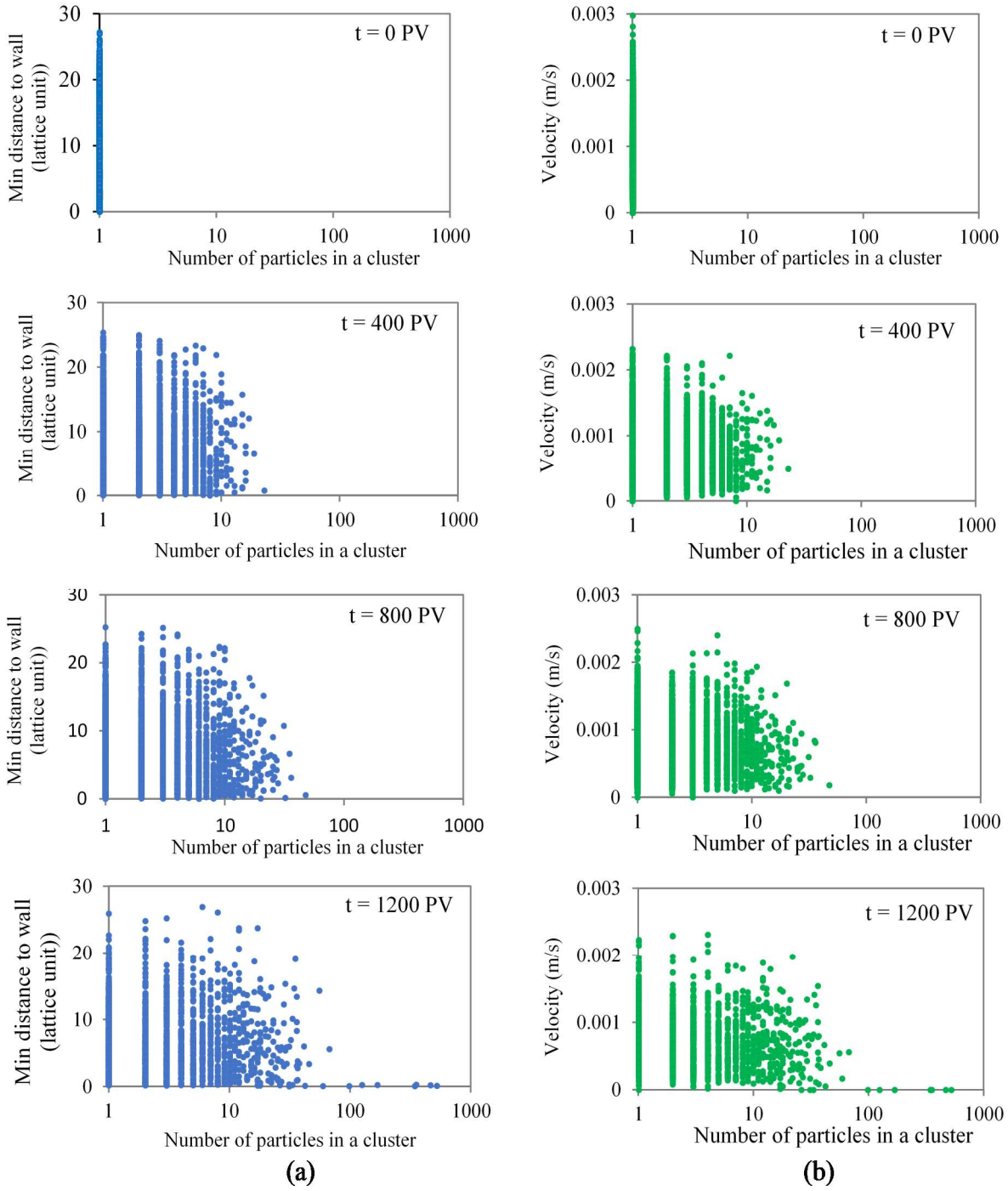
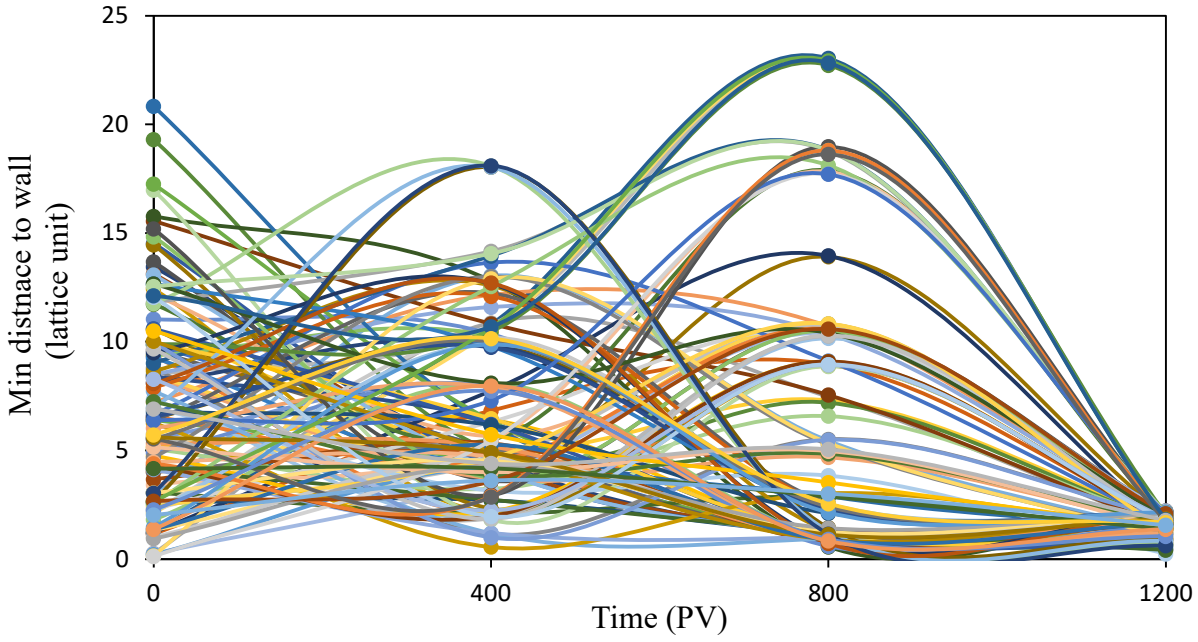
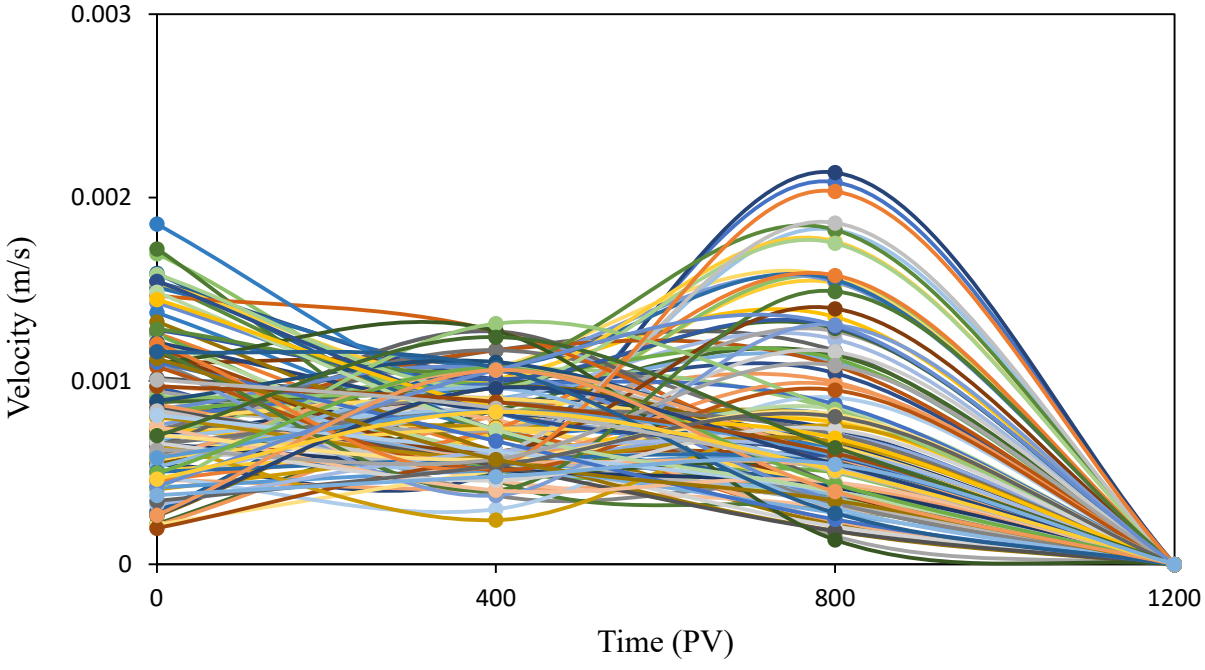


Figure III.23. (a) Distances from clusters to the nearest walls at different times such as 0 PV, 400 PV, 800 PV, and 1200 PV and (b) the velocities of clusters at different times such as 0 PV, 400 PV, 800 PV, and 1200 PV. One dot represents a cluster which can be a single particle or an aggregate containing multiple particles. The distance from a cluster to the wall is the minimum distance from the surface of the particle (in the cluster) that is nearest to the wall.

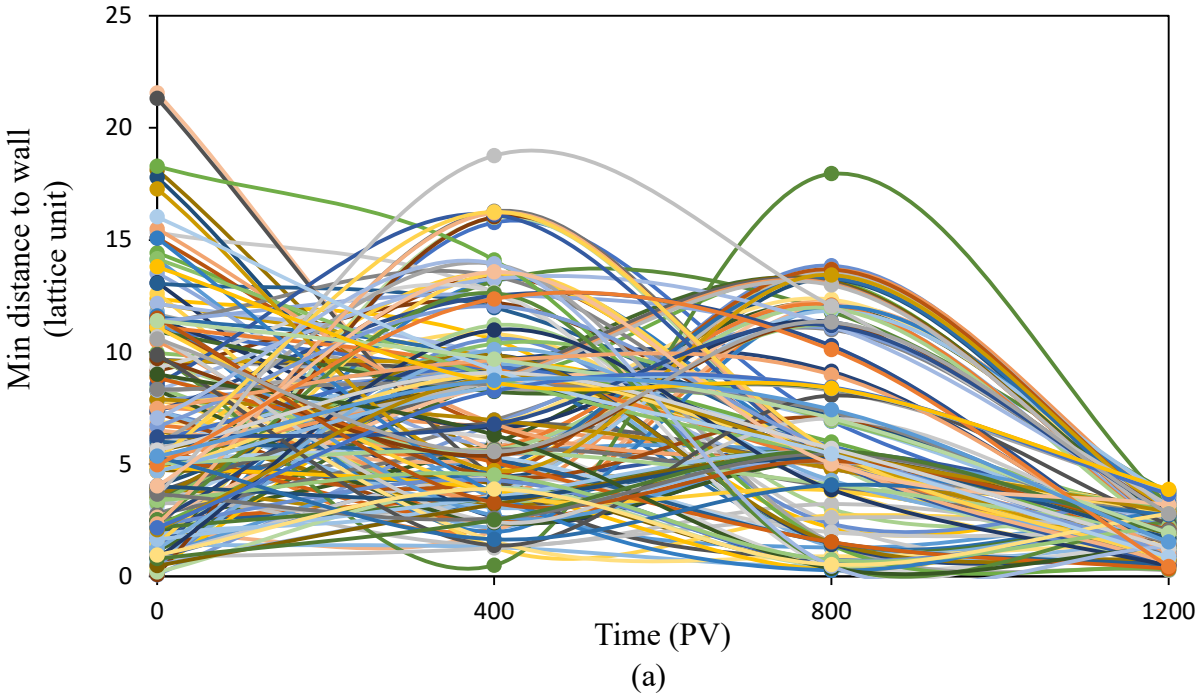


(a)

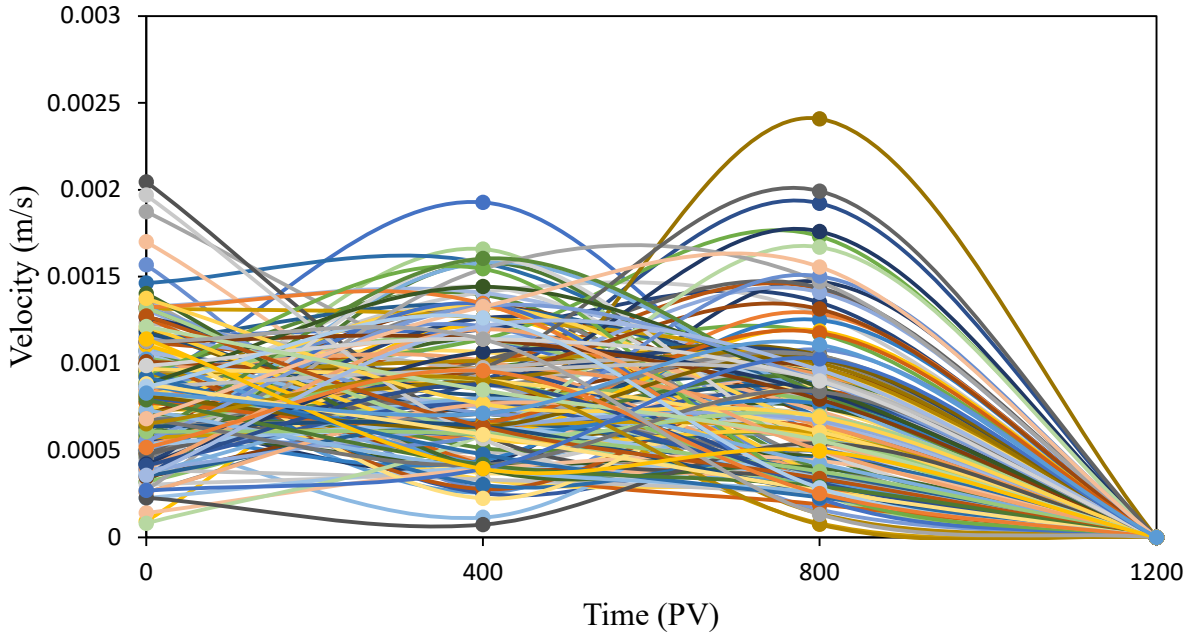


(b)

Figure III.24. (a) Distances from the porous medium matrix wall for 125 primary particles, which formed a 125-particle cluster at 1200 PV. The distances shown are to the nearest wall at times of 0 PV, 400 PV, 800 PV, and 1200 PV and (b) velocities of the same125 primary particles at 0 PV, 400 PV, 800 PV, and 1200 PV. Each line is representing results for one particle.



(a)



(b)

Figure III.25. (a) Distances to the nearest wall for 167 primary particles, which formed a 167-particle cluster at 1200 PV. The distances to the wall are reported for different times at 0 PV, 400 PV, 800 PV, and 1200 PV and (b) velocities of the same 167 primary particles at 0 PV, 400 PV, 800 PV, and 1200 PV. Each line is one particle.

IV. CONCLUSIONS AND FUTURE PLANS

IV.1. Conclusions

It is possible to draw the following conclusions based on the results of various topics presented here:

The Weibull distribution is a good fit for the distributions of the normalized velocity magnitude for flow through sphere packings and scaffolds. More interestingly, the velocity distributions in the geometries with random configurations, such as random sphere packings, fiber scaffolds, and randomly foamed scaffolds followed one unique Weibull equation with a scale factor of 1.212 and a shape factor of 1.062 within statistical accuracy. Not only data obtained herein but also data obtained elsewhere[1] follow this distribution. The distribution appeared to be the same when the pore size distribution was continuous. However, because of the orderly structure of geometries in SC, BCC, and FCC, their pore area distributions were discrete and the velocity distribution in the structured sphere packings including SC, BCC and FCC could not be predicted with that Weibull equation. In other words, their regular structure makes the fluid mechanics more like varying-cross-section capillaries than true porous media; therefore, the corresponding velocity distribution fails to conform with that of the unstructured media. A different Weibull distribution (with $\alpha = 0.867$, $\beta = 0.935$) was found to be a good fit for velocity distributions of flows through SC and BCC whereas the Weibull distribution (with $\alpha = 1.499$, $\beta = 1.102$) described the flow velocity through FCC within statistical accuracy.

More interestingly, the pore structure of a porous medium was found to determine the velocity distribution of fluid flow through that medium. The velocity magnitude distribution of fluid flow through a porous medium and the pore volume distribution, which was continuous, were statistically similar. This result enables the prediction of the velocity probability density function

(PDF) if an experimentally obtained pore volume distribution is available. In such a scenario, the average fluid velocity magnitude within the pores can be determined by dividing the superficial velocity (Darcy velocity) of the fluid by the porosity of the medium, and subsequently applying the pore size distribution. In addition, it is possible to create porous media with predetermined pore volume distributions, which can be used to manipulate the pore velocity distribution.

Hydrodynamic dispersion is one of those porous media-related topics that are typically associated with a lot of uncertainty and a lack of fundamental understanding, even though several applications are critically dependent on predicting dispersion in porous media. The conventional approach has been the Eulerian approach, often through macroscopic tools of analysis. Dispersion, however, is an effect that is driven by particle transport phenomena that are below the scale of consideration for macro-scale models. The present study was focused on providing a fresh approach and on identifying the relevant parameters, dimensionless numbers, and quantities. Given the currently available computational techniques that allow for in-depth calculations devoid of empiricisms, such as the use of lattice Boltzmann models and specialized particle tracking algorithms that provide paths of individual particles from a Lagrangian perspective, it is possible to analyze hydrodynamic dispersion in a physically sound framework and to probe its relationship to the effective Peclet number from both the Eulerian and Lagrangian viewpoints. The results led to the definition of a Peclet number that is based on more naturally relevant scales rather than using Eulerian macroscopic quantities. The length scale used in defining an effective Eulerian Peclet number was the diameter of the spheres making up the porous media and was constant for a certain porous medium configuration. In contrast, the effective Lagrangian Peclet number was calculated from the Lagrangian length and time scales, which varied with molecular diffusion (i.e., the Schmidt number), the fluid velocity, and the pore geometry. This new definition has a strong

impact on simplifying and unifying the correlation between the ratio of dispersion over diffusion with the Peclet number in packed beds, $\frac{D_L}{D'_m} = 1 + A\ Pe'^L_m$. This unified correlation reveals a linear dependence on the effective Lagrangian Peclet number for different packing types, with the clear appearance of a geometrical coefficient A as the slope of the line. We conclude that the Lagrangian scales are the appropriate scales for studying hydrodynamic dispersion, as one might have predicted because both molecular diffusion effects and flow are taken into consideration

The work, related to aggregation of NPs, describes simulation results from a multiscale process that involves the aggregation and movement of NPs through porous media. The aggregate morphology was examined by computing the fractal dimension and asphericity of clusters. Effects of the ionic strength, pore velocity and particle size on the aggregation process of Cerium oxide NPs in randomly packed spheres were investigated. The ionic strength was found to be the most important factor affecting both aggregation kinetics and morphology of aggregates. At electrolyte concentration above the CCC, the attachment efficiency was unity, and aggregation kinetics were fast. However, diffusion-limited aggregates had low fractal dimension and high asphericity. On the other hand, at electrolyte concentration below the CCC, the attachment efficiency was less than one; and reaction-limited aggregation occurred at low speeds producing denser aggregates that had high fractal dimension and low asphericity. The pore velocity also had strong effects on aggregation kinetics and the morphology of aggregates in diffusion-controlled aggregation, while particle size only had a clear impact on changing the fractal dimension of reaction-limited aggregates. The computational model is based on Newton's second law of motion. It also considers interaction forces between particles, thereby reflecting the physics of the aggregation process without using any probabilistic model. In addition, it could predict the fractal dimension, the asphericity, and the size distribution of particles with time. However, it certainly has some

drawbacks. For example, the accuracy of results is mainly dependent on the force fields between particles; however, knowing the parameters for the force fields, such as the Hamaker constant, the surface potential, and so on, is not simple. Some types of particles might require more complicated force fields, which could include Lewis acid-base interactions. To overcome this drawback, it would be required to perform atomistic simulations or experiments in bulk to determine the force fields. In addition, the model can be improved by adding the particle-wall interactions, rotational movement of particles, and the effects of large aggregates on the flow field in a two-way coupling model.

IV.2. Future Plans

Modeling the aggregation process of nanoparticles in porous media is newly developed so a lot of improvements should be done for the current aggregation model, and there are several areas that future research can focus on.

- ✓ Incorporating the interactions between particles and the solid phase of porous media is a crucial step to accurately model the aggregation process. The surface chemistry of the porous media can influence the aggregation behavior of nanoparticles, and incorporating this effect into the model can provide more accurate predictions.
- ✓ The effect of large aggregates on the flow fields is another important aspect to consider. Large aggregates can alter the flow fields by creating additional resistance to the fluid flow, which can in turn affect the aggregation process. Therefore, including the effect of large aggregates in the model is necessary.
- ✓ The impact of the rotational movement of aggregates on the aggregation process is another important factor to consider in the model. Taking this effect into account can improve the

accuracy of predictions (especially on the morphology of aggregates), as rotational movement can affect the rate of collision and attachment between nanoparticles.

- ✓ Additionally, it would be interesting to investigate how different types of porous media (e.g., bidisperse, tridisperse, sandstones, etc.) can affect the aggregation of nanoparticles and the configuration of the aggregates. Different porous media have varying pore structures and surface chemistries, which can impact the behavior of nanoparticles within them.
- ✓ Finally, it would be beneficial to further examine the impact of the Peclet number on the aggregation process. The Peclet number, which is the ratio of advection to diffusion, can influence the transport of nanoparticles in porous media. Investigating this effect can provide insights into the behavior of nanoparticles in different flow regimes, and can inform the development of more accurate aggregation models.

REFERENCES

(1) Souzy, M.; Lhuissier, H.; Méheust, Y.; Le Borgne, T.; Metzger, B. Velocity Distributions, Dispersion and Stretching in Three-Dimensional Porous Media. *J. Fluid Mech.* **2020**, *891*, A16. https://doi.org/10.1017/jfm.2020.113.

(2) De Paoli, M.; Giurgiu, V.; Zonta, F.; Soldati, A. Universal Behavior of Scalar Dissipation Rate in Confined Porous Media. *Phys. Rev. Fluids* **2019**, *4* (10), 101501. https://doi.org/10.1103/PhysRevFluids.4.101501.

(3) Matyka, M.; Gołembiewski, J.; Koza, Z. Power-Exponential Velocity Distributions in Disordered Porous Media. *Phys. Rev. E* **2016**, *93* (1), 013110. https://doi.org/10.1103/PhysRevE.93.013110.

(4) Siena, M.; Riva, M.; Hyman, J. D.; Winter, C. L.; Guadagnini, A. Relationship between Pore Size and Velocity Probability Distributions in Stochastically Generated Porous Media. *Phys. Rev. E* **2014**, *89* (1), 013018. https://doi.org/10.1103/PhysRevE.89.013018.

(5) de Anna, P.; Quaife, B.; Biros, G.; Juanes, R. Prediction of the Low-Velocity Distribution from the Pore Structure in Simple Porous Media. *Phys. Rev. Fluids* **2017**, *2* (12), 124103. https://doi.org/10.1103/PhysRevFluids.2.124103.

(6) Pham, N. H.; Voronov, R. S.; Tummala, N. R.; Papavassiliou, D. V. Bulk Stress Distributions in the Pore Space of Sphere-Packed Beds under Darcy Flow Conditions. *Phys. Rev. E* **2014**, *89* (3), 033016. https://doi.org/10.1103/PhysRevE.89.033016.

(7) De Paoli, M.; Zonta, F.; Soldati, A. Influence of Anisotropic Permeability on Convection in Porous Media: Implications for Geological CO 2 Sequestration. *Phys. Fluids* **2016**, *28* (5), 056601. https://doi.org/10.1063/1.4947425.

(8) Dentz, M.; Icardi, M.; Hidalgo, J. J. Mechanisms of Dispersion in a Porous Medium. *J. Fluid Mech.* **2018**, *841*, 851–882. https://doi.org/10.1017/jfm.2018.120.

(9) Khan, I.; Saeed, K.; Khan, I. Nanoparticles: Properties, Applications and Toxicities. *Arab. J. Chem.* **2019**, *12* (7), 908–931. https://doi.org/10.1016/j.arabjc.2017.05.011.

(10) Jiang, X.; Tong, M.; Lu, R.; Kim, H. Transport and Deposition of ZnO Nanoparticles in Saturated Porous Media. *Colloids Surfaces A Physicochem. Eng. Asp.* **2012**, *401*, 29–37. https://doi.org/10.1016/j.colsurfa.2012.03.004.

(11) Fang, J.; Shan, X. quan; Wen, B.; Lin, J. ming; Owens, G. Stability of Titania Nanoparticles in Soil Suspensions and Transport in Saturated Homogeneous Soil Columns. *Environ.*

Pollut. **2009**, *157* (4), 1101–1109. https://doi.org/10.1016/j.envpol.2008.11.006.

(12) Bizmark, N.; Schneider, J.; Priestley, R. D.; Datta, S. S. Multiscale Dynamics of Colloidal Deposition and Erosion in Porous Media. *Sci. Adv.* **2020**, *6* (46), 1–11. https://doi.org/10.1126/sciadv.abc2530.

(13) Holland, T. A.; Mikos, A. G. Review: Biodegradable Polymeric Scaffolds. Improvements in Bone Tissue Engineering through Controlled Drug Delivery. In *Tissue Engineering I*; Springer Berlin Heidelberg, 2006; Vol. 102, pp 161–185. https://doi.org/10.1007/b137205.

(14) Kretlow, J. D.; Mikos, A. G. From Material to Tissue: Biomaterial Development, Scaffold Fabrication, and Tissue Engineering. *AIChE J.* **2008**, *54* (12), 3048–3067. https://doi.org/10.1002/aic.11610.

(15) Nguyen, D.; Balakotaiah, V. Flow Maldistributions and Hot Spots in Down-Flow Packed Bed Reactors. *Chem. Eng. Sci.* **1994**, *49* (24), 5489–5505. https://doi.org/10.1016/0009-2509(94)00360-2.

(16) Cartmell, S. H.; Porter, B. D.; García, A. J.; Guldberg, R. E. Effects of Medium Perfusion Rate on Cell-Seeded Three-Dimensional Bone Constructs in Vitro. *Tissue Eng.* **2003**, *9* (6), 1197–1203. https://doi.org/10.1089/10763270360728107.

(17) Olivares, A. L.; Lacroix, D. Simulation of Cell Seeding Within a Three-Dimensional Porous Scaffold: A Fluid-Particle Analysis. *Tissue Eng. Part C Methods* **2012**, *18* (8), 624–631. https://doi.org/10.1089/ten.tec.2011.0660.

(18) Pham, N. H.; Harwell, J. H.; Resasco, D. E.; Papavassiliou, D. V.; Chen, C.; Shiau, B. Transport and Deposition Kinetics of Polymer-Coated Multiwalled Carbon Nanotubes in Packed Beds. *AIChE J.* **2016**, *62* (10), 3774–3783. https://doi.org/10.1002/aic.15273.

(19) Agrawal, R.; West, D. H.; Balakotaiah, V. Modeling and Analysis of Local Hot Spot Formation in Down-Flow Adiabatic Packed-Bed Reactors. *Chem. Eng. Sci.* **2007**, *62* (18–20), 4926–4943. https://doi.org/10.1016/j.ces.2006.11.057.

(20) Jaffe, S. B. Hot Spot Simulation in Commercial Hydrogenation Processes. *Ind. Eng. Chem. Process Des. Dev.* **1976**, *15* (3), 410–416. https://doi.org/10.1021/i260059a011.

(21) Bergemann, C.; Elter, P.; Lange, R.; Weiï¿½mann, V.; Hansmann, H.; Klinkenberg, E. D.; Nebe, B. Cellular Nutrition in Complex Three-Dimensional Scaffolds: A Comparison between Experiments and Computer Simulations. *Int. J. Biomater.* **2015**, *2015*. https://doi.org/10.1155/2015/584362.

(22) Datta, S. S.; Chiang, H.; Ramakrishnan, T. S.; Weitz, D. A. Spatial Fluctuations of Fluid Velocities in Flow through a Three-Dimensional Porous Medium. *Phys. Rev. Lett.* **2013**, *111* (6), 064501. https://doi.org/10.1103/PhysRevLett.111.064501.

(23) Araújo, A. D.; Bastos, W. B.; Andrade, J. S.; Herrmann, H. J. Distribution of Local Fluxes in Diluted Porous Media. *Phys. Rev. E* **2006**, *74* (1), 010401. https://doi.org/10.1103/PhysRevE.74.010401.

(24) Maier, R. S.; Kroll, D. M.; Kutsovsky, Y. E.; Davis, H. T.; Bernard, R. S. Simulation of Flow through Bead Packs Using the Lattice Boltzmann Method. *Phys. Fluids* **1998**, *10* (1), 60–74. https://doi.org/10.1063/1.869550.

(25) Aramideh, S.; Vlachos, P. P.; Ardekani, A. M. Pore-Scale Statistics of Flow and Transport through Porous Media. *Phys. Rev. E* **2018**, *98* (1), 013104. https://doi.org/10.1103/PhysRevE.98.013104.

(26) Campolo, M.; Curcio, F.; Soldati, A. Minimal Perfusion Flow for Osteogenic Growth of Mesenchymal Stem Cells on Lattice Scaffolds. *AIChE J.* **2013**, *59* (8), 3131–3144. https://doi.org/10.1002/aic.14084.

(27) Voronov, R. S.; VanGordon, S. B.; Sikavitsas, V. I.; Papavassiliou, D. V. Distribution of Flow-Induced Stresses in Highly Porous Media. *Appl. Phys. Lett.* **2010**, *97* (2), 024101. https://doi.org/10.1063/1.3462071.

(28) Bakhshian, S.; Sahimi, M. Computer Simulation of the Effect of Deformation on the Morphology and Flow Properties of Porous Media. *Phys. Rev. E* **2016**, *94* (4), 042903. https://doi.org/10.1103/PhysRevE.94.042903.

(29) Vu, T. V.; Papavassiliou, D. V. Synergistic Effects of Surfactants and Heterogeneous Nanoparticles at Oil-Water Interface: Insights from Computations. *J. Colloid Interface Sci.* **2019**, *553*, 50–58. https://doi.org/10.1016/j.jcis.2019.05.102.

(30) Lowe, C. P.; Frenkel, D. Do Hydrodynamic Dispersion Coefficients Exist? *Phys. Rev. Lett.* **1996**, *77* (22), 4552–4555. https://doi.org/10.1103/PhysRevLett.77.4552.

(31) Dutta, D. Hydrodynamic Dispersion. In *Encyclopedia of Microfluidics and Nanofluidics*; Springer US: Boston, MA, 2013; pp 1–14. https://doi.org/10.1007/978-3-642-27758-0_660-3.

(32) Delgado, J. M. P. Q. Longitudinal and Transverse Dispersion in Porous Media. *Chem. Eng. Res. Des.* **2007**, *85* (9), 1245–1252. https://doi.org/10.1205/cherd07017.

(33) Perkins, T. K.; Johnston, O. C. A Review of Diffusion and Dispersion in Porous Media. *Soc. Pet. Eng. J.* **1963**, *3* (01), 70–84. https://doi.org/10.2118/480-PA.

(34) Koch, D. C.; Brady, J. F. Dispersion in Fixed Beds.Pdf. **1985**, *154*.

(35) Zhu, Y.; Fox, P. J. Simulation of Pore-Scale Dispersion in Periodic Porous Media Using Smoothed Particle Hydrodynamics. *J. Comput. Phys.* **2002**, *182* (2), 622–645. https://doi.org/10.1006/jcph.2002.7189.

(36) Ghanbarian, B.; Hunt, A. G.; Ewing, R. P.; Sahimi, M. Tortuosity in Porous Media: A Critical Review. *Soil Sci. Soc. Am. J.* **2013**, *77* (5), 1461–1477. https://doi.org/10.2136/sssaj2012.0435.

(37) Sahimi, M. Flow and Transport in Porous Media and Fractured Rock: From Classical Methods to Modern Approaches. *2nd ed. Wiley-VCH, Weinheim, Ger.* **2011**.

(38) Sahimi, M. Flow Phenomena in Rocks: From Continuum Models to Fractals, Percolation, Cellular Automata, and Simulated Annealing. *Rev. Mod. Phys.* **1993**, *65* (4), 1393–1534. https://doi.org/10.1103/RevModPhys.65.1393.

(39) Kim, A. S.; Chen, H. Diffusive Tortuosity Factor of Solid and Soft Cake Layers: A Random Walk Simulation Approach. *J. Memb. Sci.* **2006**, *279* (1–2), 129–139. https://doi.org/10.1016/j.memsci.2005.11.042.

(40) Clennell, M. Ben. Tortuosity: A Guide through the Maze. *Geol. Soc. Spec. Publ.* **1997**, *122* (122), 299–344. https://doi.org/10.1144/GSL.SP.1997.122.01.18.

(41) Moldrup, P.; Olesen, T.; Komatsu, T.; Schjønning, P.; Rolston, D. E. Tortuosity, Diffusivity, and Permeability in the Soil Liquid and Gaseous Phases. *Soil Sci. Soc. Am. J.* **2001**, *65* (3), 613–623. https://doi.org/10.2136/sssaj2001.653613x.

(42) Epstein, N. On Tortuosity and the Tortuosity Factor in Flow and Diffusion through Porous Media. *Chem. Eng. Sci.* **1989**, *44* (3), 777–779. https://doi.org/10.1016/0009-2509(89)85053-5.

(43) Currie, J. A. Gaseous Diffusion in Porous Media. Part 2. - Dry Granular Materials. *Br. J. Appl. Phys.* **1960**, *11* (8), 318–324. https://doi.org/10.1088/0508-3443/11/8/303.

(44) Klinkenberg, L. J. Analog Between Diffusion and Electrical Conductivity in Porous Rocks. *Geol. Soc. Am. Bull. 62.6* **1951**, 559–564.

(45) Grane, F. Measurements of Transverse Dispersion in Granular Media. *J. Chem. Eng. Data* **1961**, *6* (2), 283–287. https://doi.org/10.1021/je60010a031.

(46) Li, Z.; Dong, M. Experimental Study of Diffusive Tortuosity of Liquid-Saturated Consolidated Porous Media. *Ind. Eng. Chem. Res.* **2010**, *49* (13), 6231–6237. https://doi.org/10.1021/ie901765d.

(47) Liu, S.; Masliyah, J. Dispersion in Porous Media. In *Handbook of Porous Media, Second Edition*; CRC Press, 2005; Vol. 7, pp 81–140. https://doi.org/10.1201/9780415876384.ch3.

(48) Rose, D. A. Some Aspects of the Hydrodynamic Dispersion of Solutes in Porous Materials. *J. Soil Sci.* **1973**, *24* (3).

(49) Tandon, P.; Rosner, D. E. Translational Brownian Diffusion Coefficient of Large (Multiparticle) Suspended Aggregates. *Ind. Eng. Chem. Res.* **1995**, *34* (10), 3265–3277. https://doi.org/10.1021/ie00037a013.

(50) Fan, D.; Chapman, E.; Khan, A.; Iacoviello, F.; Mikutis, G.; Pini, R.; Striolo, A. Anomalous Transport of Colloids in Heterogeneous Porous Media: A Multi-Scale Statistical Theory. *J. Colloid Interface Sci.* **2022**, *617*, 94–105. https://doi.org/10.1016/j.jcis.2022.02.127.

(51) Saleh, N. B.; Afrooz, A. R. M. N.; Aich, N.; Plazas-Tuttle, J. Aggregation Kinetics and Fractal Dimensions of Nanomaterials in Environmental Systems. *Eng. Nanoparticles Environ. Biophys. Process. Toxic.* **2016**, 139–159. https://doi.org/10.1002/9781119275855.ch8.

(52) Stoll, S.; Pefferkorn, E. Modes of Spontaneous and Provoked Cluster Fragmentation. I. During Diffusion-Limited Aggregation. *J. Colloid Interface Sci.* **1992**, *152* (1), 247–256. https://doi.org/10.1016/0021-9797(92)90024-G.

(53) Jiang, X.; Tong, M.; Kim, H. Influence of Natural Organic Matter on the Transport and Deposition of Zinc Oxide Nanoparticles in Saturated Porous Media. *J. Colloid Interface Sci.* **2012**, *386* (1), 34–43. https://doi.org/10.1016/j.jcis.2012.07.002.

(54) Fernandes, I. J.; Aroche, A. F.; Schuck, A.; Lamberty, P.; Peter, C. R.; Hasenkamp, W.; Rocha, T. L. A. C. Silver Nanoparticle Conductive Inks: Synthesis, Characterization, and Fabrication of Inkjet-Printed Flexible Electrodes. *Sci. Rep.* **2020**, *10* (1), 1–12. https://doi.org/10.1038/s41598-020-65698-3.

(55) Alexis, F.; Pridgen, E.; Molnar, L. K.; Farokhzad, O. C. Factors Affecting the Clearance and Biodistribution of Polymeric Nanoparticles. *Mol. Pharm.* **2008**, *5* (4), 505–515. https://doi.org/10.1021/mp800051m.

(56) Nguyen, T. X. D.; Vu, T. V.; Razavi, S.; Papavassiliou, D. V. Coarse Grained Modeling of

Multiphase Flows with Surfactants. *Polymers (Basel).* **2022**, *14* (3). https://doi.org/10.3390/polym14030543.

(57) Ehtesabi, H.; Ahadian, M. M.; Taghikhani, V.; Ghazanfari, M. H. Enhanced Heavy Oil Recovery in Sandstone Cores Using TiO 2 Nanofluids. *Energy & Fuels* **2014**, *28* (1), 423–430. https://doi.org/10.1021/ef401338c.

(58) Petosa, A. R.; Jaisi, D. P.; Quevedo, I. R.; Elimelech, M.; Tufenkji, N. Aggregation and Deposition of Engineered Nanomaterials in Aquatic Environments: Role of Physicochemical Interactions. *Environ. Sci. Technol.* **2010**, *44* (17), 6532–6549. https://doi.org/10.1021/es100598h.

(59) Hul, G.; Seijo, M.; Carnal, F.; Cornelis, G.; Stoll, S. Effect of Deposition, Detachment and Aggregation Processes on Nanoparticle Transport in Porous Media Using Monte Carlo Simulations. *Environ. Sci. Nano* **2021**, *8* (8), 2223–2234. https://doi.org/10.1039/D1EN00034A.

(60) Lv, X.; Gao, B.; Sun, Y.; Shi, X.; Xu, H.; Wu, J. Effects of Humic Acid and Solution Chemistry on the Retention and Transport of Cerium Dioxide Nanoparticles in Saturated Porous Media. *Water, Air, Soil Pollut.* **2014**, *225* (10), 2167. https://doi.org/10.1007/s11270-014-2167-7.

(61) Babakhani, P. The Impact of Nanoparticle Aggregation on Their Size Exclusion during Transport in Porous Media: One- and Three-Dimensional Modelling Investigations. *Sci. Rep.* **2019**, *9* (1). https://doi.org/10.1038/s41598-019-50493-6.

(62) Pham, O. L.; Feher, S. E.; Nguyen, Q. T.; Papavassiliou, D. V. Distribution and History of Extensional Stresses on VWF Surrogate Molecules in Turbulent Flow. *Sci. Rep.* **2022**, *12* (1), 1–14. https://doi.org/10.1038/s41598-021-04034-9.

(63) Sun, Y.; Park, C.-H.; Pichot, G.; Taron, J. *Random Walk Particle Tracking*; 2015. https://doi.org/10.1007/978-3-319-11894-9_6.

(64) Fan, D.; Pini, R.; Striolo, A. A Seemingly Universal Particle Kinetic Distribution in Porous Media. *Appl. Phys. Lett.* **2021**, *119* (13), 134101. https://doi.org/10.1063/5.0060668.

(65) Nguyen, V.; Papavassiliou, D. V. Hydrodynamic Dispersion in Porous Media and the Significance of Lagrangian Time and Space Scales. *Fluids* **2020**, *5* (2), 79. https://doi.org/10.3390/fluids5020079.

(66) Choy, C. C.; Wazne, M.; Meng, X. Application of an Empirical Transport Model to

Simulate Retention of Nanocrystalline Titanium Dioxide in Sand Columns. *Chemosphere* **2008**, *71* (9), 1794–1801. https://doi.org/10.1016/j.chemosphere.2007.12.030.

(67) Guzman, K. A. D.; Finnegan, M. P.; Banfield, J. F. Influence of Surface Potential on Aggregation and Transport of Titania Nanoparticles. *Environ. Sci. Technol.* **2006**, *40* (24), 7688–7693. https://doi.org/10.1021/es060847g.

(68) Jiang, X.; Wang, X.; Tong, M.; Kim, H. Initial Transport and Retention Behaviors of ZnO Nanoparticles in Quartz Sand Porous Media Coated with Escherichia Coli Biofilm. *Environ. Pollut.* **2013**, *174*, 38–49. https://doi.org/10.1016/j.envpol.2012.11.016.

(69) Sun, P.; Shijirbaatar, A.; Fang, J.; Owens, G.; Lin, D.; Zhang, K. Distinguishable Transport Behavior of Zinc Oxide Nanoparticles in Silica Sand and Soil Columns. *Sci. Total Environ.* **2015**, *505*, 189–198. https://doi.org/10.1016/j.scitotenv.2014.09.095.

(70) Kurlanda-Witek, H.; Ngwenya, B. T.; Butler, I. B. Transport of Bare and Capped Zinc Oxide Nanoparticles Is Dependent on Porous Medium Composition. *J. Contam. Hydrol.* **2014**, *162–163*, 17–26. https://doi.org/10.1016/j.jconhyd.2014.04.002.

(71) Wang, Q.; Lee, J.-H.; Jeong, S.-W.; Jang, A.; Lee, S.; Choi, H. Mobilization and Deposition of Iron Nano and Sub-Micrometer Particles in Porous Media: A Glass Micromodel Study. *J. Hazard. Mater.* **2011**, *192* (3), 1466–1475. https://doi.org/10.1016/j.jhazmat.2011.06.066.

(72) Wei, Y. T.; Wu, S. chee; Yang, S. W.; Che, C. H.; Lien, H. L.; Huang, D. H. Biodegradable Surfactant Stabilized Nanoscale Zero-Valent Iron for in Situ Treatment of Vinyl Chloride and 1,2-Dichloroethane. *J. Hazard. Mater.* **2012**, *211–212*, 373–380. https://doi.org/10.1016/j.jhazmat.2011.11.018.

(73) Raychoudhury, T.; Tufenkji, N.; Ghoshal, S. Aggregation and Deposition Kinetics of Carboxymethyl Cellulose-Modified Zero-Valent Iron Nanoparticles in Porous Media. *Water Res.* **2012**, *46* (6), 1735–1744. https://doi.org/10.1016/j.watres.2011.12.045.

(74) Phenrat, T.; Kim, H. J.; Fagerlund, F.; Illangasekare, T.; Lowry, G. V. Empirical Correlations to Estimate Agglomerate Size and Deposition during Injection of a Polyelectrolyte-Modified Fe0 Nanoparticle at High Particle Concentration in Saturated Sand. *J. Contam. Hydrol.* **2010**, *118* (3–4), 152–164. https://doi.org/10.1016/j.jconhyd.2010.09.002.

(75) Babakhani, P.; Fagerlund, F.; Shamsai, A.; Lowry, G. V.; Phenrat, T. Modified

MODFLOW-Based Model for Simulating the Agglomeration and Transport of Polymer-Modified Fe0 Nanoparticles in Saturated Porous Media. *Environ. Sci. Pollut. Res.* **2018**, *25* (8), 7180–7199. https://doi.org/10.1007/s11356-015-5193-0.

(76) Pham, N. H.; Papavassiliou, D. V. Hydrodynamic Effects on the Aggregation of Nanoparticles in Porous Media. *Int. J. Heat Mass Transf.* **2018**, *121*, 477–487. https://doi.org/10.1016/j.ijheatmasstransfer.2017.12.150.

(77) Taghavy, A.; Pennell, K. D.; Abriola, L. M. Modeling Coupled Nanoparticle Aggregation and Transport in Porous Media: A Lagrangian Approach. *J. Contam. Hydrol.* **2015**, *172*, 48–60. https://doi.org/10.1016/j.jconhyd.2014.10.012.

(78) Taghavy, A.; Pennell, K. D.; Abriola, L. M. Modeling Coupled Nanoparticle Aggregation and Transport in Porous Media: A Lagrangian Approach. *J. Contam. Hydrol.* **2015**, *172*, 48–60. https://doi.org/10.1016/j.jconhyd.2014.10.012.

(79) Katzourakis, V. E.; Chrysikopoulos, C. V. Modeling the Transport of Aggregating Nanoparticles in Porous Media. *Water Resour. Res.* **2021**, *57* (1). https://doi.org/10.1029/2020WR027946.

(80) Krehel, O.; Muntean, A.; Knabner, P. Multiscale Modeling of Colloidal Dynamics in Porous Media Including Aggregation and Deposition. *Adv. Water Resour.* **2015**, *86*, 209–216. https://doi.org/10.1016/j.advwatres.2015.10.005.

(81) Lee, D. Modeling Coagulation Kinetics Incorporating Fractal Theories: A Fractal Rectilinear Approach. *Water Res.* **2000**, *34* (7), 1987–2000. https://doi.org/10.1016/S0043-1354(99)00354-1.

(82) M. Elimelech, J. Gregory, X. Jia, R. A. W. *Particle Deposition and Aggregation, Measurement, Modeling and Simulation*; Kent: Elsevier Science & Technology, 1995.

(83) Saleh, N. B.; Afrooz, A. R. M. N.; Aich, N.; Plazas-Tuttle, J. Aggregation Kinetics and Fractal Dimensions of Nanomaterials in Environmental Systems. In *Engineered Nanoparticles and the Environment: Biophysicochemical Processes and Toxicity*; John Wiley & Sons, Inc.: Hoboken, NJ, USA, 2016; pp 139–159. https://doi.org/10.1002/9781119275855.ch8.

(84) Jungblut, S.; Joswig, J. O.; Eychmüller, A. Diffusion- and Reaction-Limited Cluster Aggregation Revisited. *Phys. Chem. Chem. Phys.* **2019**, *21* (10), 5723–5729. https://doi.org/10.1039/c9cp00549h.

(85) Veerapaneni, S.; Wiesner, M. R. Particle Deposition on an Infinitely Permeable Surface. *J. Colloid Interface Sci.* **1994**, *162* (1), 110–122. https://doi.org/10.1006/jcis.1994.1015.

(86) Roth, E. J.; Gilbert, B.; Mays, D. C. Colloid Deposit Morphology and Clogging in Porous Media: Fundamental Insights Through Investigation of Deposit Fractal Dimension. *Environ. Sci. Technol.* **2015**, *49* (20), 12263–12270. https://doi.org/10.1021/acs.est.5b03212.

(87) Deng, X.; Huang, Z.; Wang, W.; Davé, R. N. Investigation of Nanoparticle Agglomerates Properties Using Monte Carlo Simulations. *Adv. Powder Technol.* **2016**, *27* (5), 1971–1979. https://doi.org/10.1016/j.apt.2016.06.029.

(88) Liu, H. H.; Surawanvijit, S.; Rallo, R.; Orkoulas, G.; Cohen, Y. Analysis of Nanoparticle Agglomeration in Aqueous Suspensions via Constant-Number Monte Carlo Simulation. *Environ. Sci. Technol.* **2011**, *45* (21), 9284–9292. https://doi.org/10.1021/es202134p.

(89) Ono, K.; Matsukawa, Y.; Saito, Y.; Matsushita, Y.; Aoki, H.; Era, K.; Aoki, T.; Yamaguchi, T. Monte Carlo Simulation for Morphology of Nanoparticles and Particle Size Distributions: Comparison of the Cluster–Cluster Aggregation Model with the Sectional Method. *J. Nanoparticle Res.* **2015**, *17* (6), 242. https://doi.org/10.1007/s11051-015-3049-7.

(90) Chen, S.; Doolen, G. D. Lattice Boltzmann Method for Fluid Flows. *Annu. Rev. Fluid Mech.* **1998**, *30* (1), 329–364. https://doi.org/10.1146/annurev.fluid.30.1.329.

(91) Papavassiliou, D. V.; Pham, N. H.; Kadri, O. E.; Voronov, R. S. Lattice Boltzmann Methods for Bioengineering Applications. In *Numerical Methods and Advanced Simulation in Biomechanics and Biological Processes*; Elsevier, 2018; pp 415–429. https://doi.org/10.1016/B978-0-12-811718-7.00023-X.

(92) Mohamad, A. A. *Lattice Boltzmann Method*; Advanced Structured Materials; Springer London: London, 2011. https://doi.org/10.1007/978-0-85729-455-5.

(93) Pham, N. H.; Swatske, D. P.; Harwell, J. H.; Shiau, B.-J.; Papavassiliou, D. V. Transport of Nanoparticles and Kinetics in Packed Beds: A Numerical Approach with Lattice Boltzmann Simulations and Particle Tracking. *Int. J. Heat Mass Transf.* **2014**, *72*, 319–328. https://doi.org/10.1016/j.ijheatmasstransfer.2013.12.075.

(94) Massey, F. J. The Kolmogorov-Smirnov Test for Goodness of Fit Author. *J. Am. Stat. Assoc.* **1951**, *46* (253), 68–78. https://doi.org/10.1080/01621459.1951.10500769.

(95) Siregar, K.; Ishak, A.; Esterlita, M. Distribution Testing On The Average Room Occupancy Rate Of Hotels By Province In 2013-2017. *IOP Conf. Ser. Mater. Sci. Eng.* **2020**, *1003* (1), 012107. https://doi.org/10.1088/1757-899X/1003/1/012107.

(96) Sadeghifar, H.; Bahrami, M.; Djilali, N. A Statistically-Based Thermal Conductivity Model for Fuel Cell Gas Diffusion Layers. *J. Power Sources* **2013**, *233*, 369–379. https://doi.org/10.1016/j.jpowsour.2013.01.086.

(97) Karuppanasamy, J.; Pillai, R. G. Statistical Distributions for the Corrosion Rates of Conventional and Prestressing Steel Reinforcement Embedded in Chloride Contaminated Mortar. *Corrosion* **2017**, *73* (9), 1119–1131. https://doi.org/10.5006/2330.

(98) Goleva, R.; Stainov, R.; Wagenknecht-Dimitrova, D.; Mirtchev, S.; Atamian, D.; Mavromoustakis, C. X.; Mastorakis, G.; Dobre, C.; Savov, A.; Draganov, P. Data and Traffic Models in 5G Network. In *Internet of Things (IoT) in 5G Mobile Technologies*; Mavromoustakis, C. X., Mastorakis, G., Batalla, J. M., Eds.; Springer International Publishing: Cham, 2016; pp 485–499. https://doi.org/10.1007/978-3-319-30913-2_20.

(99) Rahimdel, M. J.; Ataei, M.; Khalokakaei, R. Reliability Analysis and Maintenance Scheduling of the Electrical System of Rotary Drilling Machines. In *Current Trends in Reliability, Availability, Maintainability and Safety*; Kumar, U., Ahmadi, A., Verma, A. K., Varde, P., Eds.; Springer International Publishing: Cham, 2016; pp 623–632. https://doi.org/10.1007/978-3-319-23597-4_45.

(100) Yilmaz, Ş.; Bayrak, E.; Bayrak, Y. Comparision of the Different Probability Distributions for Earthquake Hazard Assessment in the North Anatolian Fault Zone. In *AIP Conference Proceedings*; 2016; Vol. 1726, p 020003. https://doi.org/10.1063/1.4945829.

(101) Sadeghi, S. H.; Zabihi, M.; Vafakhah, M.; Hazbavi, Z. Spatiotemporal Mapping of Rainfall Erosivity Index for Different Return Periods in Iran. *Nat. Hazards* **2017**, *87* (1), 35–56. https://doi.org/10.1007/s11069-017-2752-3.

(102) Martin-Vide, J.; Moreno-Garcia, M. C. Probability Values for the Intensity of Barcelona's Urban Heat Island (Spain). *Atmos. Res.* **2020**, *240* (October 2019), 104877. https://doi.org/10.1016/j.atmosres.2020.104877.

(103) Csabay, M.; Stehlikova, B. Firm Size Distribution and the Effects of Ownership Type. *J. Compet.* **2020**, *12* (4), 22–38. https://doi.org/10.7441/joc.2020.04.02.

(104) Filó, T. G. S.; Bigonha, M. A. S.; Ferreira, K. A. M. Statistical Dataset on Software Metrics

in Object-Oriented Systems. *ACM SIGSOFT Softw. Eng. Notes* **2014**, *39* (5), 1–6. https://doi.org/10.1145/2659118.2659130.

(105) Rabbani, A.; Ayatollahi, S.; Kharrat, R.; Dashti, N. Estimation of 3-D Pore Network Coordination Number of Rocks from Watershed Segmentation of a Single 2-D Image. *Adv. Water Resour.* **2016**, *94*, 264–277. https://doi.org/10.1016/j.advwatres.2016.05.020.

(106) Rabbani, A.; Jamshidi, S.; Salehi, S. An Automated Simple Algorithm for Realistic Pore Network Extraction from Micro-Tomography Images. *J. Pet. Sci. Eng.* **2014**, *123*, 164–171. https://doi.org/10.1016/j.petrol.2014.08.020.

(107) Baranau, V.; Tallarek, U. Random-Close Packing Limits for Monodisperse and Polydisperse Hard Spheres. *Soft Matter* **2014**, *10* (21), 3826. https://doi.org/10.1039/c3sm52959b.

(108) Baranau, V.; Hlushkou, D.; Khirevich, S.; Tallarek, U. Pore-Size Entropy of Random Hard-Sphere Packings. *Soft Matter* **2013**, *9* (12), 3361. https://doi.org/10.1039/c3sm27374a.

(109) Skoge, M.; Donev, A.; Stillinger, F. H.; Torquato, S. Packing Hyperspheres in High-Dimensional Euclidean Spaces. *Phys. Rev. E* **2006**, *74* (4), 041127. https://doi.org/10.1103/PhysRevE.74.041127.

(110) Lubachevsky, B. D. How to Simulate Billiards and Similar Systems. *J. Comput. Phys.* **1991**, *94* (2), 255–283. https://doi.org/10.1016/0021-9991(91)90222-7.

(111) Lubachevsky, B. D.; Stillinger, F. H. Geometric Properties of Random Disk Packings. *J. Stat. Phys.* **1990**, *60* (5–6), 561–583. https://doi.org/10.1007/BF01025983.

(112) Shambaugh, R. L. A Macroscopic View of the Melt-Blowing Process for Producing Microfibers. *Ind. Eng. Chem. Res.* **1988**, *27* (12), 2363–2372. https://doi.org/10.1021/ie00084a021.

(113) Zhang, D.; Bhat, G.; Malkan, S.; Wadsworth, L. Structure and Properties of Polypropylene Filaments in a Spunbonding Process. *J. Therm. Anal.* **1997**, *49* (1), 161–167. https://doi.org/10.1007/BF01987435.

(114) VanGordon, S. B.; Voronov, R. S.; Blue, T. B.; Shambaugh, R. L.; Papavassiliou, D. V.; Sikavitsas, V. I. Effects of Scaffold Architecture on Preosteoblastic Cultures under Continuous Fluid Shear. *Ind. Eng. Chem. Res.* **2011**, *50* (2), 620–629. https://doi.org/10.1021/ie902041v.

(115) Voronov, R.; VanGordon, S.; Sikavitsas, V. I.; Papavassiliou, D. V. Computational

Modeling of Flow-Induced Shear Stresses within 3D Salt-Leached Porous Scaffolds Imaged via Micro-CT. *J. Biomech.* **2010**, *43* (7), 1279–1286. https://doi.org/10.1016/j.jbiomech.2010.01.007.

(116) Thibodeaux, T. W.; Sheng, Q.; Thompson, K. E. Rapid Estimation of Essential Porous Media Properties Using Image-Based Pore-Scale Network Modeling. *Ind. Eng. Chem. Res.* **2015**, *54* (16), 4474–4486. https://doi.org/10.1021/ie503981k.

(117) Bear, J. *Dynamics of Fluids in Porous Media*; Courier Dover Publications, 1972.

(118) Bijeljic, B.; Raeini, A.; Mostaghimi, P.; Blunt, M. J. Predictions of Non-Fickian Solute Transport in Different Classes of Porous Media Using Direct Simulation on Pore-Scale Images. *Phys. Rev. E* **2013**, *87* (1), 013011. https://doi.org/10.1103/PhysRevE.87.013011.

(119) Alhashmi, Z.; Blunt, M. J.; Bijeljic, B. The Impact of Pore Structure Heterogeneity, Transport, and Reaction Conditions on Fluid–Fluid Reaction Rate Studied on Images of Pore Space. *Transp. Porous Media* **2016**, *115* (2), 215–237. https://doi.org/10.1007/s11242-016-0758-z.

(120) Dong, H. Micro-Ct Imaging and Pore Network Extraction a Dissertation Submitted To the Department of Earth Science and Engineering of Imperial College Lodon in Partial Fulfilment of the Requirements for the Degree Of, Imperial College London, 2007.

(121) Hesamian, G.; Chachi, J. Two-Sample Kolmogorov–Smirnov Fuzzy Test for Fuzzy Random Variables. *Stat. Pap.* **2015**, *56* (1), 61–82. https://doi.org/10.1007/s00362-013-0566-2.

(122) Wilcox, R. Comparing Two Groups. In *Introduction to Robust Estimation and Hypothesis Testing*; Elsevier, 2012; pp 137–213. https://doi.org/10.1016/B978-0-12-386983-8.00005-6.

(123) Hodges, J. L. The Significance Probability of the Smirnov Two-Sample Test. *Ark. för Mat.* **1958**, *3* (5), 469–486. https://doi.org/10.1007/BF02589501.

(124) Leslie, J.; Gibbons, J. D. Nonparametric Statistical Inference. *J. R. Stat. Soc. Ser. A* **1986**, *149* (3), 275. https://doi.org/10.2307/2981565.

(125) Muljadi, B. P.; Blunt, M. J.; Raeini, A. Q.; Bijeljic, B. The Impact of Porous Media Heterogeneity on Non-Darcy Flow Behaviour from Pore-Scale Simulation. *Adv. Water Resour.* **2016**, *95*, 329–340. https://doi.org/10.1016/j.advwatres.2015.05.019.

(126) Pham, N. H.; Papavassiliou, D. V. Nanoparticle Transport in Heterogeneous Porous Media

with Particle Tracking Numerical Methods. *Comput. Part. Mech.* **2017**, *4* (1), 87–100. https://doi.org/10.1007/s40571-016-0130-7.

(127) Voronov, R. Local Fluid Stress and Nutrient Transport Effects via Simulations of Perfusion through Bone Tissue Engineering Scaffolds, The University of Oklahoma, 2010.

(128) Bird, R.B., Stewart, W. E. *Transport Phenomena*; J. Wiley, New York, 2002.

(129) Chapman, A. M.; Higdon, J. J. L. Oscillatory Stokes Flow in Periodic Porous Media. *Phys. Fluids A* **1992**, *4* (10), 2099–2116. https://doi.org/10.1063/1.858507.

(130) Eshghinejadfard, A.; Daróczy, L.; Janiga, G.; Thévenin, D. Calculation of the Permeability in Porous Media Using the Lattice Boltzmann Method. *Int. J. Heat Fluid Flow* **2016**, *62*, 93–103. https://doi.org/10.1016/j.ijheatfluidflow.2016.05.010.

(131) Carrel, M.; Morales, V. L.; Dentz, M.; Derlon, N.; Morgenroth, E.; Holzner, M. Pore-Scale Hydrodynamics in a Progressively Bioclogged Three-Dimensional Porous Medium: 3-D Particle Tracking Experiments and Stochastic Transport Modeling. *Water Resour. Res.* **2018**, *54* (3), 2183–2198. https://doi.org/10.1002/2017WR021726.

(132) Holzner, M.; Morales, V. L.; Willmann, M.; Dentz, M. Intermittent Lagrangian Velocities and Accelerations in Three-Dimensional Porous Medium Flow. *Phys. Rev. E* **2015**, *92* (1), 013015. https://doi.org/10.1103/PhysRevE.92.013015.

(133) Meyer, F. Topographic Distance and Watershed Lines. *Signal Processing* **1994**, *38* (1), 113–125. https://doi.org/10.1016/0165-1684(94)90060-4.

(134) Gerke, K. M.; Sizonenko, T. O.; Karsanina, M. V.; Lavrukhin, E. V.; Abashkin, V. V.; Korost, D. V. Improving Watershed-Based Pore-Network Extraction Method Using Maximum Inscribed Ball Pore-Body Positioning. *Adv. Water Resour.* **2020**, *140* (January 2019), 103576. https://doi.org/10.1016/j.advwatres.2020.103576.

(135) Dong, H.; Blunt, M. J. Pore-Network Extraction from Micro-Computerized-Tomography Images. *Phys. Rev. E* **2009**, *80* (3), 036307. https://doi.org/10.1103/PhysRevE.80.036307.

(136) Raeini, A. Q.; Bijeljic, B.; Blunt, M. J. Generalized Network Modeling: Network Extraction as a Coarse-Scale Discretization of the Void Space of Porous Media. *Phys. Rev. E* **2017**, *96* (1), 013312. https://doi.org/10.1103/PhysRevE.96.013312.

(137) Silin, D.; Patzek, T. Pore Space Morphology Analysis Using Maximal Inscribed Spheres. *Phys. A Stat. Mech. its Appl.* **2006**, *371* (2), 336–360. https://doi.org/10.1016/j.physa.2006.04.048.

(138) Arand, F.; Hesser, J. Accurate and Efficient Maximal Ball Algorithm for Pore Network Extraction. *Comput. Geosci.* **2017**, *101* (October 2016), 28–37. https://doi.org/10.1016/j.cageo.2017.01.004.

(139) Voronov, R. S.; VanGordon, S. B.; Sikavitsas, V. I.; Papavassiliou, D. V. Efficient Lagrangian Scalar Tracking Method for Reactive Local Mass Transport Simulation through Porous Media. *Int. J. Numer. Methods Fluids* **2011**, *67* (4), 501–517. https://doi.org/10.1002/fld.2369.

(140) G.I. Taylor. Diffusion by Continuous Movements. *Proc. Lond. Math. Soc. 24A 196-212*.

(141) Saffman, P. G. On the Effect of the Molecular Diffusivity in Turbulent Diffusion. *J. Fluid Mech.* **1960**, *8* (2), 273–283. https://doi.org/10.1017/S0022112060000591.

(142) Srinivasan, C.; Papavassiliou, D. V. Backwards and Forwards Dispersion of a Scalar in Turbulent Wall Flows. *Int. J. Heat Mass Transf.* **2010**, *53* (5–6), 1023–1035. https://doi.org/10.1016/j.ijheatmasstransfer.2009.11.008.

(143) Le, P. M.; Papavassiliou, D. V. Turbulent Dispersion from Elevated Line Sources in Channel and Couette Flow. *AIChE J.* **2005**, *51* (9), 2402–2414. https://doi.org/10.1002/aic.10507.

(144) Mito, Y.; Hanratty, T. J. Use of a Modified Langevin Equation to Describe Turbulent Dispersion of Fluid Particles in a Channel Flow. *Flow, Turbul. Combust.* **2002**, *68* (1), 1–26. https://doi.org/10.1023/A:1015614823809.

(145) Luo, J. P.; Lu, Z. M.; Liu, Y. L. Lagrangian Time Scales and Its Relationship to Eulerian Equivalents in Turbulent Channel Flow. *J. Shanghai Univ.* **2010**, *14* (1), 71–75. https://doi.org/10.1007/s11741-010-0114-1.

(146) Luo, J.; Ushijima, T.; Kitoh, O.; Lu, Z.; Liu, Y. Lagrangian Dispersion in Turbulent Channel Flow and Its Relationship to Eulerian Statistics. *Int. J. Heat Fluid Flow* **2007**, *28* (5), 871–881. https://doi.org/10.1016/j.ijheatfluidflow.2007.02.008.

(147) Manz, B.; Gladden, L. F.; Warren, P. B. Flow and Dispersion in Porous Media: Lattice-Boltzmann and N M R Studies. *AIChE J.* **1999**, *45* (9), 1845–1854. https://doi.org/10.1002/aic.690450902.

(148) Li, K.; Zhang, W.; Huang, Y.; Chen, Y. Aggregation Kinetics of CeO2 Nanoparticles in KCl and CaCl2 Solutions: Measurements and Modeling. *J. Nanoparticle Res.* **2011**, *13* (12), 6483–6491. https://doi.org/10.1007/s11051-011-0548-z.

(149) Zhang, W. Characterizing , Imaging , and Quantifying the Environmental Behavior and Biological Interactions of Metal-Based Nanoparticles, 2011.

(150) Karimian, H.; Babaluo, A. A. Halos Mechanism in Stabilizing of Colloidal Suspensions: Nanoparticle Weight Fraction and PH Effects. *J. Eur. Ceram. Soc.* **2007**, *27* (1), 19–25. https://doi.org/10.1016/j.jeurceramsoc.2006.05.109.

(151) Fan and Zhu. *Principles of Gas-Solid Flows*; Cambridge University Press, Ed.; Cambridge University Press, 1998.

(152) Dong, S.; Zheng, L.; Zhang, X.; Wu, S.; Shen, B. A New Model for Brownian Force and the Application to Simulating Nanofluid Flow. *Microfluid. Nanofluidics* **2014**, *16* (1–2), 131–139. https://doi.org/10.1007/s10404-013-1213-x.

(153) Llamas, M.; Giner, V.; Sancho, M. The Dynamic Evolution of Cell Chaining in a Biological Suspension Induced by an Electrical Field. *J. Phys. D. Appl. Phys.* **1998**, *31* (21), 3160–3167. https://doi.org/10.1088/0022-3727/31/21/023.

(154) Phenrat, T.; Saleh, N.; Sirk, K.; Tilton, R. D.; Lowry, G. V. Aggregation and Sedimentation of Aqueous Nanoscale Zerovalent Iron Dispersions. *Environ. Sci. Technol.* **2007**, *41* (1), 284–290. https://doi.org/10.1021/es061349a.

(155) He, Y. T.; Wan, J.; Tokunaga, T. Kinetic Stability of Hematite Nanoparticles: The Effect of Particle Sizes. *J. Nanoparticle Res.* **2008**, *10* (2), 321–332. https://doi.org/10.1007/s11051-007-9255-1.

(156) Stebounova, L. V.; Guio, E.; Grassian, V. H. Silver Nanoparticles in Simulated Biological Media: A Study of Aggregation, Sedimentation, and Dissolution. *J. Nanoparticle Res.* **2011**, *13* (1), 233–244. https://doi.org/10.1007/s11051-010-0022-3.

(157) D. C. Rapaort. Simulating Simple Systems. In *The Art of Molecular Dynamics Simulation*; Cambridge University Press, 2004; pp 44–82. https://doi.org/10.1017/CBO9780511816581.006.

(158) Raper, J. A.; Amal, R. Measurement of Aggregate Fractal Dimensions Using Static Light Scattering. *Part. Part. Syst. Charact.* **1993**, *10* (5), 239–245. https://doi.org/10.1002/ppsc.19930100505.

(159) Sorensen, C. M. The Mobility of Fractal Aggregates: A Review. *Aerosol Sci. Technol.* **2011**, *45* (7), 765–779. https://doi.org/10.1080/02786826.2011.560909.

(160) Kätzel, U.; Bedrich, R.; Stintz, M.; Ketzmerick, R.; Gottschalk-Gaudig, T.; Barthel, H.

Dynamic Light Scattering for the Characterization of Polydisperse Fractal Systems: I. Simulation of the Diffusional Behavior. *Part. Part. Syst. Charact.* **2008**, *25* (1), 9–18. https://doi.org/10.1002/ppsc.200700004.

(161) Lattuada, M.; Wu, H.; Morbidelli, M. Hydrodynamic Radius of Fractal Clusters. *J. Colloid Interface Sci.* **2003**, *268* (1), 96–105. https://doi.org/10.1016/j.jcis.2003.07.028.

(162) Hess, W.; Frisch, H. L.; Klein, R. On the Hydrodynamic Behavior of Colloidal Aggregates. *Zeitschrift fur Phys. B Condens. Matter* **1986**, *64* (1), 65–67. https://doi.org/10.1007/BF01313690.

(163) Riseman, J.; Kirkwood, J. G. The Intrinsic Viscosity, Translational and Rotatory Diffusion Constants of Rod-Like Macromolecules in Solution. *J. Chem. Phys.* **1950**, *18* (4), 512–516. https://doi.org/10.1063/1.1747672.

(164) Kirkwood, J. G.; Riseman, J. The Intrinsic Viscosities and Diffusion Constants of Flexible Macromolecules in Solution. *J. Chem. Phys.* **1948**, *16* (6), 565–573. https://doi.org/10.1063/1.1746947.

(165) Striolo, A. On the Solution Self-Assembly of Nanocolloidal Brushes: Insights from Simulations. *Nanotechnology* **2008**, *19* (44), 445606. https://doi.org/10.1088/0957-4484/19/44/445606.

(166) Nguyen, Q.; Feher, S.; Papavassiliou, D. Lagrangian Modeling of Turbulent Dispersion from Instantaneous Point Sources at the Center of a Turbulent Flow Channel. *Fluids* **2017**, *2* (3), 46. https://doi.org/10.3390/fluids2030046.

(167) Rudnick, J.; Gaspari, G. The Shapes of Random Walks. *Science (80-.).* **1987**, *237* (4813), 384–389. https://doi.org/10.1126/science.237.4813.384.

(168) Gupta, S.; Biswas, P. Effect of PH on Size and Internal Structure of Poly(Propylene Imine) Dendrimers: A Molecular Dynamics Simulation Study. *J. Phys. Chem. B* **2018**, *122* (39), 9250–9263. https://doi.org/10.1021/acs.jpcb.8b04653.

(169) Nguyen, Q.; Papavassiliou, D. V. A Statistical Model to Predict Streamwise Turbulent Dispersion from the Wall at Small Times. *Phys. Fluids* **2016**, *28* (12), 125103. https://doi.org/10.1063/1.4968182.

(170) Justus, C. G.; Hargraves, W. R.; Mikhail, A.; Graber, D. Methods for Estimating Wind Speed Frequency Distributions. *J. Appl. Meteorol.* **1978**, *17* (3), 350–353. https://doi.org/10.1175/1520-0450(1978)017<0350:MFEWSF>2.0.CO;2.

(171) Tuller, S. E.; Brett, A. C. The Characteristics of Wind Velocity That Favor the Fitting of a Weibull Distribution in Wind Speed Analysis. *J. Clim. Appl. Meteorol.* **1984**, *23* (1), 124–134. https://doi.org/10.1175/1520-0450(1984)023<0124:TCOWVT>2.0.CO;2.

(172) Lai, C.-D. *Generalized Weibull Distributions (SpringerBriefs in Statistics)*; 2013.

(173) Akdağ, S. A.; Güler, Ö. Calculation of Wind Energy Potential and Economic Analysis by Using Weibull Distribution—A Case Study from Turkey. Part 1: Determination of Weibull Parameters. *Energy Sources, Part B Econ. Planning, Policy* **2009**, *4* (1), 1–8. https://doi.org/10.1080/15567240802532841.

(174) Yeh, T. H.; Wang, L. A Study on Generator Capacity for Wind Turbines under Various Tower Heights and Rated Wind Speeds Using Weibull Distribution. *IEEE Trans. Energy Convers.* **2008**, *23* (2), 592–602. https://doi.org/10.1109/TEC.2008.918626.

(175) Nguyen, V. T.; Papavassiliou, D. V. Velocity Magnitude Distribution for Flow in Porous Media. *Ind. Eng. Chem. Res.* **2021**, *60* (38), 13979–13990. https://doi.org/10.1021/acs.iecr.1c02474.

(176) Shewhart, W. A.; Wilks, S. S.; Cressie, N. A. C.; Fisher, N. I.; Johnstone, I. M.; Kadane, J. B.; Scott, D. W.; Silverman, B. W.; Smith, A. F. M.; Teugels, J.; Barnett, V.; Bradley, R. A.; Hunter, J. S.; Kendall, D. G. *An Introduction to Probability and Statistics*; 2000.

(177) Berger, V. W.; Zhou, Y. Kolmogorov–Smirnov Test: Overview. In *Wiley StatsRef: Statistics Reference Online*; Wiley, 2014; pp 1–5. https://doi.org/10.1002/9781118445112.stat06558.

(178) Massey, F. J. The Kolmogorov-Smirnov Test for Goodness of Fit. *J. Am. Stat. Assoc.* **1951**, *46* (253), 68. https://doi.org/10.2307/2280095.

(179) Press, C.; Society, T. A. Distribution of the Bay Checkerspot Butterfly , Euphydryas Editha Bayensis : Evidence for a Metapopulation Model Author (s): Susan Harrison , Dennis D . Murphy , Paul R . Ehrlich Reviewed Work (s): Source : The American Naturalist , Vol . 132 , No . 3. **2012**, *132* (3), 360–382.

(180) De Meyer, F.; Capel-Boute, C. Statistical Analysis of Piccardi Chemical Tests. *Int. J. Biometeorol.* **1987**, *31* (4), 301–322. https://doi.org/10.1007/BF02188942.

(181) Voronov, R. S.; VanGordon, S. B.; Sikavitsas, V. I.; Papavassiliou, D. V. Distribution of Flow-Induced Stresses in Highly Porous Media. *Appl. Phys. Lett.* **2010**, *97* (2), 024101. https://doi.org/10.1063/1.3462071.

(182) Rabbani, A.; Babaei, M. Hybrid Pore-Network and Lattice-Boltzmann Permeability Modelling Accelerated by Machine Learning. *Adv. Water Resour.* **2019**, *126* (February), 116–128. https://doi.org/10.1016/j.advwatres.2019.02.012.

(183) Ibrahim, H. M.; Awad, M.; Al-Farraj, A. S.; Al-Turki, A. M. Effect of Flow Rate and Particle Concentration on the Transport and Deposition of Bare and Stabilized Zero-Valent Iron Nanoparticles in Sandy Soil. *Sustain.* **2019**, *11* (23), 1–13. https://doi.org/10.3390/su11236608.

(184) Turetta, L.; Lattuada, M. The Role of Hydrodynamic Interactions on the Aggregation Kinetics of Sedimenting Colloidal Particles. *Soft Matter* **2022**, *18* (8), 1715–1730. https://doi.org/10.1039/d1sm01637g.

(185) Chowdhury, I.; Walker, S. L.; Mylon, S. E. Aggregate Morphology of Nano-TiO2: Role of Primary Particle Size, Solution Chemistry, and Organic Matter. *Environ. Sci. Process. Impacts* **2013**, *15* (1), 275–282. https://doi.org/10.1039/c2em30680h.

(186) Sun, H.; Jiao, R.; Xu, H.; An, G.; Wang, D. The Influence of Particle Size and Concentration Combined with PH on Coagulation Mechanisms. *J. Environ. Sci. (China)* **2019**, *82*, 39–46. https://doi.org/10.1016/j.jes.2019.02.021.

(187) Karimian, H.; Babaluo, A. A. Halos Mechanism in Stabilizing of Colloidal Suspensions: Nanoparticle Weight Fraction and PH Effects. *J. Eur. Ceram. Soc.* **2007**, *27* (1), 19–25. https://doi.org/10.1016/j.jeurceramsoc.2006.05.109.

(188) Nguyen, V. T.; Pham, N. H.; Papavassiliou, D. V. Relationship between Pore Fluid Velocity Distribution and Pore Size Distribution. *AIChE J.* **2022**, No. November. https://doi.org/10.1002/aic.17987.

APPENDIX

Appendix A: Hydrodynamic dispersivity based on Lagrangian Peclet number

A.1. The Grid Independence Analysis for FCC and RPS

To conduct grid independence analyses, numerical experiments to simulate the flow of water at room temperature in FCC and RPS were conducted. They all had the same domain size and pressure drop, but they had different resolutions varying from 101 × 101 × 101 to 501 × 501 × 501. The mean velocity was calculated for each run and is shown in Table A1 and Figure A1. Convergence was obtained at the resolution 201 × 201 × 201 for FCC and 401 × 401 × 401 for RPS, with a convergence tolerance of less than 0.53%. In addition to the average velocity, the full fluid velocity distribution was calculated. The range of velocities of the NPs was divided into 20 bins; then, the number of fluid nodes and the percent in each bin were calculated. It was found that there was no significant difference in the velocity distribution of the two LBM runs in the FCC that had the same average pore velocity (1000 μm/s) but different resolutions (201 × 201 × 201 and 501 × 501 × 501), as shown in Figure A2a. Similarly, the velocity distribution profiles for the two LBM runs in the RPS that had the resolutions 201 × 201 × 201 and 501 × 501 × 501 were almost identical, as demonstrated in Figure A2b. Hence, we accept that the chosen resolutions for FCC (201 × 201 × 201) and RPS (401 × 401 × 401) could provide results with acceptable accuracy.

Table A1. The effect of the number of mesh resolution on the mean velocity of the LBM flow field for FCC and RPS.

Domain Resolution	Number of Grid Points	FCC Mean Velocity (μm/s)	Error (%) Compared to (501 × 501 × 501)	RS Mean Velocity (μm/s)	Error (%) Compared to (501 × 501 × 501)
101 × 101 × 101	1,030,301	502.340	0.972%	478.762	6.376%
201 × 201 × 201	**8,120,601**	**500.130**	**0.528%**	500.174	2.189%
301 × 301 × 301	27,270,901	497.880	0.075%	505.520	1.143%
401 × 401 × 401	64,481,201	497.540	0.007%	**508.920**	**0.478%**
501 × 501 × 501	125,751,501	497.505	0.000	511.367	0.000

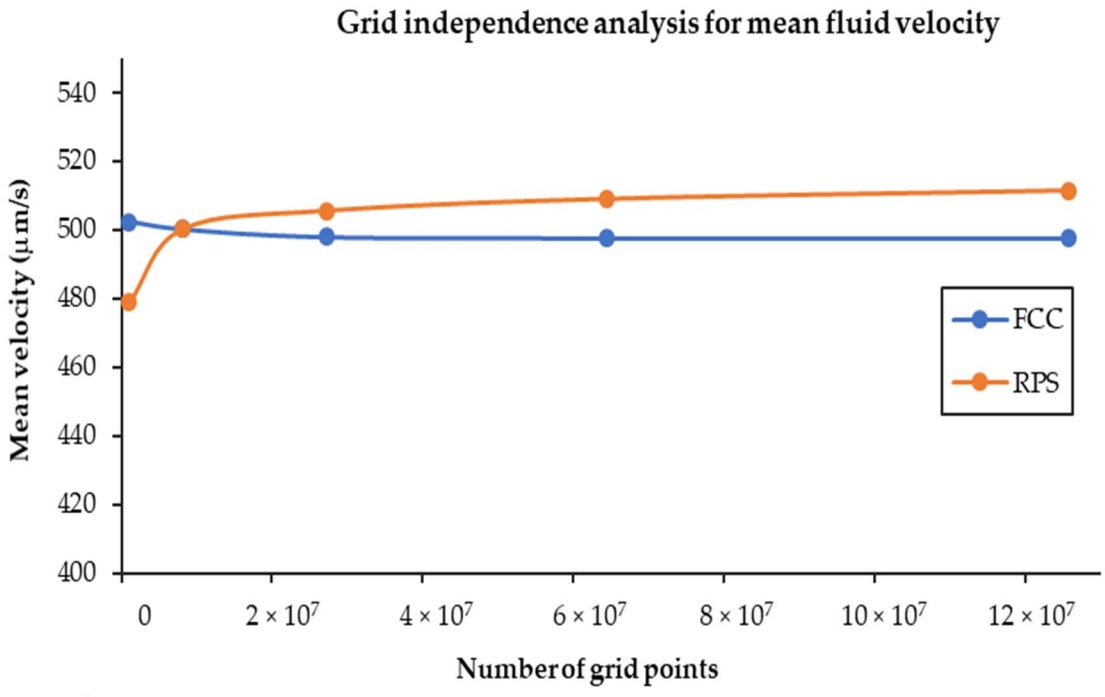
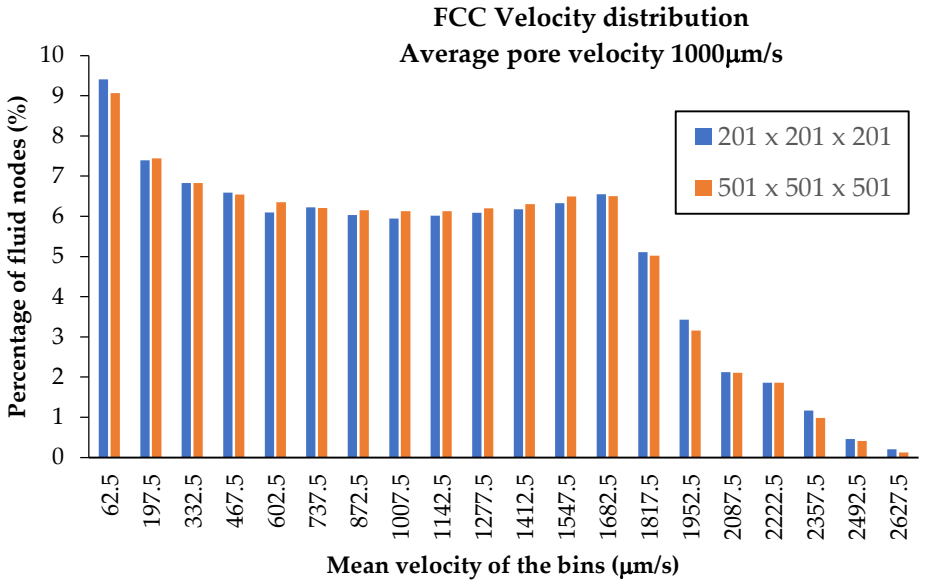
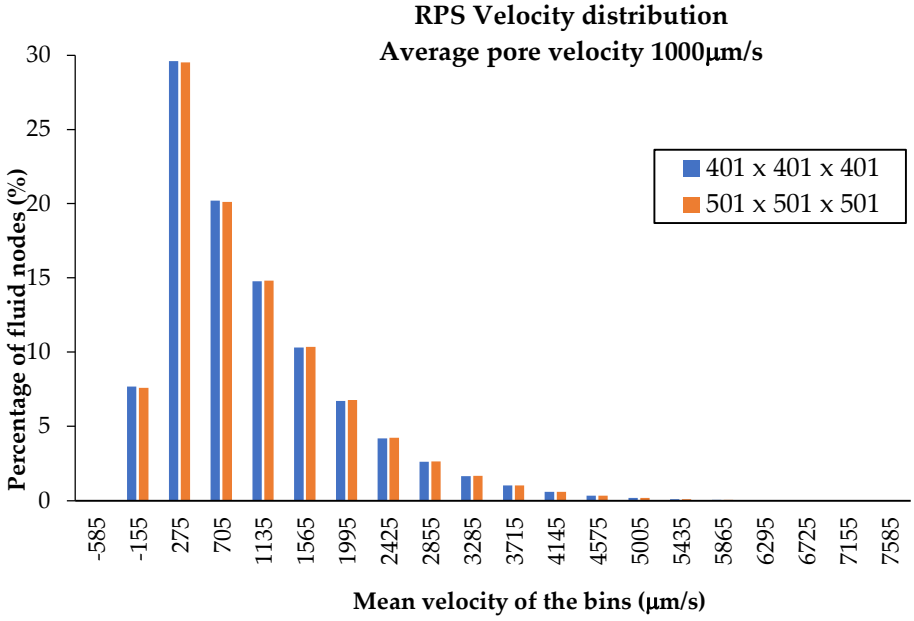


Figure A1. The effect of the number of mesh points on the accuracy of the mean fluid velocity of the LBM flow field for FCC and RPS.



(**a**)



(**b**)

Figure A2. The velocity distribution profiles for the flow fields in (a) FCC domains with resolutions of 201 × 201 × 201 and 501 × 501 × 501 and (b) RPS domains with resolutions of 401 × 401 × 401 and 501 × 501 × 501. The x-axis shows the mean velocity of the bins, while the y-axis shows the percent of the fluid nodes with the velocity in the range of the corresponding bin.

Table A.2. Summary of the Results Related to the ratio of the Hydrodynamic Dispersion Coefficient over the Effective Molecular Diffusion Coefficient together with Eulerian and Lagrangian Peclet Numbers

Sc	Pore velocity, u (cm/s)	FCC				RPS			
		$Pe_m'^L$	$Pe_m'^E$	$\frac{D_L}{D_m'}$	τ^L(s)	$Pe_m'^L$	$Pe_m'^E$	$\frac{D_L}{D_m'}$	τ^L(s)
100	0.005	0.001	0.494	0.983	0.002	0.000	0.110	0.960	0.001
	0.010	0.002	0.988	0.999	0.001	0.001	0.210	1.020	0.001
	0.020	0.008	1.980	0.985	0.001	0.006	0.430	1.010	0.001
	0.050	0.048	4.940	1.010	0.001	0.031	1.090	1.030	0.001
	0.100	0.168	9.880	1.000	0.001	0.110	2.130	1.140	0.001
	0.200	0.577	19.800	1.120	0.001	0.395	4.270	1.370	0.001
	0.300	1.150	29.600	1.390	0.001	0.729	6.400	1.740	0.001
	0.400	2.000	39.500	1.710	0.001	1.130	8.530	2.110	0.000
1000	0.005	0.047	4.960	0.990	0.013	0.037	1.080	1.020	0.009
	0.010	0.168	9.930	1.010	0.012	0.118	2.130	1.120	0.008
	0.020	0.588	19.900	1.140	0.010	0.392	4.260	1.400	0.007
	0.050	3.010	49.600	2.160	0.009	1.540	10.900	2.550	0.004
	0.100	10.700	99.300	5.240	0.008	3.940	21.300	5.150	0.003
	0.200	35.900	199.000	16.500	0.006	10.400	42.600	12.300	0.002
	0.300	77.800	298.000	32.900	0.006	17.100	63.900	21.700	0.001
	0.400	119.000	397.000	53.500	0.005	28.700	85.300	31.800	0.001
7080	0.005	1.560	35.500	1.630	0.062	0.904	7.470	1.910	0.033
	0.010	5.590	70.900	3.280	0.056	2.380	14.700	3.390	0.023
	0.020	19.700	142.000	9.190	0.049	5.980	29.400	7.770	0.014
	0.050	102.000	355.000	43.700	0.041	23.300	74.700	26.200	0.009
	0.100	332.000	709.000	145.000	0.033	59.500	147.000	67.300	0.006
	0.200	1180.000	1420.000	486.000	0.029	156.000	293.000	169.000	0.004
	0.300	2350.000	2130.000	1010.000	0.026	248.000	440.000	282.000	0.003
	0.400	3860.000	2840.000	1680.000	0.024	364.000	587.000	411.000	0.002
10000	0.005	3.070	50.400	2.170	0.086	1.260	10.900	2.550	0.032
	0.010	10.400	101.000	5.260	0.073	3.690	21.500	5.200	0.024
	0.020	37.500	202.000	16.500	0.066	9.860	42.900	12.500	0.016
	0.050	186.000	504.000	80.300	0.052	40.600	109.000	44.100	0.010
	0.100	638.000	1010.000	268.000	0.045	102.000	215.000	111.000	0.007
	0.200	2130.000	2020.000	924.000	0.037	241.000	429.000	272.000	0.004

0.300	4540.000	3030.000	1910.000	0.035	408.000	644.000	458.000	0.003
0.400	7500.000	4030.000	3150.000	0.033	613.000	858.000	655.000	0.003

A.2 Relationship between the hydrodynamic dispersivity and the effective Lagrangian Peclet number of various porous media.

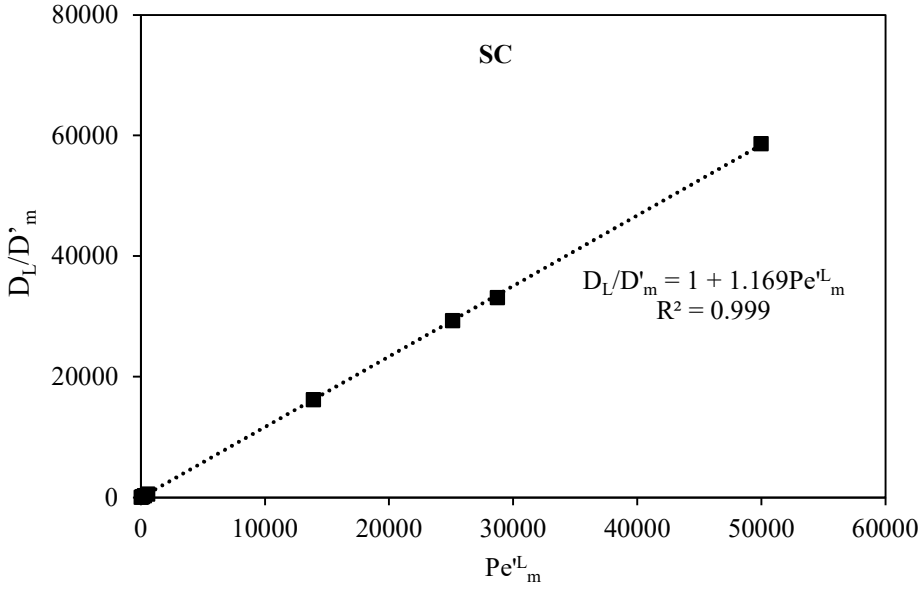


Figure A.3. The ratio of the hydrodynamic dispersion coefficient over the effective molecular diffusion coefficient in an SC as a function of the effective Peclet number determined from the Lagrangian length scale.

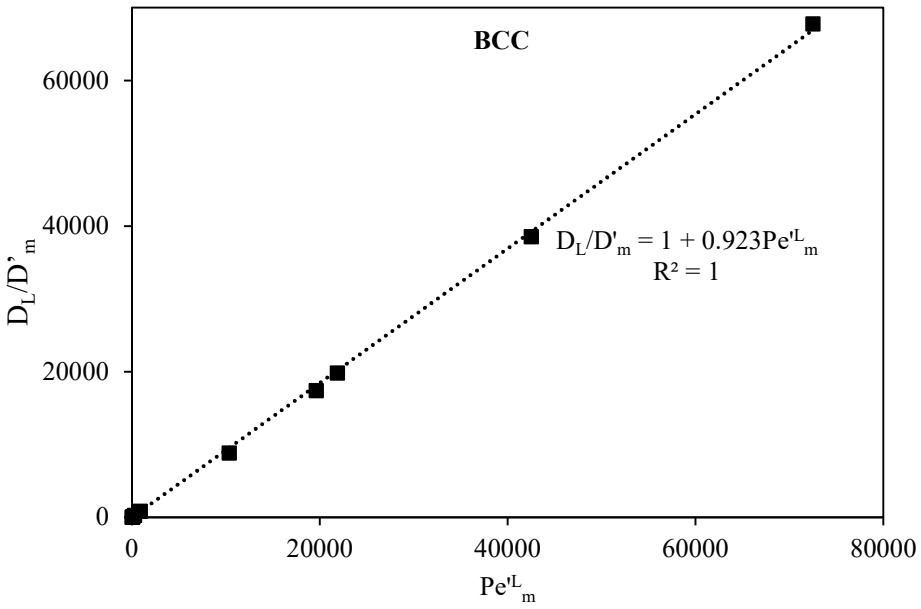


Figure A.4. The ratio of the hydrodynamic dispersion coefficient over the effective molecular diffusion coefficient in a BCC as a function of the effective Peclet number determined from the Lagrangian length scale.

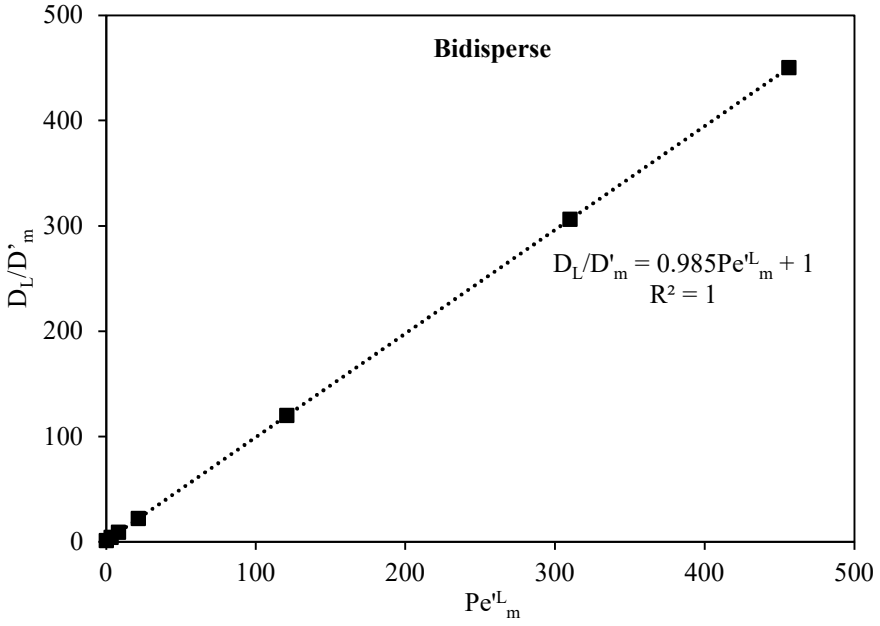


Figure A.5. The ratio of the hydrodynamic dispersion coefficient over the effective molecular diffusion coefficient in a bidisperse sphere packing as a function of the effective Peclet number determined from the Lagrangian length scale.

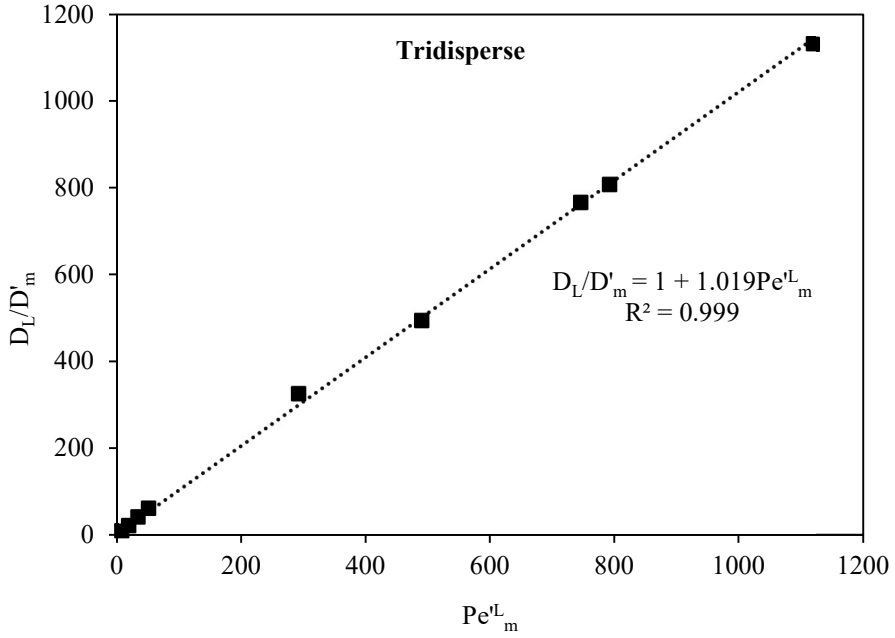


Figure A.6. The ratio of the hydrodynamic dispersion coefficient over the effective molecular diffusion coefficient in a tridisperse sphere packing as a function of the effective Peclet number determined from the Lagrangian length scale.

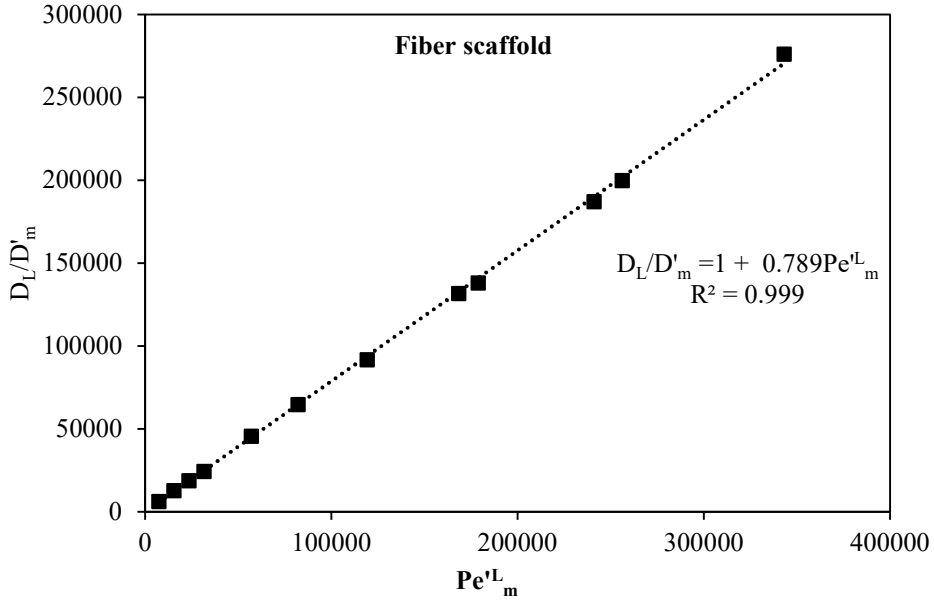


Figure A.7. The ratio of the hydrodynamic dispersion coefficient over the effective molecular diffusion coefficient in a fiber scaffold as a function of the effective Peclet number determined from the Lagrangian length scale.

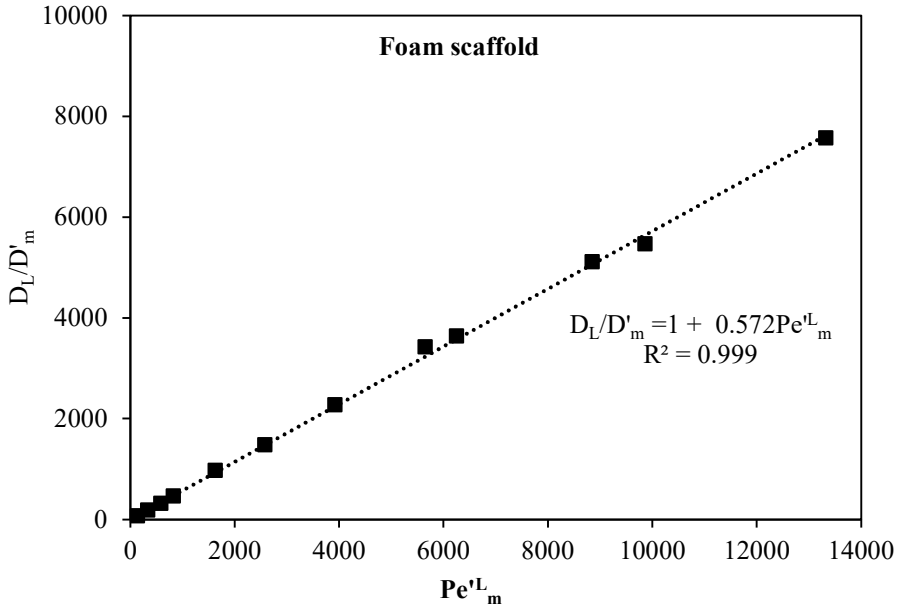


Figure A.7. The ratio of the hydrodynamic dispersion coefficient over the effective molecular diffusion coefficient in a foam scaffold as a function of the effective Peclet number determined from the Lagrangian length scale.

Appendix B: Aggregation of nanoparticles

B.1 Determining dynamic timestep

The timestep at each simulation step is estimated based on two constraints: particles in the nearest pair are not allowed to move more than one-tenth of the separation distance; and particles cannot travel more than one-fifth of the grid resolution.

As regards to the first restriction, at each simulation step, the separation distance (h) between the two nearest neighbors is computed; and the distance that a particle in the nearest pair travel is derived based on Newton's second law as follows:

$$m\frac{dV}{dt} = F_g + F_b + F_d + F_r + F_e + F_{vdW} \tag{B1}$$

By applying first-order discretization for the derivative, Eqn. B1 becomes

$$m\frac{V_2 - V_1}{\Delta t} = F_g + F_b + 3\pi\mu D(U - V_2) + \sqrt{\frac{6\pi k_B T D\mu}{\Delta t}}\xi + F_e + F_{vdW} \tag{B2}$$

where V_1 is the velocity of the particle at the previous step; and V_2 is the velocity of the particle at the current step.

Assuming $B = F_g + F_b + 3\pi\mu d_P U + F_{vdW} + F_e$ which are can be evaluated after determining the neighbors of each particle, Eqn. B2 can be written

$$V_2 = \frac{B + \sqrt{\frac{6\pi k_B T D\mu}{\Delta t}}\xi + \frac{mV_1}{\Delta t}}{\frac{m}{\Delta t} + 3\pi\mu D} \tag{B3}$$

The distance that the particle travels in three directions in Cartesian coordinate (Δs_x, Δs_y, and Δs_z) can be given as below:

$$\Delta s_x = V_{2x}\Delta t = \frac{\Delta t B_x + (\sqrt{\Delta t 6\pi k_B T D\mu}\xi)_x + mV_{1x}}{\frac{m}{\Delta t} + 3\pi\mu D}, \quad \text{(B4)}$$

$$\Delta s_y = V_{2y}\Delta t = \frac{\Delta t B_y + (\sqrt{\Delta t 6\pi k_B T D\mu}\xi)_y + mV_{1y}}{\frac{m}{\Delta t} + 3\pi\mu D}, \quad \text{(B5)}$$

$$\Delta s_z = V_{2z}\Delta t = \frac{\Delta t B_z + (\sqrt{\Delta t 6\pi k_B T D\mu}\xi)_z + mV_{1z}}{\frac{m}{\Delta t} + 3\pi\mu D} \quad \text{(B6)}$$

where V_{1x}, V_{1y}, and V_{1z} are the velocities of the particle in x, y, and z directions at the prior step; and V_{2x}, V_{2y}, and V_{2z} are the velocities of the particle in x, y, and z directions at the current step, respectively.

The distance that the particle travels is this:

$$\Delta s = \sqrt{\Delta s_x^2 + \Delta s_y^2 + \Delta s_z^2}. \quad \text{(B7)}$$

Δs cannot be determined at this stage since the timestep, Δt, is unknown. By limiting Δs of each particle to be less than one-tenth of *h,* Δt for the first constraint is found.

For the second constraint, it is assumed that the maximum velocity at the current step is not much different from that at the previous step. Δt for the second constraint can be estimated by dividing one-fifth of the grid resolution by the maximum velocity of particles in the previous simulation step. The timestep for each simulation step is the minimum of the timesteps obtained from the two restrictions.

B.2 Independence analysis of the simulation box size

Simulations related to the aggregation process of 10 mg/L CeO_2 nanoparticles in 0.2M KCl (in the bulk of an aqueous suspension) were performed with different simulation box sizes including 0.5 x 0.5 x 0.5 mm^3 (48,816 particles), 0.3 x 0.3 x 0.3mm^3 (10,544 particles), and 0.2 x

0.2 x 0.2mm^3 (3,124 particles). The aggregation kinetics and the fractal dimensions with time are shown in Figures B1a and B1b. With the box size equal to or larger than 0.2 x 0.2 x 0.2 mm^3, the results were independent of the box size or the number of particles. Thus, the simulation aggregation process of 10,544 particles in the simulation box, sized 0.3 x 0.3 x 0.3mm^3, which was used for validation, was proved to generate accurate outcomes.

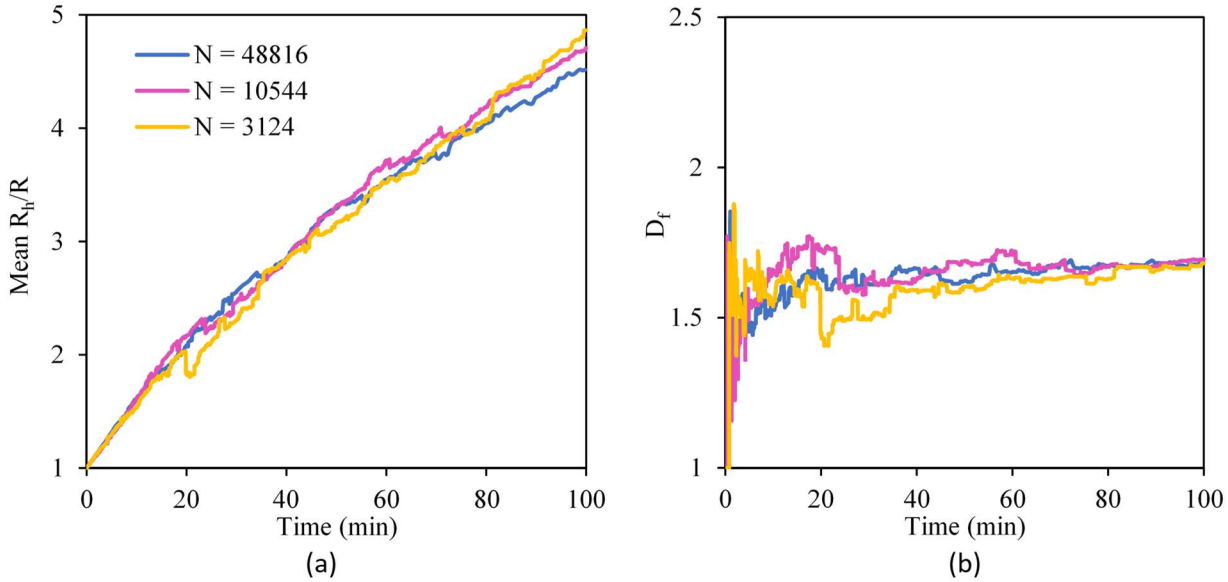


Figure B1. Aggregation kinetics (a) and fractal dimensions (b) of 10 mg/L nanoparticles CeO_2, in 0.2M KCl solution, with different simulation box sizes and different numbers of nanoparticles (48,816, 10,544, and 3,124).

B.3 Independence analysis of the user-defined freezing time

The diffusion-controlled aggregation kinetics of nanoparticles suspended in the bulk of 0.2M KCl solution is illustrated in Figure B2a. However, the simulations were performed with different algorithms. The blue line is the result obtained by not freezing any particles during the simulation. The yellow, green, and pink lines represent the kinetics and D_f achieved by freezing particles with different values of user-defined freezing time such as 0.00001s, 0.0001s, and 0.001s, respectively. As shown in Figures B2a and B2b, freezing particles with user-defined freezing time

varying from 0.00001 to 0.001s did not affect the physics of aggregation as well as the accuracy of the results.

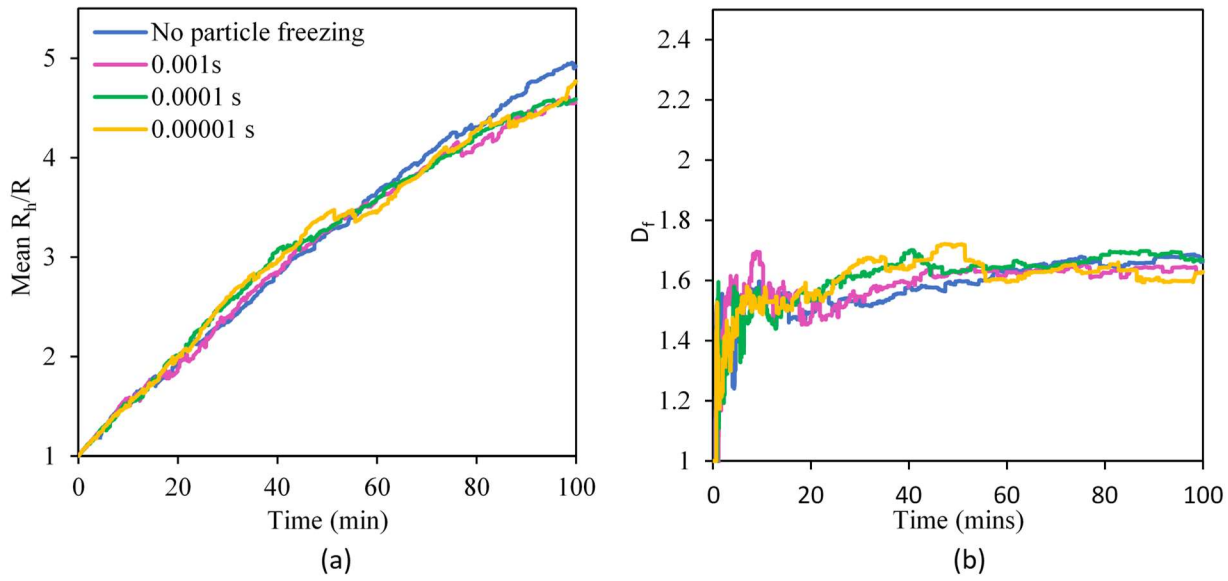


Figure B2. Aggregation kinetics (a) and fractal dimensions (b) of 10mg/L CeO_2 particles in the diffusion-limited regime (0.2M KCL) with different cases including no particles frozen, particles frozen with user-defined freezing times 0.001s, 0.0001s, and 0.00001s.

Figure B3 shows the same analysis as Figure B2 for the reaction-limited aggregation. However, in the reaction-controlled regime, when the separation distance between two particles was larger than 10nm, the van der Waals force was higher than the electrostatic force. Consequently, they attracted each other; which made the separation distance smaller and the electrostatic force become dominant. Thus, they expelled each other until their distance was larger than 10nm; and they attracted each other again. In this case, particles in the interaction pair kept moving back and forth; and the timestep for each movement was very small (~10^{-9}s). Thus, it was impossible to simulate reaction-controlled aggregation for 10 mins without freezing any particles. Hence, there was no result of the simulation without freezing non-interacting particles. As shown in Figure B3, the kinetics and fractal dimensions of simulations with different user-defined freezing times were almost the same.

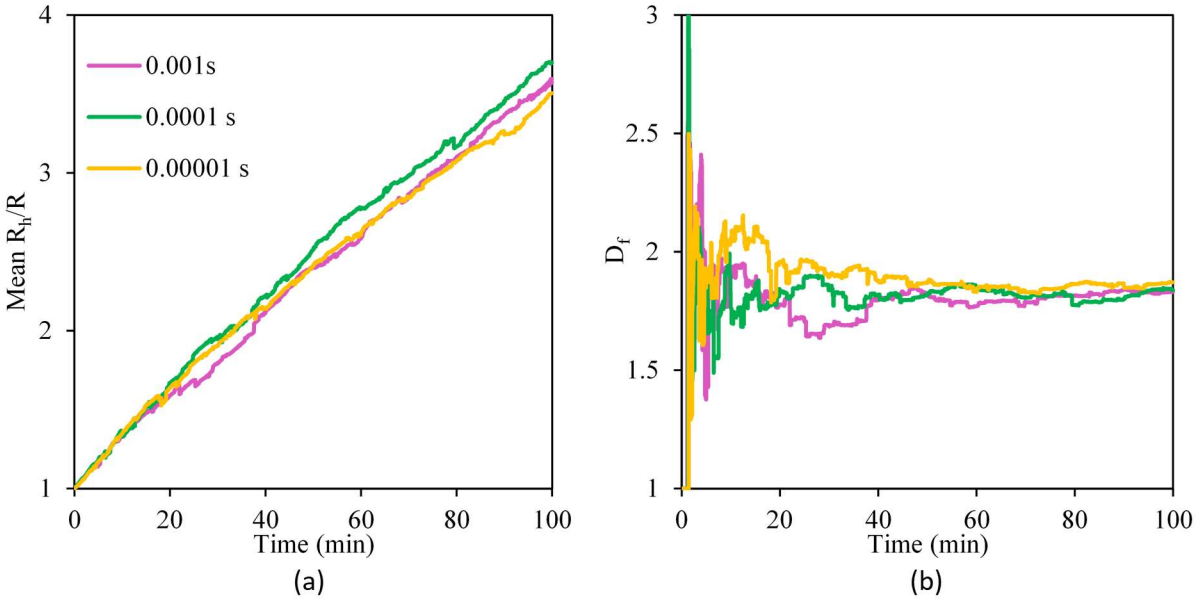


Figure B3. Aggregation kinetics (a) and fractal dimensions (b) of 10mg/L CeO_2 particles in the reaction-limited regime (0.02M KCl) with different cases such as particles frozen with user-defined freezing time 0.001s, 0.0001s, and 0.00001s.

B.4 Independence analysis of the grid resolution

Figure B4 illustrates the results for aggregation kinetics and fractal dimensions of nanoparticles aggregating in the sphere packing, with different grid resolutions, such as 201 x 201 x 201, 401 x 401 x 401, and 501 x 501 x 501. 10mg/L CeO_2 particles, suspended in 0.2M KCl aqueous solution, moved in the porous medium, sized 0.419 x 0.419 x 0.419 mm^3, at the average pore velocity of 500 μm/s. Convergence was achieved at the grid resolution 41 x 401 x 401 since there were no differences in the aggregation kinetics and fractal dimensions between the

resolutions 401 x 401 x 401 and 501 x 501 x 501. Therefore, in our study, the grid resolution 401 x 401 x 401 was applied for the simulation box of randomly packed spheres.

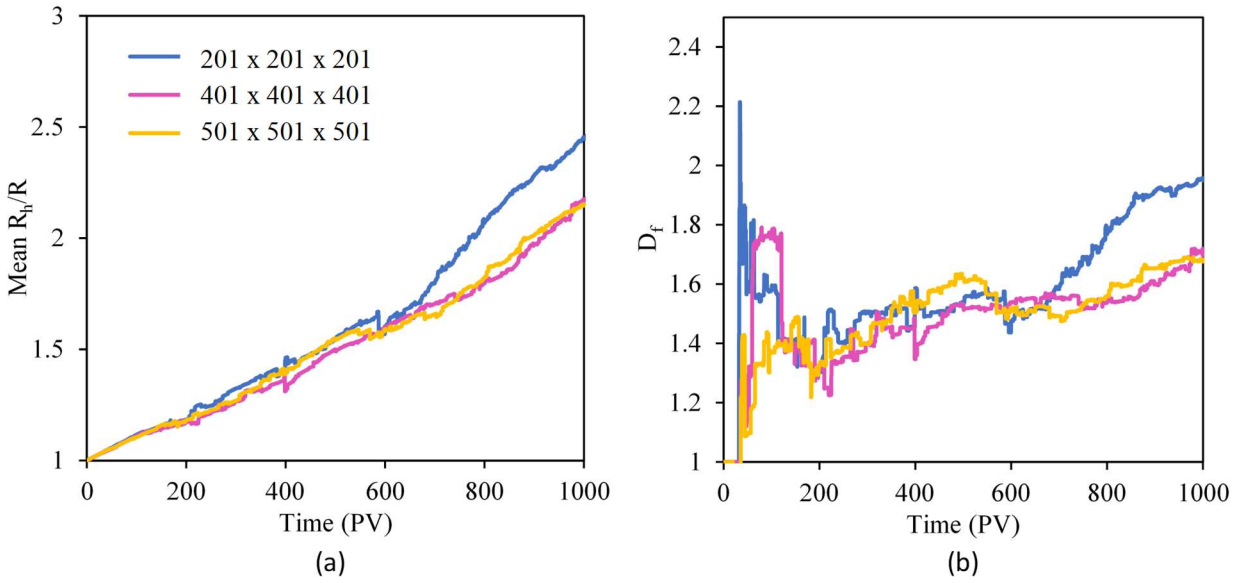


Figure B4. Aggregation kinetics (a) and fractal dimensions (b) of 10mg/L CeO_2 particles in the diffusion-limited regime (0.2M KCL) with different grid resolutions of porous media including 201x201x201, 401x401x401, 501x501x501. Particles travel through porous media at the average pore velocity of 500 μm/s.

B.5 Independence analysis of the cut-off radius

Based on Figure B4 representing the DLVO energy, the interaction forces among particles are applicable when the separation distance between particles is smaller than one diameter of a single particle, or the distance between the centers of two single particles is smaller than 2D. Simulations related to the aggregation of 10 mg/L CeO_2 particles suspended in 0.2M KCl at the bulk condition with different values of cut-off radius (such as 2D, 3D, and 4D) were performed. The aggregation kinetics and fractal dimension of aggregates were demonstrated in Figure B5; and they proved that the cut-off radius larger than 2D did not affect the results. Since the computational times for 2D and 3D cases were not much different, to be safe, R_c = 3D was selected in our numerical experiments.

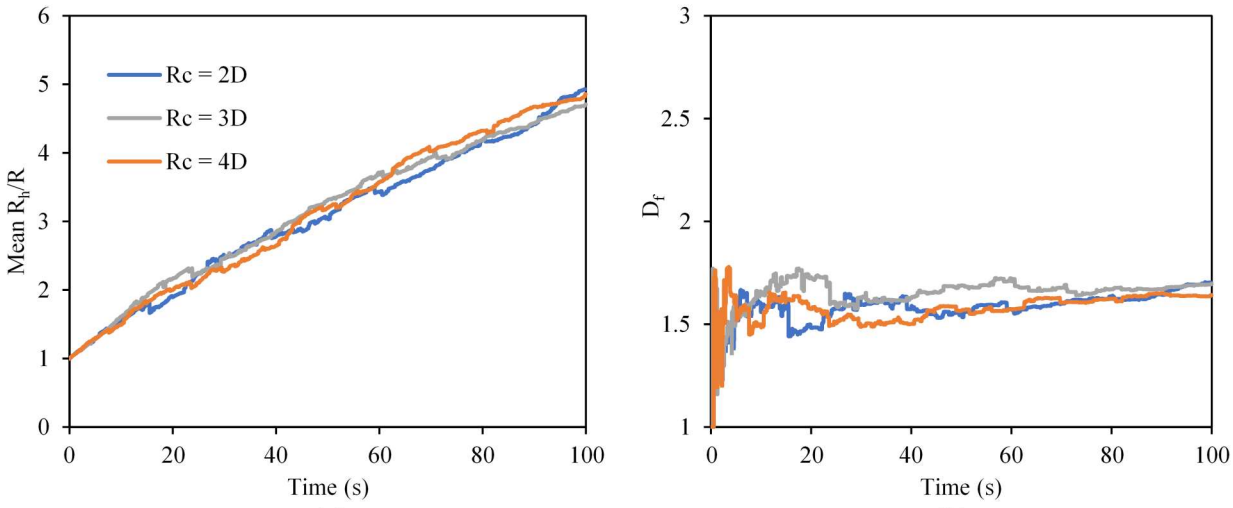


Figure B5. Aggregation kinetics (a) and fractal dimensions (b) of 10 mg/L nanoparticles CeO_2, in 0.2M KCl solution at bulk conditions, with different values of cut-off radius such as 2D, 3D, and 4D.